Master Thesis

Dynamic Simulation of a Wind Assisted Ship Propulsion System and its Time Domain and Frequency Domain Analysis

Ting-Kai Kuo

TU Delft

Master Thesis

Dynamic Simulation of a Wind Assisted Ship Propulsion System and its Time Domain and Frequency Domain Analysis

by

Ting-Kai Kuo

to obtain the degree of Master of Science
at the Delft University of Technology,
to be defended publicly on 28 September, 2020 at 12:30 PM.

Student number:	4786904	
Thesis number:	SDPO.20.022.m	
Project duration:	14 November, 2019 – 28 September, 2020	
Thesis committee:	Dr. Ir. A. Vrijdag,	TU Delft, supervisor
	Ir. K. Visser,	TU Delft
	Dr. Ir. H.J. de Koning Gans,	TU Delft

TU Delft

Summary

During the energy transition, a wind-assisted ship propulsion system has the potential for increasing energy efficiency according to the ship's EEDI (Energy Efficiency Design Index) in the short term. However, it would not only make the diesel engine run in off-design condition, but its dynamic behavior due to time-varying wind and waves is still unknown. Hence, for a selected case used in this thesis, a Flettner rotor is chosen to be further evaluated on the system's dynamic behavior under its favorable wind angle at Beaufort scale 6 and 7.

After modeling the wind-assisted ship propulsion system, it was linearized and normalized around its static operating points. This gives more insight into the system from a frequency-domain analysis via the Bode magnitude plots of engine speed, engine torque, and ship speed to the variation of true wind speed and wakefield induced by wave amplitude disturbance. In addition to the time-domain simulation for understanding the impact of the wind and wake disturbance on the system, the system response spectrum, which was proposed as an alternative approach for analyzing the system's dynamic behavior, was derived by connecting a wind and a derived wake spectrum to the Bode magnitude plots. Therefore, how the energy is conveyed from the marine environment to the system around its equilibrium can be tracked clearly.

Consequently, according to the selected case with a given controller, the results show that the fluctuation of true wind speed directly influences the ship speed, which in turn makes the engine torque be more sensitive to the variation of true wind speed in low-frequency regions. Besides, the engine speed resists to the variation of true wind speed very well due to the controller's introduction. Although the Flettner rotor generates approximately 44% of thrust at Beaufort scale 7, the true wind speed disturbance does not result in a significant engine loading disturbance compared with the fluctuation of wakefield, which significantly influences the engine speed and torque. It was found that it is related to the frequency region where the wake spectrum overlaps with the system sensitivity function. Within this region, the controller has a relatively poor performance, and thus an engine operating cloud can be noticed in time-domain simulation. However, the ship speed is not influenced significantly by the wakefield disturbance because the frequency region of wake spectrum does not overlap with that of the transfer function where the ship speed is more sensitive to the variation of wakefield. Finally, the sensitivity study implies that a further increase of ship total mass and moment of inertia enlarge the engine speed and torque in the frequency region where the controller does not perform well.

In conclusion, based on the selected case under its favorable wind condition, the potential of the wind-assisted ship propulsion system is still promising. Furthermore, the linearised model is a useful additional tool, and the system response spectrum gives more insight into the system.

Preface

I have learned a lot, applied what I have learned from TU Delft, and develop something new during the past months.

First of all, I would like to thank my daily supervisor, A. Vrijdag, for his full support, patient guides, positive encouragement, and valuable suggestions on my work. Especially when I was struggling, he always told me, " You are almost there!" which enables me to keep forward and to move from one stage to another. Moreover, I would like to thank R. Eggier, who also inspired me firstly during one of the IMarEST's lectures, and N J van der Kolk, who kindly provided me with assistance on hydromechanics.

In addition, I would also like to thank Cong-Biao Sui, who gave me suggestions on the diesel engine and Nikos Makrygiannis, who is willing to share his experience with me, and my classmate, Xiao-Sen Zheng during my two-year academic year.

Last but not least, I appreciate my parents and my family for their support of a two-year abroad study in the Netherlands.

Ting-Kai Kuo
Delft, September 2020

Contents

List of Figures

List of Tables

Nomenclature

Latin capitals

AWA	Apparent wind angle
AWS	Apparent wind speed
Bft	Beaufort scale number
C	Coefficient
D	Diameter
E	Error
F	Force
H	Transfer function
I	Moment of inertia
J	Advance ratio
K	Gain
M	Torque
MCR	Maximum continuous rating
P/D	Pitch diameter ratio
Q	Torque
R	Resistance
S	Spectrum
SA	Relative amount of fuel saving
SP	Span
T	Thrust
TWA	True wind angle
TWS	True wind speed
U	Tangential speed
V	Speed
WASP	Wind-assisted ship propulsion
X	Fuel rack position
Z	Height or Depth

Latin lowercase

a	Normalised propeller derivative
b	Normalised propeller derivative
c	Rotor derivative
e	Error
e	Normalised resistance steepness
f	Frequency
g	Normalised engine derivative
i	Gear box ratio
k	Velocity ratio
k	Wave number
m	Mass
n	Rotational speed
p	Normalised propeller derivative
q	Normalised propeller derivative
s	Rotor derivative
t	Time
t	Thrust deduction
u	X-axis speed
v	Y-axis speed
v	Normalised engine derivative
w	Wake

Greek symbols	
α	Resistance factor
β	Leeway angle
ζ	Sea surface elevation
η	Efficiency
θ	Pitch angle
κ	Contribution ratio
λ	WSP factor
μ	Heading relative to the waves
ρ	Density
τ	Integration constant
ω	Radial frequency

Matrices	
A	State matrix
B	Input matrix
C	Output matrix
D	Feedforward matrix
G	Gain matrix for disturbance

Vectors	
x	State vector
u	Input vector
y	Output vector
v	Sensor noise vector
w	Disturbance vector

Subscripts	
Q	Torque
T	Thrust
Z	Height
a	Advance
air	Air
b	Brake
d	Drag
e	Encounter
eng	Engine
f	Fuel
i	Integral
l	lift
nomi	Nominal
p	Proportional
prop	Propeller
s	Shaft
s	Ship
set	Setpoint
tan	Tangentail
v	Ship speed
water	Water
x	X-axial dierction
y	Y-axial dierction
θ	Pitch angle

Chapter 1

Introduction

1.1. General overview of literature research

Background

Wind power has been used to propel various ships for a long time in human history. Until the 20^{th} century, wind propulsion usage was gradually replaced by steam or diesel engines that use coal or oil containing high-density energy [Smith et al., 2013]. However, between 1970 and 1980, the price of fuel oil increased significantly. It was nearly ten-fold, which made the shipping industry whose bunkers cost account a high amount (almost 50%) of the Operational Expenses (OPEX) suffer from it [Bialystocki and Konovessis, 2016]. As a result, the oil crisis led to higher prices for these kinds of energy commodities and subsequently stimulated the possibility of using wind-assisted ship propulsion (WASP) as an alternative. A lot of effort has been made to understand better several wind propulsors, including the wing sail, the wind turbine, the Turbosail, the Flettner rotor, the Dynarig, and the kite since the arisen of the oil price. The potential for one of those devices, such as the wing sail, was demonstrated by two ships, Shin Aitoku and Usuki Pioneer, in the 1980's. However, due to the sudden oil price drop, the interest in the wind-assisted ship propulsion gradually faded out [Bordogna et al., 2014].

Recently, due to more awareness of the environment, especially approximately 3% of anthropogenic carbon dioxide, 13% of the global SOx and 15% of the worldwide NOx produced from the global shipping industry, several regulations aiming for the reduction of emissions, such as the Environmental Efficiency Design Index (EEDI) that requires new-build vessels with progressive carbon reduction and the introduction of the 2020 Sulfur Cap, were placed by the International Maritime Organisation (IMO). In addition to regulations, the operational cost still influenced significantly by the price of fuel oil cost. Therefore, reducing greenhouse gas emissions, harmful emissions (SOx, NOx), and fuel consumption become necessary [van der Kolk et al., 2019].

During this transition, wind-assisted propulsion is regarded as one of the few approaches for achieving those goals, especially cutting fuel consumption in the short term [Register, 2015]. Before that, some researches [Fujiwara et al., 2005] [Naaijen et al., 2006] were already carried out to quantify the benefits of wind-assisted propulsion. In 2014, according to the research [Traut et al., 2014] that was one of the complete studies simulating a voyage and considering wind power variability on the routes for a kite and a Flettner rotor, 20-45% amount of fuel reduction was found when vessels sailed at slow speed. However, the integration of the wind propulsors and the conventional propulsion machinery was not taken into account. In 2016, investigations considering the traditional mechanism of propulsion [Eggers, 2016], [Väinämö, 2016] indicated the potential of the Flettner rotor from simulations for a coaster and a real case (Ro-Ro vessel M/S Estraden) respectively. The first study concluded that fuel savings on the selected routes varied between 5-10%, whereas the second case implies that 2-12% saving in fuel consumption. Although much research on wind-assisted ship propulsion has been carried out over the years, the detailed performance of wind-assisted ships is still unclear. Hence, a performance prediction program is required to evaluate the wind-assisted ships better [Bordogna et al., 2014]. Most investigations have focused on aerodynamic and hydrodynamic behavior of WASP, because the aerodynamics of different wind propulsion components have to be integrated with the ship hydrodynamics to reach an equilibrium point first [Bordogna et al., 2014]. Especially for sailing yachts, a lot of research [Fossati, 2009] has been done. However, very few studies have been made from the perspective of a marine propulsion system. On the other hand, compared with other wind-assisted propulsion systems, more complete results for the Flettner rotor, including aerodynamics, hydrodynamics and marine propulsion system, can be found in the literature study. Hence, it is decided to only focus on the application of the Flettner in this master thesis.

After the case study [Eggers, 2016] pointed out that a more complicated engine model and ship motions should be studied further, another case study [van der Kolk et al., 2019] was conducted. The concern of ship motions was addressed by the system aiming at an equilibrium point with the minimum required propeller thrust in four degrees of freedom. Furthermore, a more detailed engine model accounting both engine's torque and shaft speed rate was adopted. In this case study for a medium-size ship, its performance with one and two Flettner rotors was analysed. From the perspective of the marine propulsion system, [Eggers, 2016], [van der Kolk et al., 2019] and [Väinämö, 2016] show that the spread of the engine operating point becomes large due to various amounts of wind thrust. Furthermore, under certain conditions, especially the wind speed reaches to a certain degree when the ship is required to sail at the design speed, it can be seen that the required engine power and speed become less, which makes the engine operate at it's off-design condition. In the same year, another similar research [Tillig and Ringsberg, 2019] that considered four degrees-of-freedom of a wind-assisted ship also implied that a large amount of thrust generated by rotors leads to a low engine power that might influence the engine operation.

However, those researches were simulation based on static conditions. In reality, the marine environment that a ship encounters in the real sea is time-varying, which indicates that the ship sails dynamically instead of statically. To investigate this effect on the marine propulsion system, some investigations were carried out for vessels without wind-assisted propulsors. Compared with resistance induced by the marine environment, waves can result in relatively more significant disturbance loading of a diesel engine, mainly when the engine shaft speed is controlled. The reason is that wake disturbance influenced by the wave affects the engine directly [Stapersma and Vrijdag, 2017]. A measurement [Van Spronsen and Tousain, 2001] shown in Figure 1.1 illustrates how the waves influence engine performance dynamically for a class frigate sailing in head waves in Sea State 6. It can be seen clearly that the engine operating region becomes a cloud instead of a point. Furthermore, to some extent, the engine is overloading.

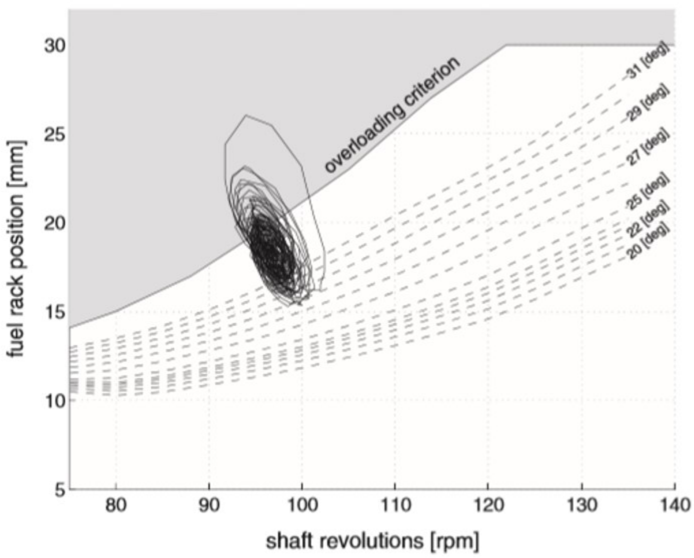

Figure 1.1: Measurement of engine speed and fuel rack of diesel direct propulsion for head waves in Sea State 6 [Van Spronsen and Tousain, 2001].

To further investigate how the wave disturbance influences the propulsion system, especially the diesel engine, the Mean Value First Principle (MVFP) was used for modeling the diesel engine so that the specific behavior, such as exhaust temperature, can be simulated [Geertsma et al., 2017b]. On the other hand, a linearised model considered an additional tool to predict system behavior in the frequency domain was also applied to evaluate the reaction of the propulsion plant in several wake frequencies and governor settings. By using a linearised model, the shape of the operating cloud can be analyzed systematically way [Vrijdag and Stapersma, 2017]. In conclusion, these researchers showed that the engine operating point becomes a cloud in a dynamic situation.

1.2. Research objectives and scopes

Despite the accumulation of literature regarding wind-assisted propulsion, there is an absence of research that examines the impact of the marine environment on the wind-assisted propulsion system as well as it's controller development in time-domain or frequency-domain simulation. Because the thrust generated by wind occupies a higher proportion of the total thrust force under some conditions, it results in a change of propeller operating points and thus engines operating points. In this situation, the fluctuating thrust generated by wind probably leads to a relatively more considerable disturbance to the diesel engine loading. According to the study [van der Kolk et al., 2019], the steady engine operating points can be seen under different wind conditions. In addition to wind, waves also impact the engine speed and torque, leading to engine operating clouds. Compared with the steady analysis, the engine operating cloud due to dynamic loading might touch the engine envelop. Some engine operating points might also be located in low-loading conditions, which makes the engine suffer from fouling issues. Considering these issues, it will be a benefit to investigate the engine operating point under dynamic conditions.

At this point, it has to mentioned that there is no research investigating the impact of time-varying wind on the diesel engine adopted in the wind-assisted propulsion system. Furthermore, it should be noted that wind-assisted propulsion's dynamic behavior is still unclear in state of the art. To investigate it, one question is :

To what extent, do wind and wave at different Beaufort scales influence the performance of the wind-assisted ship, especially for the propulsion diesel engine in the selected case?

To answer this question, several sub-questions are given as follows:

- How to relate wind and waves to a wind-assisted ship propulsion system?
- How to describe and quantify wind and waves at different Beaufort scales?
- With an engine speed controller, how does the behavior of a wind-assisted ship propulsion system, especially for its propulsion engine, is affected by wind and wave disturbance?

By evaluating those questions, the dynamical behavior of the wind-assisted ship propulsion system can be understood further. However, it should be pointed out that the scope of this thesis is limited to:

- At a approximately constant ship speed, the dynamic behavior at present are restricted to fluctuation in true wind speed and wave elevation at a certain true wind angle.

Furthermore, the following conditions and situations are going to be examined:

- Wind spectrum, wave spectrum, and the engine responses
- The effect of a certain wind direction providing the most potential benefit to the ship.
- A vessel using a medium-speed propulsion diesel engine as the prime mover, a fixed pitch propeller, and one Flettner rotor in one degree (Surge). If it is necessary, the 2-D model might be investigated.

1.3. Conclusions from literature research

In this section, a brief summary of the findings from the literature study was presented during the startup of this research project. Several conclusions are drawn for parametric modeling of wind-assisted ship propulsion systems, marine environment disturbances, operational conditions, and analysis approach after the literature research. Those will be referred as a methodology for addressing the research objectives.

1.3.1. Wind-assisted ship propulsion system modelling

The propulsion system examined in this thesis will be a typical mechanical propulsion system consisting of a medium-speed diesel engine, a gearbox, a fixed pitch propeller, and a Flettner rotor. Although the accuracy of the diesel engine model used in [Shi et al., 2010] is questionable at low loads, it is still chosen because it is acceptable for time-domain simulation. It was also used in the case study [van der Kolk et al., 2019], and it fits the purposes which are not for detailed engine behavior. Regarding the propulsion system control, although the literature [Geertsma et al., 2018] mentioned that controlling the engine speed results in engine load disturbance due to inconstant fuel injection, it will be a conventional diesel engine speed governor that controls the engine speed by adjusting the fuel rack position.

The nonlinear properties of the propulsion system will first be derived based on the work presented in [Stapersma, 2000]. However, the component, a Flettner rotor, was not included in this work. To address this issue, the Flettner rotor model can be derived based on the researches [Bordogna et al., 2019] [Eggers and Kisjes, 2019] and subsequently added in it.

1.3.2. Environment disturbance modelling

As far as the modeling of marine disturbances is concerned, it has to be mentioned that only the impact of the true wind speed disturbance and wake disturbance induced by wave amplitude on the propulsion system will be examined in this thesis. The reasons for that are stated below:

- The additional thrust generated by a Flettner occupies a relatively more significant portion of the total thrust [Eggers, 2016]. Hence, the variation of this extra thrust due to time-varying wind might have a significant impact on the dynamic behavior of the propulsion system, such as the diesel engine's performance.
- The more direct effect of the wakefield variations on the behavior of the rotating shaft system and the engine operating point, compared to the ship resistance variations [Stapersma and Vrijdag, 2017]. Thus, the wakefield disturbance induced by wave amplitude disturbance is chosen to be focus.
- The level of difficulty of the approaches used to obtain the resistance in waves, compared to those for calculating the wakefield variations.

Since the real marine environment data can not be obtained from measurement, the time-varying true wind speed and wave amplitude can be generated similarly as the research [Pérez and Blanke, 2002]. Furthermore, these two time-varying signals at each Beaufort scale can be derived from the Frøya wind spectrum and the Pierson-Moskowits spectrum that also adopted in study [van der Kolk et al., 2019]. On the other hand, wakefield variations can be obtained according to the classic linear wave theory adopted in the study [Geertsma et al., 2017a]. Additionally, in this thesis, some assumptions and simplifications will be applied to calculate the wakefield disturbance and are cited below:

- Only the axial component of velocity is modeled. In other words, the influence of other contributing factors, such as radiated waves, diffracted waves, are not considered.
- The wave disturbance velocity over the whole propeller disk equals the wave velocity at the center of the propeller hub. This means that the velocity distribution in the radial direction over the propeller is not considered.
- The ship speed and it's heading angle are considered constant despite the unsteady wake.

1.3.3. Time-domain and frequency-domain analysis

Before analyzing the dynamic performance of the wind-assisted propulsion system for the selected case, the performance of the derived model in static conditions at its favorable wind direction will be verified by comparing its results with results from the case study [van der Kolk et al., 2019].

Despite the accumulation of literature regarding the use of the Flettner rotor as wind-assisted propulsion, there is an absence of research that dynamically examines its impact on the propulsion system. Therefore, to further push the analysis step, the same case used in study [van der Kolk et al., 2019] with only one Flettner rotor will be analyzed in time-domain and mainly in the frequency domain.

The analysis of the wind-assisted propulsion system will be in its favor wind condition that the true wind angle is 120 [degree]. The reasons for that are stated and justified below:

- Based on the study [Blok, 1993], the added resistance due to waves for the following seas is relatively low, and it is decided to ignore its impact.
- The most fuel is saved at 120 [degree] according to the research [van der Kolk et al., 2019].
- The spin ratio varies moderately under this condition [van der Kolk et al., 2019].

To better investigate this condition quantitatively and systematically, the nonlinear submodels will be linearized and be an extension to previous works [Vrijdag and Stapersma, 2017]. In conclusion, the linearised model offers an advantage that parameters and variables link clearly and transparently so that it can be applied to address the main research question. Subsequently, the response of the wind-assisted ship propulsion system can be investigated by connecting regular disturbances of true wind speed and wake firstly. This will provide a foundation for understanding the dynamic behavior of the wind-assisted ship propulsion system in irregular environmental factors.

1.4. Approach

To answer the research questions, the steps adopted in this thesis are present as follows:

- **Derive a nonlinear model that describes a wind-assisted ship propulsion system of the reference vessel.**

  The nonlinear-model, derived from a physical background of the wind-assisted ship propulsion system, can be used to simulate its dynamic behavior in the time domain. In the case, the reference vessel is CF5000 given by Damen Shipyards Group, whereas the wind propulsor is a Flettner rotor provided by NORSEPOWER. By combining a conventional propulsion system with the Flettner rotor, the static engine operating point of the wind-assisted ship propulsion system at different Beaufort scales under its favorable true wind angle can be obtained firstly. Furthermore, a certain degree of disturbances, including the true wind speed and wakefield, can also be incorporated into the system. By comparing its static performance with existing results from the study [van der Kolk et al., 2019] and evaluating its primary dynamic performance, a certain degree of confidence can be guaranteed for the derived nonlinear model of the wind-assisted ship propulsion system.

- **Derive a linearised model based on the nonlinear model.**

  To better answer the main research question: to what extent do marine disturbances influence the system, the frequency-domain analysis, which gives more insight into how the system is sensitive to the input disturbances within a specific frequency region, is conducted. Hence, a linearised model, which is regarded as an additional tool for investigating the dynamic behavior of systems in the frequency domain, is derived by normalizing and linearizing around its equilibrium, which can be obtained from the nonlinear model. In addition to the linearization that provides how the disturbances are conveyed through the system, the normalization allows the system to be independent of physical dimensions. In this thesis, the Bode magnitude plots is adopted to investigate the system response to the regular disturbances at each frequency. Thus, the frequency-domain behavior of the system can be illustrated more clearly.

- **Derive the wind, wave, and wake spectrum that can be used to describe disturbances from the marine environment.**

  To relate the behavior of the wind-assisted ship propulsion system to the disturbances it encounters at different Beaufort scales, it is necessary to describe and quantify the disturbances' properties, which are true wind speed and wake induced by wave amplitude in this thesis. Their properties can be obtained respectively via the wind and wave encounter spectrum. Specifically, the irregular disturbances used in the time-domain analysis can be generated by each spectrum, whereas the spectrum showing how the energy is distributed for wind and waves can be used for frequency-domain analysis. Furthermore, because the inputs representing disturbances for the nonlinear and linearised model are true wind speed and wakefield, how the wakefield disturbance relates to waves amplitude will be derived. Consequently, the wake spectrum is derived in Chapter 4.

- **Time-domain and frequency-domain analysis of the system.**

  After the nonlinear and linearised models are obtained, the time-domain and frequency-domain analysis can be carried out. This is first done by relating estimated disturbances based on the environmental spectrum to the nonlinear model from the time-domain perspective. However, to get more insights, the system's response spectrum, which can be obtained by relating the Bode magnitude plots to the wind and wake spectrum, can be used to see the system's frequency-domain response to the disturbances. Finally, the sensitivity study shows how the total ship mass and moment of inertia influence the system's responses to disturbance in frequency domain. These all will be presented in Chapter 5.

1.5. Thesis outline and contribution

This thesis can be regarded as an extension of the study [van der Kolk et al., 2019] because the dynamic behavior of the wind-assisted propulsion system, mainly for the diesel engine, will be further investigated. Another extension is the linearised of the Flettner rotor becasue it will be implemented in the linearised propulsion system used in the research [Vrijdag and Stapersma, 2017]. In the following chapters, the research process for answering the research questions will be presented step by step. Chapter 2 first introduces the Flettner rotor to a conventional propulsion system, and its results at the favor wind condition will be compared with results from the research [van der Kolk et al., 2019]. Chapter 3 shows the procedure and process of deriving and verified the linearized model, and its results will be compared with that of the nonlinear model derived in Chapter 2. Hence, a higher level of confidence can be guaranteed for the derived linearised wind-assisted ship propulsion system model. In Chapter 4, the modeling of disturbances from the marine environment for true wind speed and wake will be presented. The relation between the wave amplitude and wakefield will also be derived to obtain the wake spectrum. After that, Chapter 5 relates the true wind disturbance and wake disturbance to the wind-assisted ship propulsion system. To give a deeper insight, the analysis will be mainly carried out in frequency-domain analysis based on the derived linearised model and the system response spectrum. Furthermore, some parameters can be set to a different value in order to investigate the impact of them on the system's response to marine disturbances.

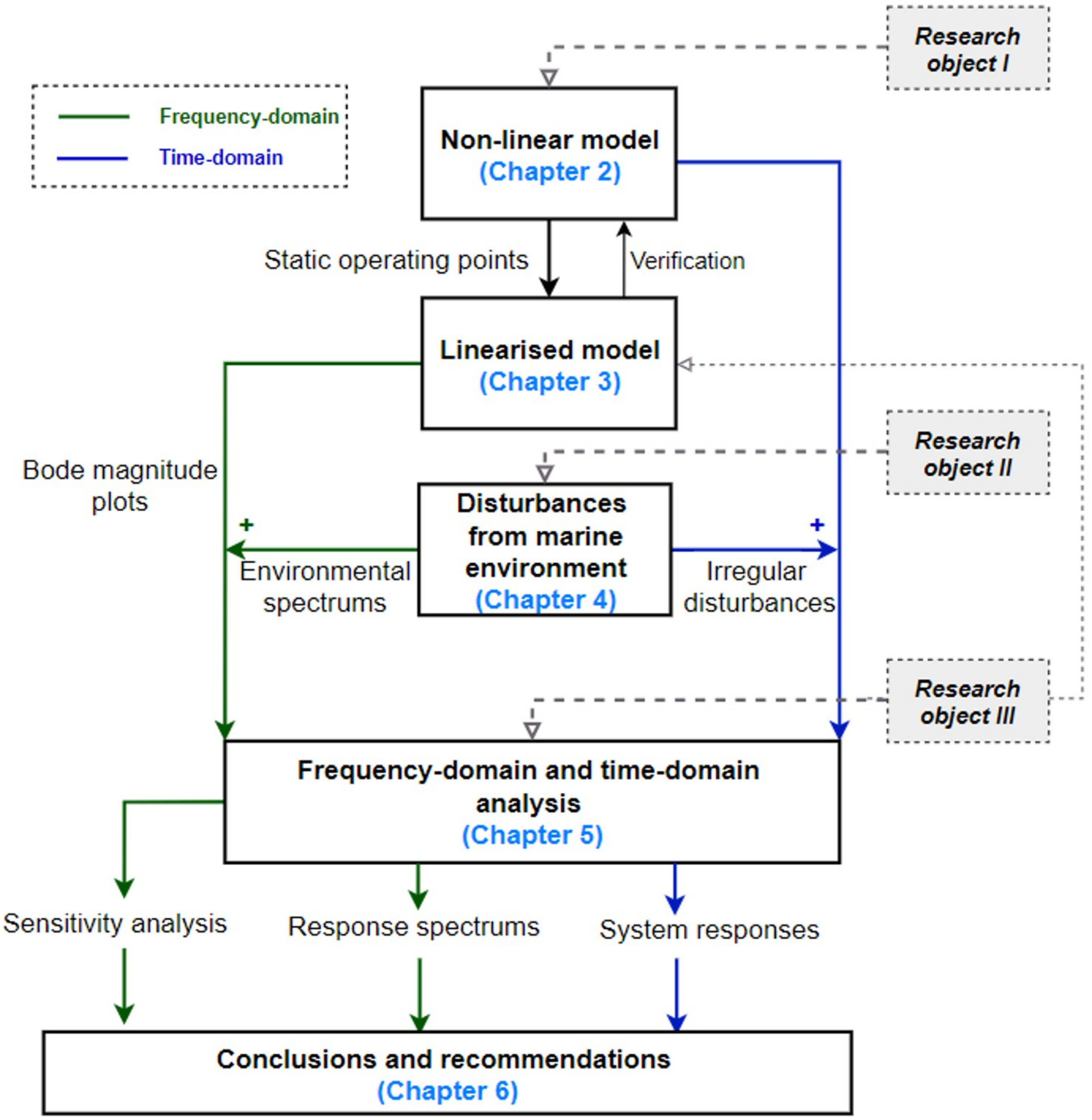

Figure 1.2: Thesis outline.

Chapter 2

Nonlinear wind-assisted ship propulsion system model

In this chapter, the process of deriving the nonlinear model of the wind-assisted ship propulsion system model is introduced and shown step by step. Furthermore, it's static and dynamic behavior are verified by comparing with the same case used in the study [van der Kolk et al., 2019] and expectation.

2.1. General ideas on the simulation model approach

To investigate the dynamic behavior of marine propulsion system with wind-assisted devices, such as the Flettner rotor, one of practical approaches is the application of simulation models including computational model based on conceptual model shown in Figure 2.1. The inside arrows mean the process required to derive from one part to another one, whereas the outside ones represent the relation with each element. To guarantee the credibility of the simulation model and its capability of representing the reality: real wind-assisted ship propulsion system, it has to be first analyzed and subsequently conceptual model can be built based on, for example, mathematical models including equations and assumptions that govern or represent the real system. With the conceptual model, a computerized model derived from it can be used to find the conceptual model's simulation results that is believed to be the performance of system in reality.

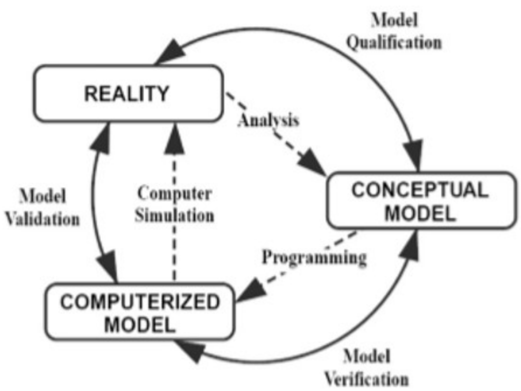

Figure 2.1: Phase of deriving a simulation model from reality [Schlesinger, 1979].

With the simulation model, designers would have more opportunities to predict the wind-assisted ship propulsion system performance under different operational conditions at the early stage. Moreover, some scenarios which is difficult to test in reality can also be investigated and the usage of scale models which are costly in time and effort might also be unnecessary. Therefore, in this thesis, a parametric simulation model for wind-assisted ship propulsion system is proposed, because it not only provides a clear relationships between inputs and outputs of parameters and variables but also provides benefits for understanding more about the performance of real system. This would also pave a way for application in controller development and even optimizations of the system. However, before building the conceptual and computerized model for wind-assisted ship propulsion system, it is necessary to determine those models purposes aiming for answering the research questions since the models' complexity depend highly on them. Take a diesel engine model as an example, instead of investigating very detailed and specific engine performance, such as inlet and exhaust temperature, the main purpose of this element is generating torque with a given amount of injected fuel at each engine speed. In conclusion, considering several disciplines, such as aerodynamic and hydrodynamic, are across in this thesis and to address the research questions efficiently, it would be benefit to keep the model as simple as possible despite the fact that its accuracy in some condition decreases due to assumptions and conditions simplifying the model.

2.2. Reference vessel

Following the same case adopted in the study [van der Kolk et al., 2019], the reference vessel is shown in Figure 2.2. It is the Combi Freighter 5000 (CF5000) given by DAMEN shipyards, and only a propeller, a rudder and a diesel engine are used for this seagoing cargo vessel. It's basic characteristics are: LOA (Length overall)=86.82 [m], Beam=15.2 [m], Draft=6.35 [m], Displacement =6682 [t] and Deadweight=5150 [t]. Concerning the Flettner, only one Flettner rotor is installed on the forward part of the hull. Note that if more than one Flettner rotor were installed, the interaction between these rotors is also required to be taken into consideration, which makes the model more complex. Therefore, using a Flettner rotor is a better first step to investigate the dynamic behavior of the wind-assisted ship propulsion system. Regarding the Flettner, its diameter is 3 [m], and the span (the length from the bottom to the the top of the rotor) is 18 [m].

Before analyzing wind-assisted ship, a realistic baseline propulsion system without the rotor was firstly made. The result is that a maximum ship speed of 11 [knot] can be achieved at maximum engine speed and approximately 85% MCR (Maximum continuous rating). With the highest open water efficiency for the propeller, the pitch diameter ratio, P/D, is set to be 0.85 and the ship service speed, 10 [knot], can be achieved. This baseline design is also the same as the case used in the study [van der Kolk et al., 2019].

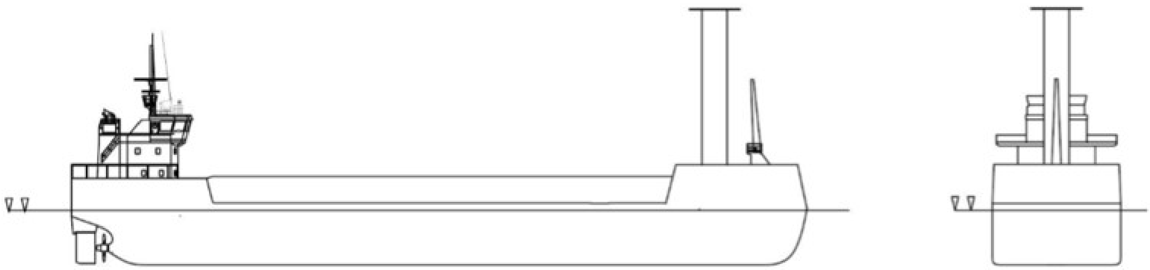

Figure 2.2: CF5000 with one Flettner rotor.

2.3. Simulation sub models

The first step of building the wind-assisted ship model is connecting the effect of wind to the ship via several sub models.

Wind shear

The WASP system performance depends highly on the magnitude of wind speed and [Fossati, 2009] state it varies with height above the sea surface due to the earth boundary layer. As a result, the magnitude of shear wind, the vertical distribution of the mean horizontal true wind speed, is required to be introduced first. Conventionally, the Beaufort scale (Bft) is an indicator used to describe the wind speed observed at sea or on land. This indicator might also be used for adjusting the WASP system setting. Thus, the mean horizontal wind speed scaling based on the Beaufort scale at 10 meters above the sea surface can be approximated as [Heier, 2014]:

$$TWS_{10} = 0.836 \cdot Bft^{1.5} \quad [m/s] \tag{2.1}$$

Considering variations in horizontal wind speed due to the height, the position of the wind speed sensor would provide a useful indicator for the magnitude of wind speed. According to NORSEPOWER [Kuuskoski, 2017], the wind speed sensor, in this case, would possibly be equipped at the top of the pole in front of the Flettner rotor shown in Figure 2.2. At this height, which is approximately half of the Flettner rotor span, the horizontal true wind speed used for the rotor can be described as:

$$TWS_0 = TWS_{Z=10} \cdot (\frac{Z_{wind,\ sensor}}{Z_{10}})^{0.1} \quad [m/s] \tag{2.2}$$

Note that the scale coefficient, 0.1, is used here [Kaltschmitt et al., 2007] because the Frøya spectrum is originally developed for neutral conditions over water in the Norwegian Sea, which indicates that there is no exchange of heat energy in the vertical direction and the wind profile is not influenced by it.

Apparent wind model

Another effect influencing the wind characteristic sensing by the ship is its motion. In fact, the wind experienced by the ship, or measured by the wind sensor in this case, is not the true wind, instead, it is relative wind or so-called apparent wind. Thus, the apparent wind speed and angle measured by the wind sensor are influenced so that a simple apparent wind model is necessary to be built and illustrated in Figure 2.3. By assuming that the ship's rudder perfectly adjusts the ship's heading angle, it is relatively small and can be ignored. Under this condition, the apparent wind speed (AWS) and the apparent wind angle (AWA) can be related to true wind speed (TWS), true wind angle (TWA), ship speed (V_s) and leeway angle (β) and is illustrated in Figure 2.3. According to the study [Eggers and Kisjes, 2019], for the true wind angle is between 0 to 180 [degree], the apparent wind speed and angle at the same height as the observed true wind can be obtained by applying the formulas:

$$AWS = \sqrt{u^2 + v^2} \quad [m/s] \tag{2.3}$$

$$AWA = \begin{cases} \tan^{-1}(\frac{v}{u}) & [rad], \quad (u \geq 0, v \geq 0) \\ \frac{\pi}{2} & [rad], \quad (u = 0, v > 0) \\ \pi + tan^{-1}(\frac{v}{u}) & [rad], \quad (u < 0, v > 0) \end{cases} \tag{2.4}$$

where the true wind speed in x-axis and y-axis, u and v, can be written as

$$u = V_s \cdot cos(\beta) + TWS \cdot cos(TWA - \beta) \rightarrow u = V_s + TWS \cdot cos(TWA) \tag{2.5}$$

$$v = V_s \cdot sin(\beta) + TWS \cdot sin(TWA - \beta) \rightarrow v = TWS \cdot \sin(TWA) \tag{2.6}$$

The leeway angle (β) is introduced due to wind-assisted devices and its range is expected between 0 to 10 [degree] [Drenthe et al., 2016], which is not too large and it is decided to ignore the effect of the leeway angle in this case. In addition, because the wind properties are the same from port or starboard side of the ship, only the true wind angle range between 0 to 180 degrees is derived.

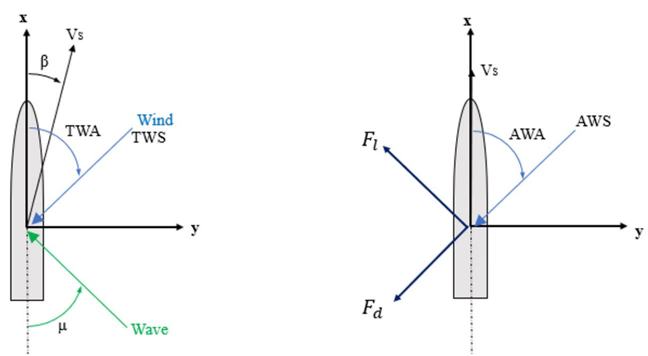

Figure 2.3: Definition of true wind angle (TWA), apparent wind angle (AWA), leeway angle (β) and forces induced by the Flettner rotor. Note that μ is the ship heading relative to waves, which means that μ=180 [degree] represents head waves.

Flettner rotor model

After the wind properties sensed by the Flettner rotor are obtained correctly, the way to derive a sub-model describing the performance of the Flettner is shown in this section. Note that the thrust generated by apparent wind is the combination of the lift force F_l and drag force F_d from the horizontal instead of the vertical plane. Thus, before modeling this thrust generated by wind, the properties of lift and drag forces are required to be modeled firstly. Regarding the direction of lift and drag force, they are perpendicular and parallel to the apparent wind flow and shown in Figure 2.3.

Concerning the magnitude of lift and drag force, they are various at a different rotational speed of the Flettner rotor. To better describe them, two non-dimensional lift and drag coefficients can function as a spin ratio (k), which is defined as a ratio of the tangential velocity of the rotor (U) to the incoming wind speed (AWS). In this thesis, both the lift and drag coefficients were obtained from the study [Bordogna et al., 2019] that also used in the case study [van der Kolk et al., 2019]. With these two coefficients shown in Figure 2.4, the lift and drag force can be modeled as:

$$\begin{cases} F_l = C_l \cdot \frac{1}{2} \cdot \rho \cdot AWS^2 \cdot SP \\ F_d = C_d \cdot \frac{1}{2} \cdot \rho \cdot AWS^2 \cdot SP \end{cases} \tag{2.7}$$

where C_l and C_d are lift and drag coefficient that can be obtained from Figure 2.4 whose values depend on the spin ratio. ρ is the air density and SP is the Flettner rotor area that equals to the production of it's diameter and it's height.

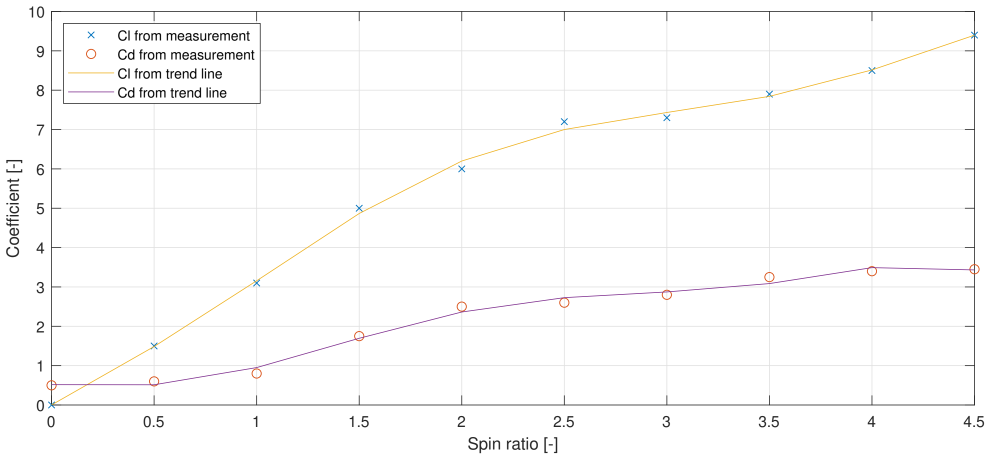

Figure 2.4: Lift and drag coefficient vs spin ratio.

Regarding the spin ratio, k, which is related to the its diameter, D_{rotor} and its shaft speed, n_{rotor}, the spin ratio can be obtained as:

$$k = \frac{U_{tan}}{AWS} = \frac{\pi \cdot D_{rotor} \cdot n_{rotor}}{AWS} \tag{2.8}$$

Finally, to obtain the thrust ($F_{rotor,x}$) as well as heeling force ($F_{rotor,y}$) generated by wind, lift and drag force can be transferred as:

$$\begin{cases} F_{rotor,x} = F_l \cdot sin(AWA) - F_d \cdot cos(AWA) \\ F_{rotor,y} = F_l \cdot cos(AWA) + F_d \cdot sin(AWA) \end{cases} \tag{2.9}$$

2.4. Simulation main model

Following the research [Vrijdag and Schuttevaer, 2019] regarding modeling the marine propulsion system used in surge direction and the literature [van der Kolk et al., 2019] using the polar chart to illustrate the performance of wind-assisted propulsion system under different wind conditions, an extensional sub-models that mentioned in the previous sections about modeling the Flettner rotor was included.

Furthermore, based on the polar chart, the setting of the engine speed and the rotor speed in different wind conditions can be obtained and subsequently used for the simulation of a wind-assisted ship propulsion system.

The conceptual model of wind-assisted ship propulsion system used for ship's surge motion is illustrated in Figure 2.5 in block diagram form. Because forces in surge direction, which are related to the engine's performance, are mainly focused, the derived heeling force, $F_{rotor,y}$, shown in Eq. (2.9) is not presented in the figure. Although the heeling force does not directly influence the forces in surge direction [Schot and Eggers, 2019], it can be used for verification of the wind-assisted ship propulsion system shown in Section 2.6.1.

In general, the conceptual model mainly consists of seven parts including the apparent wind model, a Flettner rotor, a ship hull, a propeller, a propulsion machine, an engine speed governor and a polar chart providing a basic guideline for adjusting the control variables, such as pitch angle, the rotor's rotational speed, and engine speed. According to the block diagram, the relationships between variables are transparent and the object for each part is clear while keeping the model as simple as possible. The detailed properties of each part is introduced one by one in this section.

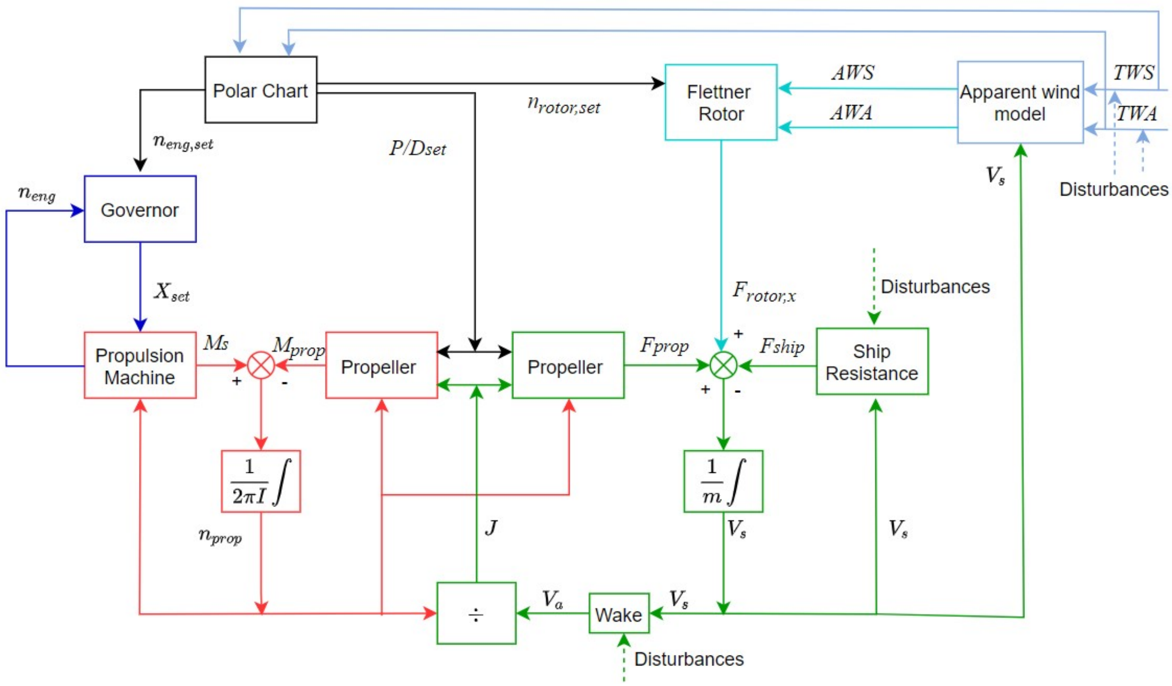

Figure 2.5: Block diagram of wind-assisted ship propulsion system model.

2.4.1. Polar chart

Wind energy can be used for generating forward thrust in two ways. The first option is that the ship speed increases when the engine loading remains the same, whereas the second one is that the ship speed remains the same, and the engine loading decreases.

Following the same case used in the literature [van der Kolk et al., 2019], the second option is chosen to be investigated, and thus maintaining the ship speed, 10 knots, is adopted for the WASP system modeling in this thesis. To achieve this goal in this case, a question must be answered: how to set the engine speed, pitch angle, and the Flettner rotor's rotational speed for a given true wind speed and angle? In this case, only a fixed pitch propeller was used so that only two control variables, the engine speed (n_{eng}) and the rotor's rotational speed (n_{rotor}) are needed to be taken into account. Conventionally, instead of controlling the primary object, ship speed, a control variable, such as engine speed that has an almost linear relation with ship speed is chosen. Controlling the ship speed via the engine speed is, in fact, a feedforward approach that is probably argued by a feedback through people in the loop [Vrijdag et al., 2010]. However, due to different contributions of force generated by wind with different speed and angles, this conventional control strategy needs to be adjusted based on wind conditions if the ship speed is required to be approximately maintained constant. Hence, a polar diagram regarding the setting of the engine speed and the rotor's rotational speed for a given wind speed and angle is proposed and shown in Figure 2.5 for the simulation in this thesis.

In the study[van der Kolk et al., 2019], to sail at 10 knots, the minimum propeller thrust in different wind conditions is found while four degrees of freedom(surge, sway, roll, and yaw) are taken into consideration. Based on those data, two polar diagrams aiming to achieve the ship speed for a given condition are provided. By referencing those two polar diagrams, the people in the "loop" could know how to set the engine speed and the rotor's rotational speed based on different wind conditions. Furthermore, because spinning the Flettner rotor requires additional power, the study [van der Kolk et al., 2019] [Eggers, 2016] indicate that a plateau for both the lift and drag force was found at k=4, which means the gain in extra propulsion is very small compared to the extra power required to spin the rotor. Therefore, Figure 2.6 shows that the spin ratio is limited until 4 despite the increasing wind speed. Note that another polar diagram regarding the required engine power is also derived in the study [van der Kolk et al., 2019]. An instance of how to use the polar diagrams presented in Figure 2.6 is given here: If the true wind speed is 30 knots and the true wind angle is 120 degrees, the engine speed and the spin ratio are set approximately 760 [rpm] and 4. Under this condition, the required engine power is around 400 k[W].

In this thesis, the same case and parameters are used as the literature [van der Kolk et al., 2019]. Therefore, these three polar charts provide an initial guideline for the setting of the engine speed as well as the rotor's rotational speed that can be derived from the spin ratio. Finally, the required engine power for a given wind condition can also be seen.

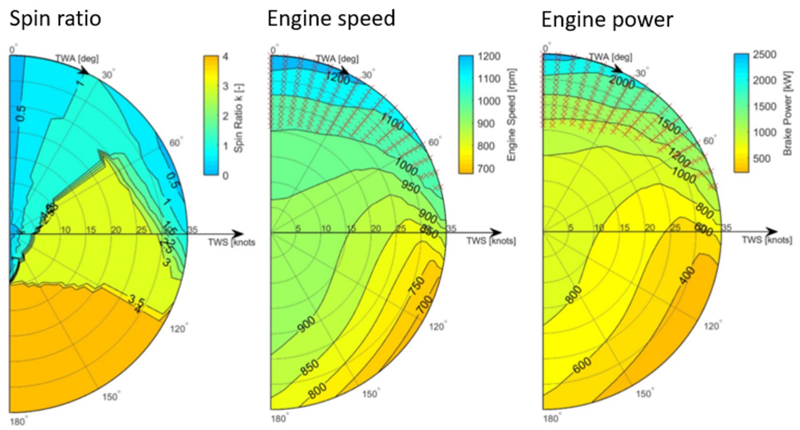

Figure 2.6: Polar charts about required spin ratio for the Flettner rotor, required engine speed and power when sailing at 10 knots [van der Kolk et al., 2019]. Note that the unit used here for wind condition is knot.

2.4.2. Propeller model

The propeller acts as a link between the outboard environment and inboard machines. The main function of the propeller is to generate the thrust to propel the ship forward. The propeller thrust can be generated when the propeller torque is produced from an engine via a power transmission system. Based on the Wageningen B-Series that is commonly applied for a fixed pitch propeller, a simple polynomials model given by Oosterveld and van Oossanen [Carlton, 2018] can be used to obtain non-dimensional thrust coefficient, K_T, and torque coefficient, K_Q, at each advance ratio, J. Given the propeller's pitch diameter ratio (P/D), blade area ratio (AE/AO) and the number of blades (Z), the K_T and K_Q are approximated as:

$$K_Q = \sum_{n=1}^{47} C_n (J)^{S_n} \cdot (P/D)^{t_n} \cdot (A_E/A_O)^{u_n} \cdot Z^{v_n} \tag{2.10}$$

$$K_T = \sum_{n=1}^{39} C_n (J)^{S_n} \cdot (P/D)^{t_n} \cdot (A_E/A_O)^{u_n} \cdot Z^{v_n} \tag{2.11}$$

where the coefficients, C_n, S_n, t_n, u_n and v_n, are provided in tables presented in [Carlton, 2018], and the advance ratio, J, can be found as a way shown in Figure 2.7.

Considering the influence from the leeway angle, which lies from 0 to 10 degrees for WASP system [Drenthe et al., 2016], it is assumed that the leeway angle does not influence the propeller behavior significantly via the disturbed wakefield. This assumption was also adopted in the study [van der Kolk et al., 2019] so that the propeller model would not be too complex and it can be ignored. Finally, with those non-dimensional coefficients and considering some energy loss induced by propeller-wake interaction, a relative rotative efficiency, η_r, is introduced. Hence, the actual propeller thrust,F_{prop}, and torque,M_{prop}, can be produced as:

$$M_{prop} = \frac{K_Q \cdot \rho \cdot n^2 \cdot D^5}{\eta_r} \tag{2.12}$$

$$F_{prop} = K_T \cdot \rho \cdot n^2 \cdot D^4 \tag{2.13}$$

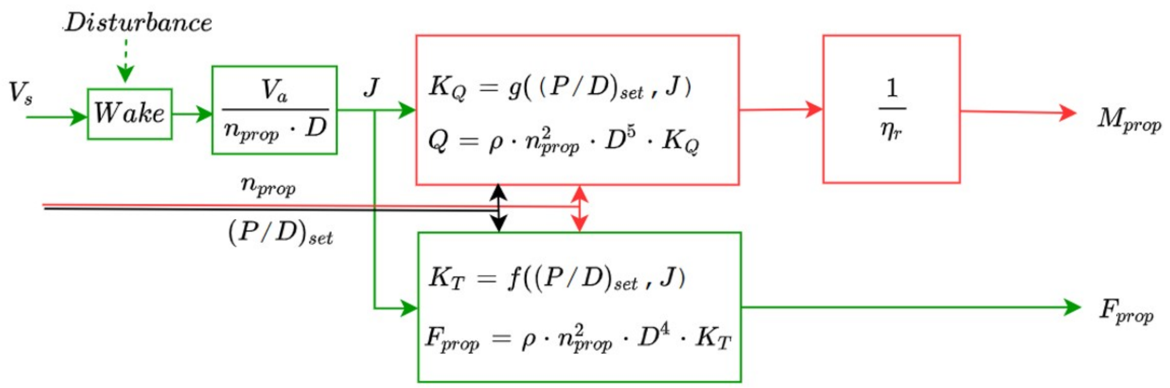

Figure 2.7: Block diagram of the propeller.

2.4.3. Ship's hull model and ship speed loop

In this section, a ship speed loop, which considers the interaction of ship force, propeller force, and the force provided by the Flettner rotor in the longitudinal direction of motion, is derived. Before adding the ship force in the ship speed loop, different types of ship resistance should be pointed out first. A conventional ship total resistance consists of viscous, form, and wave resistance. Following the same case in the literature [van der Kolk et al., 2019], the total resistance of CF5000 without a Flettner rotor at each ship speed was estimated by towing a scale model in calm water and shown in Figure 2.8 where blue dots and the red line are the resistance curves from the measurement and from the trend line given in Eq. (2.14). Despite some deviation of the ship total resistance, the resistance described by the trend line is still acceptable around the ship speed 10 [knot], which is approximate 5.144 [m/s].

Moreover, with the introduction of a Flettner rotor and waves in a seaway, the added resistance due to leeway angle and waves are needed to be considered. First, based on the research [Blok, 1993], the increase of added resistance due to waves is relatively low in following seas compared with that in head seas. Second, according to Figure 2.11, the side force generated by the Flettner rotor at true wind angle 120 degrees is relatively low, which indicates that a small leeway angle is required for the ship to keep balance. Hence, the increase of added resistance due to leeway would be relatively low. As a result, when the true wind angle is 120 degrees, the added resistances induced by waves and leeway angles are relatively low so that they are assumed to be neglected. Therefore, the ship total resistance of CF5000 without the Flettner rotor can be used, and it is represented as a lookup table based on the red line in Figure 2.8.

$$R = \alpha \cdot V_s^e \tag{2.14}$$

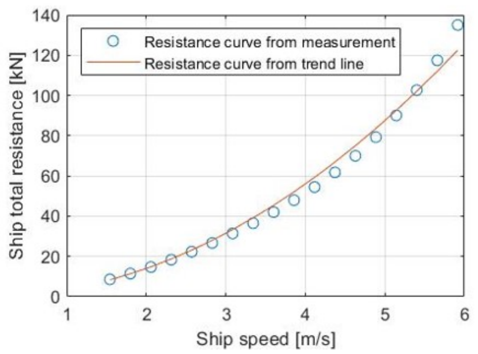

Figure 2.8: LHS: Resistance of CF5000 based on scale model(blue dot) and interpolated curve (redline). RHS: Difference between two resistance curves.

Considering the effects of the propeller-hull interaction, the thrust deduction factor, t, is implemented and the actual ship force can be calculated by:

$$F_{ship} = \frac{R_{ship}}{(1-t)} \tag{2.15}$$

For the ship speed loop, after the Flettner force (shown in Section 2.3), the propeller force (shown in Section in 2.4.2), and the ship force are obtained, the dynamic behavior of the ship in longitudinal direction can be derived based on Newton's second law. The net force results in the longitudinal acceleration of the ship, and the ship velocity can be derived by integrating this acceleration. Hence, the ship speed loop, describing the dynamic ship behavior in the longitudinal direction, can be calculated as:

$$V_s = \frac{1}{m_{ship}} \cdot \int (F_{rotor,x} + F_{prop} - F_{ship})dt + V_{s,0} \tag{2.16}$$

where the total ship mass, m_{ship} includes the added mass induced by the surge motion of the ship, such as acceleration or deceleration. According to the literature [Journee and Pinkster, 1997], this added mass in longitudinal direction direction is approximately 5-8 % of the actual ship mass and it is assumed to be 7.5% in this case. $V_{s,0}$ is the initial ship speed [m/s].

2.4.4. Propulsion machine, governor model and shaft speed loop

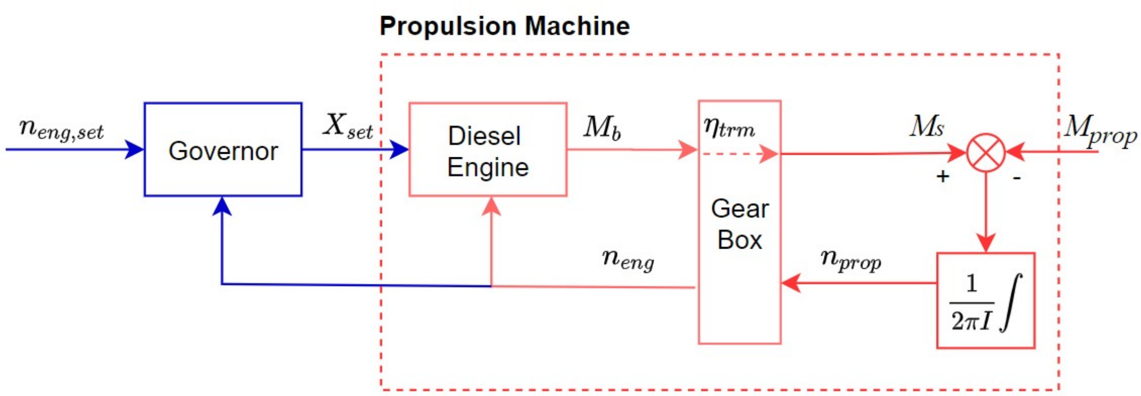

Figure 2.9: Block diagram of a engine speed governor and a propulsion machine, including a diesel engine and a gearbox.

Governor model

Instead of controlling the ship speed directly, it was chosen to control the engine speed. Controlling the engine speed via an engine speed governor is constantly applied in standard mechanical propulsion. The governor's input values are the desired and the actual engine speed: $n_{eng,set}$ and n_{eng}. Because the same case is used in this thesis, the desired engine speed is determined by the polar chart shown in Figure 2.6. These two input variables are normalized with the maximum engine speed before entering the PID controller. Subsequently, the difference between them is regarded as the non-dimension engine speed error. The output of the PID controller is the desired fuel rack setpoint X_{set}. At this point, fuel rack adjusting has to be introduced because the engine torque is generated from fuel mass injected to the cylinders at a given engine speed. The relation between the setting of the fuel rack, X_{set}, and the required fuel injected per cycle in kg, m_f, is:

$$m_{f,set} = X_{set} \cdot m_{f,nomi} \tag{2.17}$$

where $m_{f,nomi}$ is the nominal fuel injected per cycle [kg].

In this part, this nominal fuel injected per cycle is chosen to be the maximum fuel injected per cycle representing the maximum engine torque. Furthermore, to keep the model as simple as possible, it is assumed that there is no time delay caused by the inertia of the fuel pump actuator and the ignition delay. In this case, the fuel pump is not necessary to be included, and the setting of fuel rack can be calculated as:

$$X_{set} = \left(K_p \cdot \frac{n_{set} - n}{n_{max}} + K_i \cdot \int_0^t \frac{n_{set} - n}{n_{max}} dt + K_d \cdot \frac{d\frac{n_{set}-n}{n_{max}}}{dt} \right) \cdot X_{max} \tag{2.18}$$

where K_p is the proportional gain, K_i is the integral gain and K_d is the derivative gain.

Considering the maximum torque limited by the maximum fuel injected per cycle, a lookup table, including the torque limit of the diesel engine at each actual engine speed, is added and illustrated in Figure 2.10. In this way, the thermal overloading of this diesel engine can be prevented by selecting the minimum value between the PID controller's output and the lookup table.

Diesel engine model

Following the recommendations by [Eggers, 2016]: a more detailed engine model considering both the influence of engine torque rate and speed should be used, an analytical model of the diesel engine [Shi et al., 2010] that is also used in the case study [van der Kolk et al., 2019] is adopted because of no factory acceptance test (FAT)report for the given engine. Although its accuracy decreases at low loads and strong dynamic conditions, it does not make the model overcomplicated. Hence, the engine torque can be predicted based on engine speed and injected fuel per cycle as:

$$M_B^+ = 1 - C_0 \cdot (1 - n_e^+) + C_1 \cdot (1 - n_e^+)^2 - C_2 \cdot (1 - m_f^+) + C_3 \cdot (1 - m_f^+)^2 + C_4 \cdot (1 - n_e^+) \cdot (1 - m_f^+) \tag{2.19}$$

where the $'+'$ means the ratio between the actual value and nominal value so that

$$M_B^+ = \frac{M_B}{M_{b,nomi}} \tag{2.20}$$

$$n_e^+ = \frac{n_{eng}}{n_{eng,nomi}} \tag{2.21}$$

$$m_f^+ = \frac{m_f}{m_{f,nomi}} \tag{2.22}$$

By manually adjusting the five static operating points, those five coefficients,C_0,C_1,C_2,C_3,C_4, can be derived from five engine operating condition shown in Table 2.1, and they are -0.0113, -0.5619, 1.0501, -0.0496 and 0.1921 respectively. Hence, the engine torque can be function as a given injected fuel per cycle [kg] at a given engine speed. Furthermore, to obtain the engine's specific fuel consumption (SFC), the engine power P_b, injected fuel per second $\dot{m_f}$, and the SFC for each engine operating point can be calculated as:

$$P_b = M_b \cdot n_{eng} \tag{2.23}$$

$$\dot{m_f} = m_f \cdot n_{eng} \quad [g/s] \tag{2.24}$$

$$SFC = \frac{\dot{m_f} \cdot 3600000}{P_b} \quad [g/kWh] \tag{2.25}$$

Hence, an acceptable diesel engine model is properly built and its specific fuel consumption (SFC) is shown in Figure 2.14.

Engine operating point	n^+_{eng}	m^+_f	M^+_b
No.1	0.925	0.505	0.48
No.2	0.925	0.07	0.05
No.3	0.775	0.51	0.49
No.4	0.525	0.25	0.2
No.5	0.525	0.04	0

Table 2.1: Parameters for engine torque estimation.

Marine power transmission system model and shaft speed loop

The power transmission system connects the propulsor and prime movers by one or multiple line shafts and the gearbox. In this way, the torque generated by the engine can be transmitted properly to the propeller despite some power loss. Regarding the gearbox, a relatively simple gearbox model was used to keep the model as simple as possible. In addition to reducing the shaft speed to the required rotational speed required for the propeller, transmission system, such as the gear box, reduces the power generated by the diesel engine due to power loss in transmission process. Although the study [Godjevac et al., 2016] states that the loss from gearbox might be significant when the engine is in low load, a constant total transmission efficiency, η_{trm}, including the power loss due to gearbox and line shafts, is assumed because Figure 2.12 shows that the engine loading is not so low. Therefore, the power transmission process from the engine to the shaft can be represented as:

$$P_s = P_b \cdot \eta_{trm} \tag{2.26}$$

With a gearbox ratio defined as $i_{gb} = \frac{n_{eng}}{n_{shaft}}$, the shaft torque, M_s, can be calculated as:

$$M_s = M_b \cdot i_{gb} \cdot \eta_{trm} \tag{2.27}$$

Regarding the shaft speed loop, the shaft rotational dynamic behavior can be calculated by Newton's second law. The net torque, consisting of propeller and shaft torque, results in the shaft's angular acceleration. By integrating this angular acceleration, the shaft rotational speed, n_s is:

$$n_s = \frac{1}{2 \cdot \pi \cdot I_{total}} \int (M_s - M_{prop}) dt + n_{s,0} \tag{2.28}$$

where I_{total} is the total moment of inertia, and $n_{s,0}$ represents the initial shaft rotational speed.

Finally, after the engine speed governor, diesel engine and the gearbox system are built properly, the relationships between them from a bigger picture is shown in Figure 2.10.

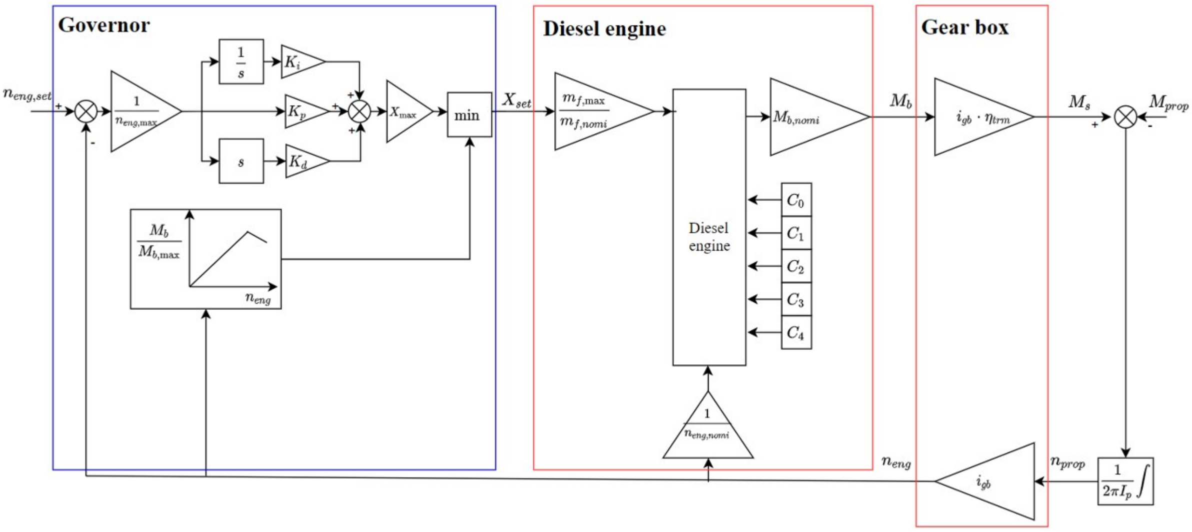

Figure 2.10: Overview of propulsion machine, governor model and shaft speed loop.

2.5. Add disturbances

As far as disturbances acting on the wind-assisted ship propulsion system are concerned, the disturbances that are mainly analyzed in this thesis are true wind speed (TWS) and wake (w) induced by wave amplitude. Both of the disturbances are implemented in the model by the way shown in Figure 2.11.

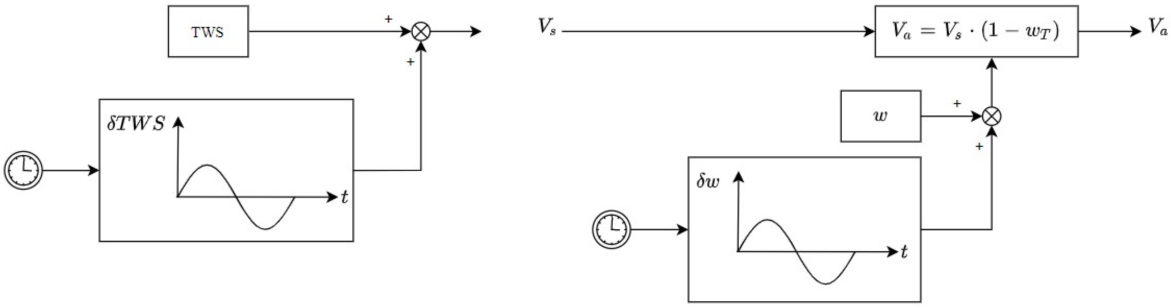

Figure 2.11: LHS: True wind disturbance. RHS: Propeller wake disturbance.

From Figure 2.11, the clock symbol means that the input for the disturbance block is a time step in the model. In each time step, the disturbance amplitude has its magnitude derived from the wind or wave spectrum shown in Chapter 4. In this way, regular and irregular disturbances can be represented. For example, in Figure 2.11, the disturbance for both true wind speed and wake are implemented as a sinusoidal disturbance. Similarly, the disturbance of ship resistance and true wind angle can also be applied in this way but in different blocks. Due to the scope of this thesis, they are not shown here.

2.6. Verification of simulation models

Verification is necessary to determine whether a computational model accurately represents the mathematical model and its solution. Although the nonlinear wind-assisted ship propulsion system for the selected case can not be validated because there are no any measurements from the wind-assisted ship, it still can be verified by inspecting the resemblance with the expectations of the model.

For a complex model consisting of many sub-models, it is suggested to verify the sub-models separately before connecting them together [Vrijdag et al., 2010]. Because an additional subsystem, a wind-assisted propulsion system including an apparent wind sub-model and a Flettner rotor sub-model, is added to the conventional propulsion system, this additional subsystem is firstly verified before connecting both of them. Furthermore, the static and dynamic inspection are also conducted to investigate the system's credibility, especially under this favor wind condition: true wind angle is 120 degrees.

2.6.1. Verification of sub models

To make a fair comparison, the ship speed and the spin ratio are set as constant values, which are 10 knots and 4, respectively. Subsequently, the polar chart regarding the apparent wind speed, apparent wind angle, the driving force (thrust) and the heeling force (side fore) under each wind condition are shown in Figure 2.12.

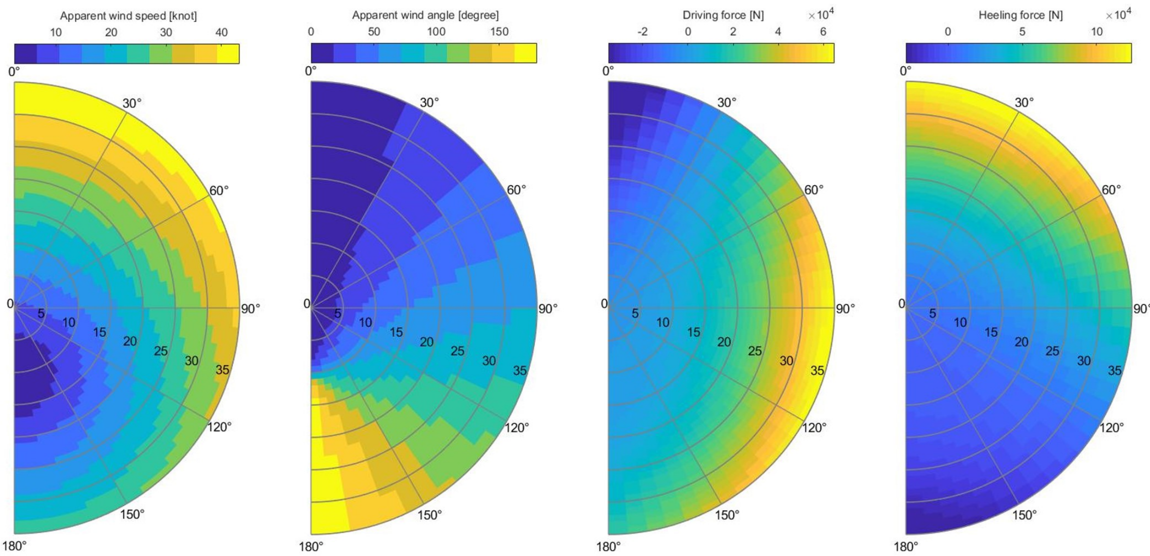

Figure 2.12: From the left-hand to the right-hand side, they are the result of apparent wind speed, apparent wind angle, driving force and heeling force under each true wind speed and true wind angle. Note that the unit used here for the true wind is knot.

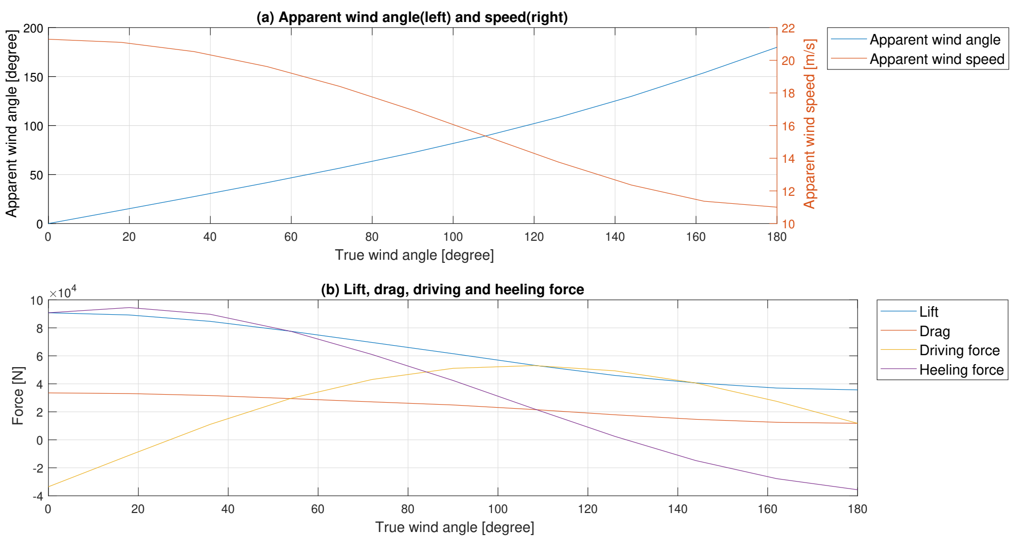

Figure 2.13: Simulation results of the sub-models at Beaufort scale 7.

To see the results more clearly when the true wind angle is 120 [degree], the results of the sub-models at Beaufort scale 7 is illustrated in Figure 2.13. Regarding the apparent wind model shown in the first part in Figure 2.13, inspection shows that as the true wind angle increases, the apparent wind angle also increases, whereas the apparent wind speed decreases. Furthermore, by inspecting the true wind angle at 0 and 180 [degree], the apparent wind angle is also 0 and 180 [degree], respectively. This can be explained by the fact that both the true wind vector under the two conditions and the ship velocity vector lie in the x-axis. Therefore, there is no difference between the true wind angle and the apparent wind angle. For the true wind angle between 0 degrees and 180 [degree], the apparent wind angle is lower because of the introduction of the ship velocity vector. Overall, the behavior of the apparent wind sub-model agrees with the expectations.

After the sub-model of the apparent wind model is built correctly, the properties of apparent wind "felt" by the Flettner rotor can be used for the next step: verification of the Flettner rotor sub-model. From Figure 2.13, it can be seen that the maximum driving force is generated by the Flettner rotor when the true wind angle is approximately 120 [degree]. Therefore, the minimum propeller torque and thus minimum engine torque is required to sail the ship at 10 knots. This result agrees well with the case study [van der Kolk et al., 2019] that the most fuel is saved in this region. On the other hand, if the spin ratio is still set at 4 instead of following the polar chart (shown in Figure 2.12) using a lower spin ratio when the true wind angle lies between 0 to 30 [degree], the heeling force becomes very large and negative driving force is generated. In this upwind condition, the study [van der Kolk et al., 2019] recommends that the Flettner rotor needs to be depowered, which means a lower spin ratio instead of 4 should be adopted. Therefore, when the undesired forces generated by the Flettner rotor are reduced by reducing the spin ratio, the rudder is capable of keeping the balance of ship, and the engine would not overload due to this additional drag force generated by the Flettner rotor. In conclusion, the sub model's behavior, consisting of apparent wind model and the Flettner rotor model, agrees not only well with the expectations but also the description in the study [van der Kolk et al., 2019].

2.6.2. Verification of overall model

Because the wind-assisted ship propulsion system model is mainly used to analyse the its dynamic behavior, especially for the engine performance at different Beaufort scales under a favorable true wind angle, the model is firstly verified in static condition by comparing its results with that used in the case study [van der Kolk et al., 2019] under the same condition. After the model in the static conditions is verified, a high level of confidence in the static behavior of the wind-assisted ship propulsion system model can be guaranteed, and then the verification of it in dynamic conditions is also conducted.

Verification of static operating points

To verify the model in static condition, seven engine operational conditions shown in Table 2.2 were selected. Furthermore, those engine operating points under each condition are shown in Figure 2.14.

Operational condition	True wind speed [knot]	Engine speed [rpm]	Engine power [kW]	Spin ratio [-]	F_{rotor}/F_{ship} [%]
11 [knot] at maximum engine speed at Bft.0	0	1000	1078.03	0	-0.32
10 [knot] at nominal engine speed at Bft.0	0	911	815.05	0	-0.32
10 [knot] at Bft.4	13.56	892	751.87	3	6
10 [knot] at Bft.5	18.95	872	688.70	3	12
10 [knot] at Bft.6	24.91	826	556.56	4	26
10 [knot] at Bft.7	31.39	762	400.25	4	44
10 [knot] at Bft.8	38.35	661	211.98	4	68

Table 2.2: Static engine operating points under different conditions.

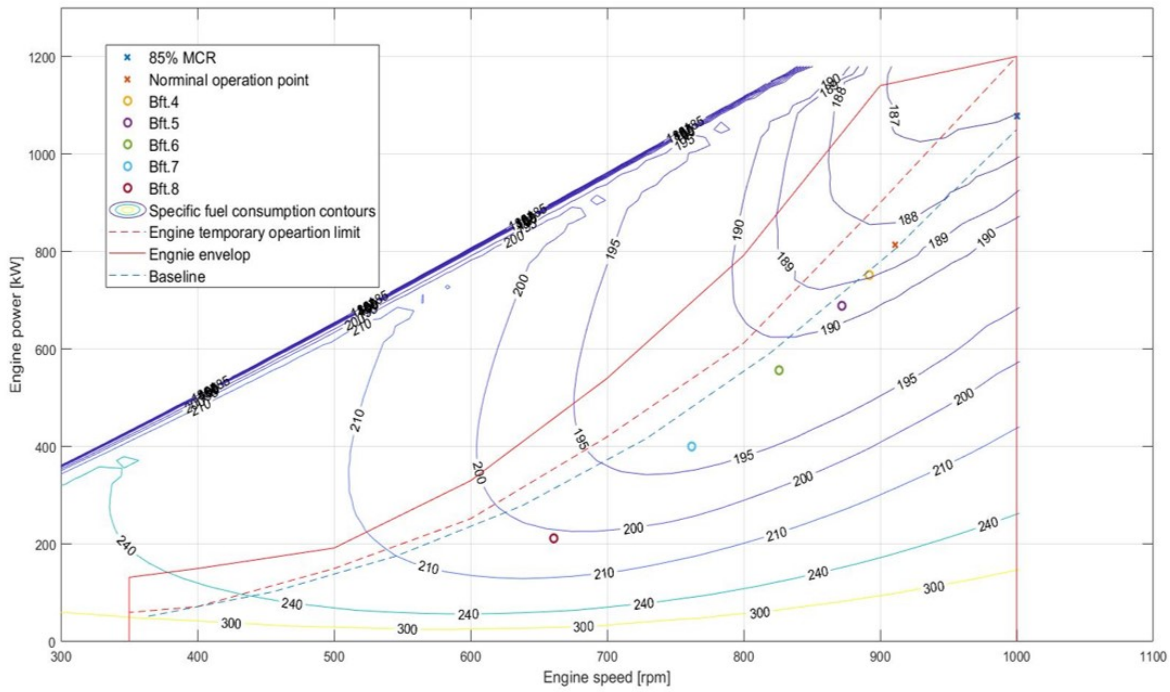

Figure 2.14: Engine static operating points at different Beaufort scales, it engine envelop, and SFC curves.

The first two operations are conditions that there is no wind and the rotor does not spin. Thus, both of the Beaufort scale and the spin ratio are zero. On the other hand, the other five conditions are the impact of wind on engine behavior when the Fletter spins and true wind angle is 120 [degree].

Regarding the first engine operating point, it can be seen that the required engine power at the maximum engine speed is not approximately 85% MCR as mentioned in the baseline design. The reason is that the additional drag force is induced due to the Flettner rotor. From Figure 2.4, the drag coefficient, C_d is nonzero although the spin ratio, k, is set to zero. Furthermore, according to Eq. (2.3), (2.4), (2.5) and (2.6), at Beaufort scale 0, which means there is no true wind, the apparent wind speed and apparent wind angle are the ship speed and 0 [degree]. This means that the ship sails directly into headwind. Consequently, the Flettner rotor at this apparent wind angle generates drag force instead of the desired driving force. Therefore, more engine power is required so that the ship can sail approximately 11 knots at its maximum engine speed.

Besides, to sail the ship speed at approximately 10 knots with the introduction of a Flettner rotor, the engine power and the engine speed decrease as the Beaufort scale increases at a favorable true wind angle. The phenomenon can be seen in Figure 2.14, and it is in line with expectations. According to Eq (2.7), the forces increase squarely due to the apparent wind speed so that relatively more wind energy can be used for generating driving force at the favorable true wind angle. As result, if the Beaufort scale becomes higher, which implies that the wind becomes stronger, less and less engine power is required for the ship to sail at 10 knots. Moreover, by comparing the engine speed and power shown in Figure 2.6 used in the case study with only one rotor [van der Kolk et al., 2019], the same trend for engine behavior can be found when the true wind angle is 120 [degree], and the engine speed and power from the simulation are also similar. Therefore, the derived model of WASP system is able to represent the conceptual model in a static situation.

Verification of dynamic behavior

After the static behavior of the wind-assisted ship propulsion system model is verified, a verification its dynamic behavior is carried in this section. To make a fair comparison, the Flettner rotor rotational speed is set as constant. In this condition, to evaluate the dynamic behavior of the system, especially the engine behavior in dynamic situations, three-step of the engine speed shown in Table 2.3 is used because the engine speed is the primary variable chosen to be mainly controlled in this thesis.

Because the engine speed governor gain settings also has an impact on the dynamic behavior of the engine, proper values of the proportional, K_p, the integral gain, K_i, and the derived gain, K_d, are necessary to be determined first. For the derived gain, K_d, it is set to zero in this case because it would normally amplify noises in reality, which makes the engine speed governor unstable in some situations. Besides, by manually adjusting the proportional, K_p, as well as the integral gain, K_i, the combination of $K_p = 1.2$ and $K_i = 1$ was found to be suitable because relatively less peak was found for both engine speed and engine torque, which is highly related to the position of the engine operating point in the engine envelop. Moreover, an acceptable rise-time, which means the time required for the engine response to rise from one to another, is also found. Consequently, the simulation results for nominal operation can be seen in Figure 2.15 and Figure 2.16.

Considering the impact of the wind on the wind-assisted ship propulsion system at its favorable true wind angle, four wind conditions from Beaufort scale 4 to 7 are chosen to evaluate the system response in terms of the engine speed, engine torque and the ship speed. When looking at Figure 2.15 and Figure 2.16, the same trend, the engine loading decreases as the wind speed increases at a favor wind angle, is found again. Moreover, compared with the nominal operational condition, Figure 2.15 shows that the ship speed increases at higher Beaufort scale, which means a rise in wind speed. Finally, during the transition of the three-step engine speed setting, Figure 2.16 shows that all the engine operating points lie in the engine envelop. Thus, it can be concluded that the derived model is capable of capturing the dynamic behavior of the system in terms of its engine speed, engine torque and ship speed.

	P/D [-]	Engine speed step (% of the maximum engine speed)
First step	0.85	59% to 78%
Second step	0.85	78% to 91%
Third step	0.85	91% to 58%

Table 2.3: Three steps of the engine step.

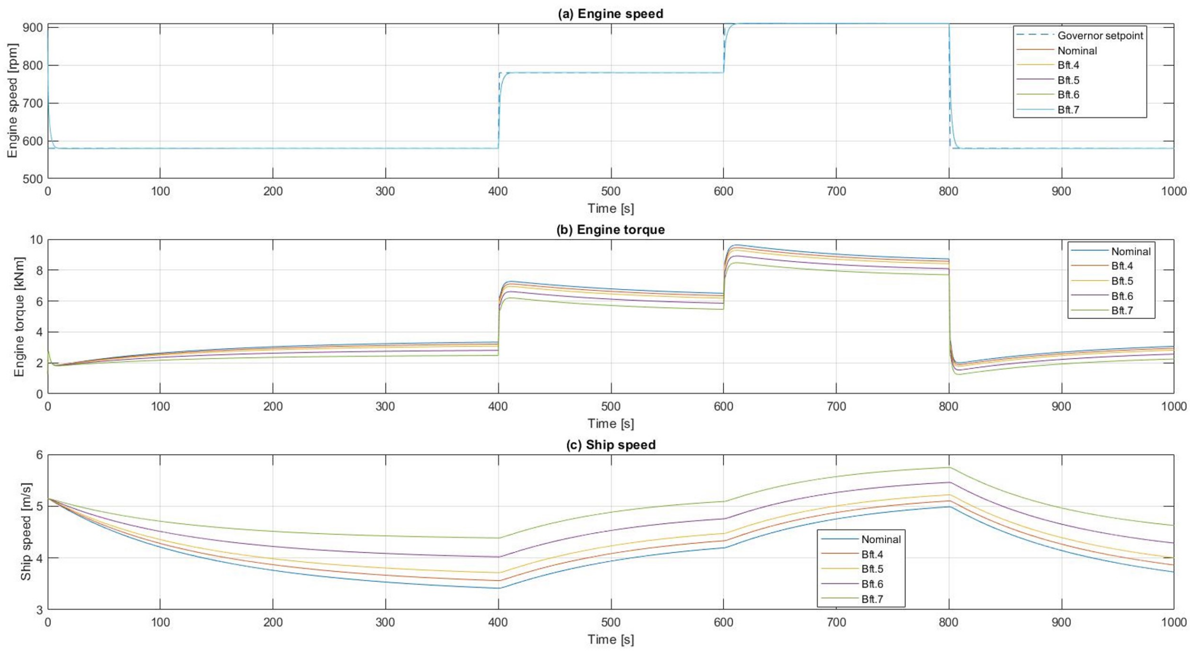

Figure 2.15: Response of the engine speed, torque and ship speed with given engine speed settings at each Beaufort scale.

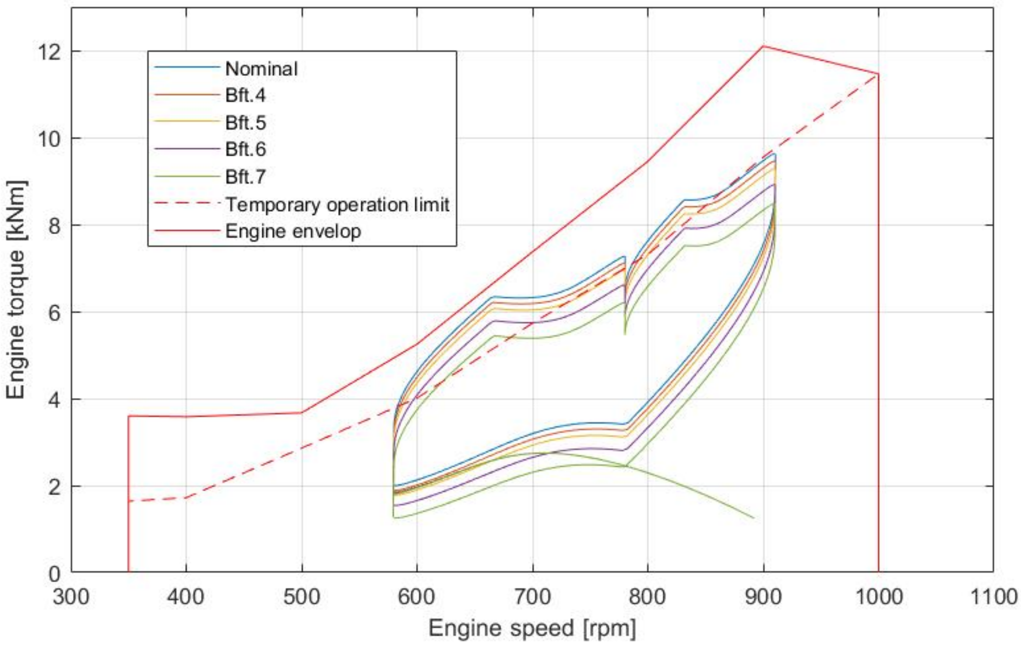

Figure 2.16: Response of the engine torque and speed to the three-step engine speed at different Beaufort scales.

2.7. Conclusions

Based on the simulation results in this chapter, it is clear that the derived nonlinear model is capable of capturing the wind-assisted ship propulsion behavior in terms of engine speed, engine torque(or power), and ship speed at different Beaufort scales. Under the favorable wind condition, the desired ship speed, 10 [knot], can be achieved with less engine speed and engine power.

Besides, with the verification, it enhances the confidence in the correct implementation of the model. Therefore, it is certain that the derived parametric propulsion system with a Flettner rotor can be further investigated, especially when the true wind angle is 120 [degree].

Finally, because the contribution from the Flettner rotor at Beaufort scale 6 and 7 are higher at its favorable true wind angle, it would be worth investigating the response of wind-assisted ship propulsion system to the disturbances from marine environment. Although less power and engine speed is required for the wind-assisted ship to sail at 10 [knot] when Beaufort scale is 8, [van der Kolk et al., 2019] states that the wind speed under this condition turns the sea into an unrealistic storm sea. This implies that the wind-assisted ship probably can not be operated well under this circumstance. Moreover, according to the literature [Tsujimoto and Orihara, 2019], the weather condition of Beaufort scale 6 and 7 do not make the master reduce the normal ship speed and heading. Therefore, under the favorable wind speed (True wind angle is 120 [degree], the dynamic behaviors of the wind-assisted ship propulsion system at Beaufort scale 6 and 7 are investigated in the following chapters.

Chapter 3

Linearisation of a wind-assisted ship propulsion system model

3.1. Introduction

After verifying the nonlinear wind-assisted ship simulation model, a relatively high level of confidence can be guaranteed when analyzing the system's dynamic behavior. Although real systems are nonlinear, the usage of a linearized model can be regarded as an additional tool to analyze and provides considerable insight, especially for systems' behavior near the equilibrium point in the frequency domain. Furthermore, linearised models reveal a more transparent relationship among parameters, and thus the main parameters or variables governing the dynamic behavior could be found. However, a linearised model is only valid in the neighborhood of its equilibrium. In other words, the linearised model might not be accurate if the perturbations around its equilibrium point are high to a certain amount. Despite the limitation of the linearised model, it is still applied in many fields of engineering [Stapersma and Vrijdag, 2017]. Hence, to investigate the responses of the wind-assisted ship propulsion system's to the disturbances from the marine environment and the relations between parameters, the nonlinear model derived in Chapter 2 was linearized and normalized.

To derive and verify the linearised wind-assisted ship propulsion system model , the procedure shown in Figure 3.1 was carried out in three steps:

- Core propulsion system: Verification of the linearised core propulsion model with the linearised wind-assisted propulsion sub-model and without the actuator (the diesel engine) and the controller (engine speed governor).
- Uncontrolled system with actuator: Verification of the linearised core propulsion model with the linearised wind-assisted propulsion sub-model and actuator(the diesel engine) and without the controller (engine speed governor).
- Controlled system: Verification of the linearised core propulsion model with the linearised wind-assisted propulsion sub-model, actuator (the diesel engine), and the controller (engine speed governor).

By following the three steps, more confidence can be guaranteed for each linearised model before connecting all of them. The difference between each model can also be compared in order to investigate the system performance when the controller is used.

The detailed verification process is that the responses of the linearised system to disturbances from marine environment were compared with that of the nonlinear system. According to the research [Vrijdag and Stapersma, 2017], there are two approaches for obtaining the system response to a given input signal. The first approach was using transfer function adopted in the research [Stapersma and

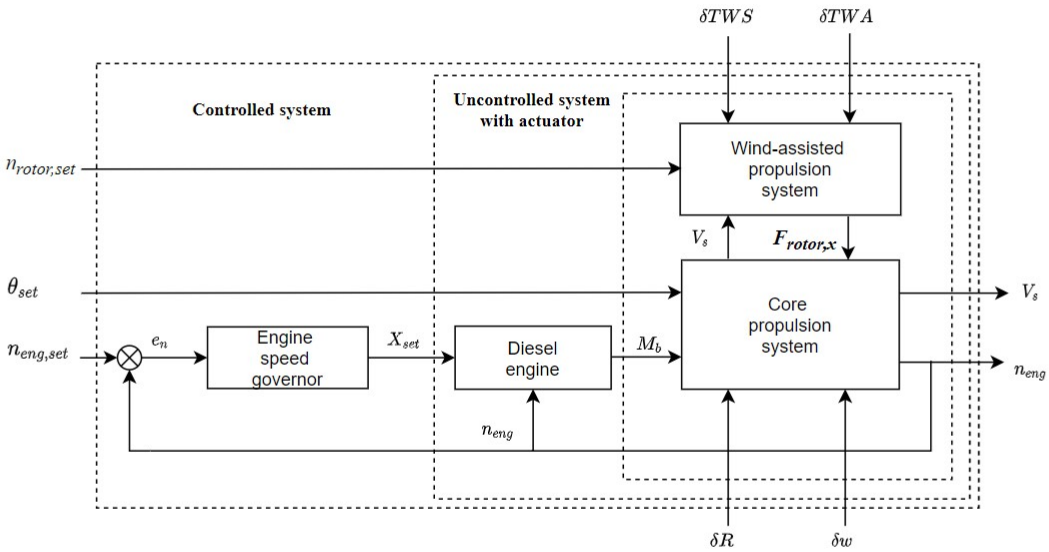

Figure 3.1: Block diagram for inputs and outputs of the system at each level.

Vrijdag, 2017], whereas the second approach was using State-Space notation that applied in [Vrijdag and Stapersma, 2017] and [Vrijdag and Schuttevaer, 2019]. In this thesis, it was chosen to obtain the system response by applying State-Space notation, which can be used to obtain the system Bode magnitude plot, because using State-Space notation is relatively less laborious. The State-Space form used in this thesis is given by:

$$\begin{aligned} \dot{x} &= Ax + Bu + Gw \\ y &= Cx + Du \end{aligned} \tag{3.1}$$

where the first equation represents the state equation, and the second one is output equations. Furthermore, for the first equation, A is the system matrix, B is the input matrix, and G is the matrix representing disturbances from the marine environment. For the second equation, C and D are the output matrix and feed-forward matrix. Finally, the x, u, w, and y represent the state vector, input vector, disturbance vector, and output vector.

Finally, based on the derived State-Space model, the Bode magnitude plot can be made by implementing it in MATLAB. Hence, the dynamic behavior of the wind-assisted ship propulsion system can be analyzed in the frequency domain, which helps understand how the system is sensitive to the disturbances marine environment, especially for the wind and wake induced by waves.

3.2. Normalisation and linearisation

3.2.1. Linearisation process

Before linearising the system, the characteristics of the non-linear system should be noticed. According to the literature [Stapersma and Vrijdag, 2017], the non-linearities can be classified into three types:

- Curvilinear correlation exists in the characteristics of models. One clear example is the propeller open water diagram using the K_T and K_Q curve. Another clear example is the diagram regarding the lift and drag coefficient at different spin ratios.

- Multiplicative operator exists in the mathematical model of the system. One clear example is the calculation of propeller performance: propeller thrust, $T = \rho \cdot n^2 \cdot D^4 \cdot K_T$

- System hard limit exits in some components, such as limits resulting from the protective mechanism in the engine governor, are active.

3.2.2. A general approach for normalisation and linearisation

Following the approach derived in [Stapersma and Vrijdag, 2017], the same notation is used and a short introduction of a certain function Z is given here as:

$$Z = c \cdot Y^e \cdot X \tag{3.2}$$

where c and e are a constant multiplier and a constant exponent. The, Z, in an equilibrium point, is:

$$Z_0 = c \cdot Y_0^e \cdot X_0 \tag{3.3}$$

Normalisation of Eq. (3.2) and Eq. (3.3) gives:

$$\frac{Z}{Z_0} = \left(\frac{Y}{Y_0}\right)^e \cdot \frac{X}{X_0} \tag{3.4}$$

By defining $X^* \equiv \frac{X}{X_0}, Y^* \equiv \frac{Y}{Y_0}$, and $Z^* \equiv \frac{Z}{Z_0}$, Eq. (3.4) can be written as:

$$Z^* = Y^{*e} \cdot X^* \tag{3.5}$$

Near equilibrium point, dX, dY and dZ can be approximated as $\delta X, \delta Y$ and δZ. Division of$X = X_0 + \delta X$ by X_0 gives $\frac{X}{X_0} = 1 + \frac{\delta X}{X_0}$ and likewise $\frac{Y}{Y_0} = 1 + \frac{\delta Y}{Y_0}$. Based on [Stapersma and Vrijdag, 2017], using Taylor series expansion and ignoring terms which are higher than the first order turn Eq. (3.5) into:

$$\frac{\delta Z}{Z_0} = \frac{\delta X}{X_0} + e \cdot \frac{\delta Y}{Y_0} \tag{3.6}$$

Defining a new representation:

$$\delta Z^* \equiv \frac{\delta Z}{Z_0} \tag{3.7}$$

Eq. (3.6) becomes:

$$\delta Z^* = \delta X^* + e \cdot \delta Y^* \tag{3.8}$$

This physical meaning of Eq. (3.8) is that a variation of output Z is relative to the variations of inputs X and Y. Moreover, the constant, e, that present as an exponent in the original Eq. (3.2) becomes a constant multiplication factor. In addition, it can also be seen that the multiplication of X and Y become a summation. These two mathematical techniques used in the approach enable the original nonlinear mathematical models to be linearised and simpler.

3.2.3. The ship speed loop

With the introduction of the Flettner rotor and assumption of constant ship mass, the differential equation that describes the dynamic behavior of the ship speed loop in surge direction is:

$$m_{ship} \cdot \frac{\mathrm{d}V_s}{\mathrm{d}t} = F_{rotor,x} + F_{prop} - F_{ship} \tag{3.9}$$

As derived in A.1 in Appendix A, the normalised and linearised version of Eq. (3.9) is:

$$\tau_v \cdot \frac{\mathrm{d}V_s^*}{\mathrm{d}t} = \kappa_{rotor} \cdot \delta F_{rotor,x}^* + \kappa_{prop} \cdot \delta F_{prop}^* - \delta F_{ship}^* \tag{3.10}$$

where τ_v is given in Appendix A.1 and

$$\kappa_{rotor} = \frac{F_{rotor,x,0}}{F_{ship,0}}, \quad \kappa_{prop} = \frac{F_{prop,0}}{F_{ship,0}} \tag{3.11}$$

The Flettner rotor

Regarding the driving force generated by the Flettner rotor, $F_{rotor,x}$, its variation is mainly relative to the variations of true wind speed TWS, true wind angle TWA, and ship speed V_s if the rotor spins at a constant speed. Despite the variation of apparent wind speed that flows into the Flettner rotor, it's rotational speed is derived from the static wind condition, and thus it is fixed. Therefore, there are no variations in the Flettner rotor's rotational speed. In this condition, the normalized and linearised version of the Flettner rotor was derived in Appendix A, and it is:

$$\delta F_{rotor,x}^* = \lambda_{TWS} \cdot \delta TWS^* + \lambda_{TWA} \cdot \delta TWA^* + \lambda_{VS} \cdot \delta V_s^* \tag{3.12}$$

where λ_{TWS}, λ_{TWA}, and λ_{VS} are coefficients derived in Appendix A.

The propeller

Regarding the propeller thrust F_{prop}, the variation of propeller thrust to the variation of open water thrust T, including the thrust deduction factor t and number of the propeller k_p, is:

$$F_{prop} = k_p \cdot (1-t) \cdot T \xRightarrow{\text{t=const}} \delta F^*_{prop} = \delta T^* \tag{3.13}$$

Concerning the open water thrust in normalised and linearised from, it can be further obtained by:

$$T = K_T \cdot \rho \cdot n^2 \cdot D^4 \Rightarrow \delta T^* = 2 \cdot \delta n^* + \delta K^*_T \tag{3.14}$$

The thrust coefficient, K_T, is a function of the advance ratio J and the propeller pitch θ. The variation of the thrust coefficient in normalised form can be approximated as:

$$\delta K^*_T = a \cdot \delta J^* + p \cdot \delta \theta^* \tag{3.15}$$

where a and p are defined as:

$$a \equiv \frac{J_0}{K_{T,0}} \cdot \left.\frac{\delta K_T}{\delta J}\right|_{\theta}, p \equiv \frac{\theta_0}{K_{T,0}} \cdot \left.\frac{\delta K_T}{\delta \theta}\right|_{J} \tag{3.16}$$

The normalisation and linearisation of advance ratio J can be obtained by:

$$J = \frac{V_a}{n \cdot D} \Rightarrow \delta J^* = \delta V^*_a - \delta n^* \tag{3.17}$$

where the advance velocity V_a can be relative to wake w and ship speed as:

$$V_a = (1-w) \cdot V_s \Rightarrow \delta V^*_a = \delta V^*_s - \delta w^* \tag{3.18}$$

Following the research [Vrijdag and Stapersma, 2017], the normalisation of wake is calculated differently than other variables and it is normalised by $1 - w_0$ which delivers:

$$\delta w^* = \frac{\delta w}{1 - w_0} \tag{3.19}$$

Finally, the variation of propeller thrust can be obtained by substitution of Eq. (3.14), Eq. (3.15), Eq. (3.17) and Eq. (3.18) into Eq. (3.13) , which gives the relation between the linearised and normalised of propeller thrust and other variables as:

$$\delta F^*_{prop} = (2-a) \cdot \delta n^* + a \cdot \delta V^*_s - a \cdot \delta w^* + p \cdot \delta \theta^* \tag{3.20}$$

where the coefficient a and p are given in [Stapersma and Vrijdag, 2017].

The ship resistance

Following the study [Vrijdag and Stapersma, 2017], the ship resistance curve $R(V_s)$ can be normalised and linearised as:

$$F_{ship} = R = \alpha \cdot V^e_s \Rightarrow \delta F^*_{ship} = \delta R^* = \delta \alpha^* + e \cdot \delta V^*_s \tag{3.21}$$

where the normalised constant e is formally defined as:

$$a \equiv \frac{V_{s,0}}{R_0} \cdot \left.\frac{\delta R}{\delta V_{s,0}}\right|_{\alpha} \tag{3.22}$$

Finally, by substitution of Eq. (3.12), Eq. (3.20) and Eq. (3.21) into Eq. (3.10), the normalisation and linearisation of the ship speed loop can be written as:

$$\begin{aligned} \tau_v \cdot \frac{\mathrm{d}V^*_s}{\mathrm{d}t} = \big(\kappa_{prop} \cdot (2-a)\big) \cdot \delta n^* + (\kappa_{rotor} \cdot \lambda_{vs} + \kappa_{prop} \cdot a - e) \cdot \delta V^*_s + \\ (-1) \cdot \delta \alpha^* + (-\kappa_{prop} \cdot a) \cdot \delta w^* + (\kappa_{rotor} \cdot \lambda_{TWS}) \cdot \delta TWS^* + (\kappa_{rotor} \cdot \lambda_{TWA}) \cdot \delta TWA^* \end{aligned} \tag{3.23}$$

3.2.4. The shaft speed loop

From the previous sections, it can be noticed that the thrust generated by the Flettner rotor only influences the ship speed loop. As a result, despite the Flettner rotor was introduced in the conventional marine propulsion system, there is no modification required for the shaft speed loop. Hence, based on the literature [Vrijdag and Stapersma, 2017], with the assumption of constant shaft inertia, the differential equation of the dynamic shaft speed loop is:

$$2 \cdot \pi \cdot \frac{dn}{dt} = M_s - M_{prop} \tag{3.24}$$

According to the research [Stapersma and Vrijdag, 2017], in the steady condition that there is equilibrium for shaft and propeller torque, Eq. (3.24) can be linearsied and normalised as:

$$\tau_n \frac{\mathrm{d}n^*}{\mathrm{d}t} = \delta M_b^* - \delta M_{prop}* \tag{3.25}$$

where the integration constant of the normalised shaft speed τ_n as well as time derivative are defined as:

$$\tau_n \equiv \frac{2 \cdot \pi \cdot I_p \cdot n_0}{M_{s,0}} \tag{3.26}$$

$$\frac{dn^*}{dt} = \frac{1}{n_0} \cdot \frac{dn}{dt} \tag{3.27}$$

Shaft torque

Regarding the shaft torque, it can be related to brake engine torque via the gearbox reduction i_{gb} and the transmission efficiency η_{trm}. With the assumption of constant transmission efficiency, the linearized and normalized of shaft torque can be related to that of the brake engine torque as:

$$M_s = i_{gb} \cdot \eta_{trm} \cdot M_b \Rightarrow \delta M_s^* = \delta M_b^* \tag{3.28}$$

Propeller torque

Regarding the torque delivered by the propeller, the variation of propeller torque can be related to open water torque by assuming a constant relative rotative efficiency η_r as:

$$M_{prop} = \frac{Q}{\eta_r} \xRightarrow{\eta_r = const} \delta M_{prop}^* = \delta Q^* \tag{3.29}$$

where $Q = K_Q \cdot \rho \cdot n^2 \cdot D^5$, and it can be linearised and normalised as:

$$\delta Q^* = 2 \cdot \delta n^* + \delta K_Q^* \tag{3.30}$$

Regarding the open water torque coefficient K_Q, it can be expressed as:

$$\frac{\delta K_Q}{K_{Q,0}} = b \cdot \frac{\delta J}{J_0} + q \cdot \frac{\delta \theta}{\theta_0} \tag{3.31}$$

in which the normalised propeller derivatives b and q are defined as:

$$b \equiv \frac{J_0}{K_{Q,0}} \cdot \left.\frac{\delta K_Q}{\delta J}\right|_{\theta}, \quad q \equiv \frac{\theta_0}{K_{Q,0}} \cdot \left.\frac{\delta K_Q}{\delta \theta}\right|_{J} \tag{3.32}$$

Following the same procedure for deriving the propeller thrust, the variation of propeller torque is:

$$\delta M_{prop}^* = (2 - b) \cdot \delta n^* + b \cdot \delta V_s^* - b \cdot \delta w^* + q \cdot \delta \theta^* \tag{3.33}$$

Finally, by substitution of Eq. (3.28) and Eq. (3.33) into Eq. (3.25), the normalisation and linearisation of the shaft speed loop can be written as:

$$\tau_n \frac{\mathrm{d}n^*}{\mathrm{d}t} = \delta M_b^* - b \cdot \delta V_s^* + (-2 + b) \cdot \delta n^* + b \cdot \delta w^* - q \cdot \delta \theta^* \tag{3.34}$$

3.2.5. Overview of the linearised model and its limits

From the previous sections, various assumptions were made so that the system can be linearized. A quick overview of the assumptions used in the linearised model and it's limitations currently are summarized below:

- The linearised model provides reliable insight into the system when there is a small variation around the equilibrium. Furthermore, no hard limits, such as the engine envelop, are touched [Vrijdag and Stapersma, 2017].

- The propeller performance was simplified as a 1-dimensional version, instead of an actual 3-dimensional wakefield, due to the usage of the open water diagram. This implies that the impact of tangential and radial wake velocity on propeller thrust and torque are not considered in the model.

- Due to the usage of an open water diagram, the propeller is regarded as a non-dynamic element [Vrijdag and Stapersma, 2017].

- The variation of rotational speed for the Flettner rotor was not incorporated in this linearised model. That is, the Flettner rotor spins at a constant rotational speed despite true wind speed variation.

Recalling Figure 3.1 representing the nonlinear system at three levels and following the previous sections regarding linearised sub models, an overview of the linearised system in normalized form is illustrated in Figure 3.2.

Moreover, the variables and parameters of the two operational condition based on the conclusion from Chapter 1 are presented in Table 3.1.

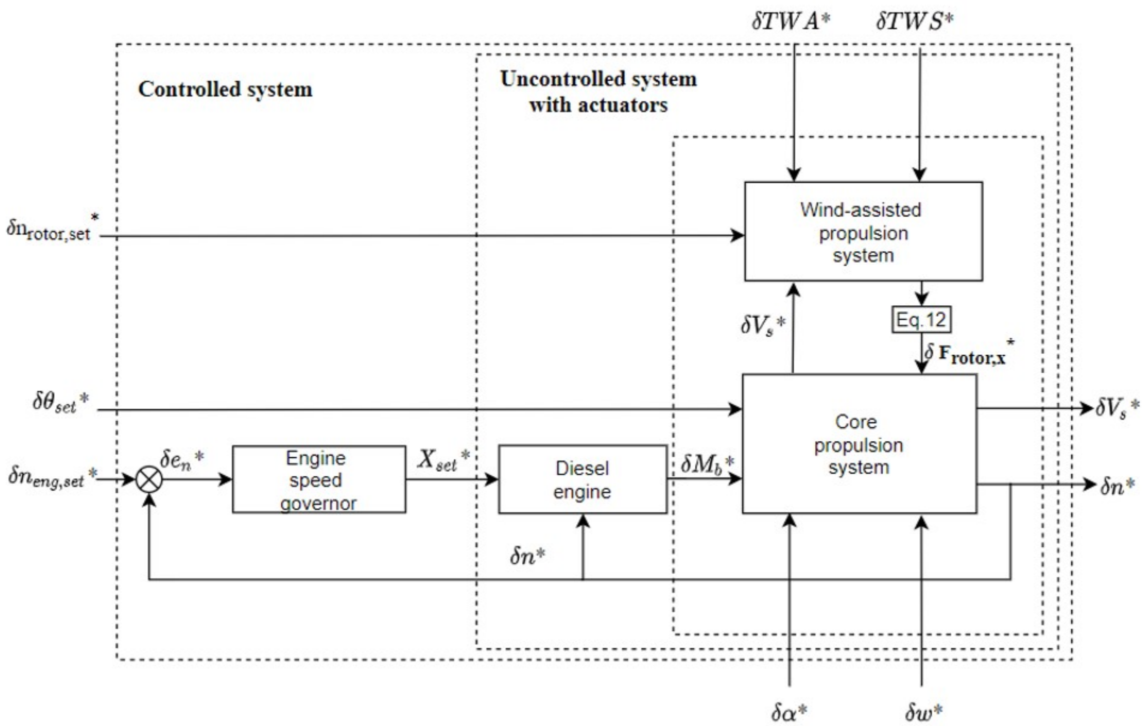

Figure 3.2: Block diagram illustrating the inputs and outputs for the linearised model at three levels.

System parameters	Bft.6	Bft.7	Units of parameters
Core systems with wind-assisted propulsor			
I_{total}	4500	4500	$[kg\ m^2]$
m_{ship}	7180000	7180000	[kg]
$(P/D)_0$	0.85	0.85	[-]
n_0	13.7	12.7	$[s^-1]$
k_0	4	4	[-]
$V_{s,0}$	5.144	5.144	[m/s]
$M_{b.0}$	6434.31	5015.85	[Nm]
$F_{ship,0}$	117458.50	117388.49	[N]
$F_{prop,0}$	86732.14	66023.57	[N]
$F_{rotor,x,0}$	30726.35	51364.92	[N]
J_0	0.5178	0.5611	[-]
$K_{T,0}$	0.1866	0.1669	[-]
$K_{Q,0}$	0.0272	0.0249	[-]
a	-1.249	-1.5423	[-]
b	-0.9915	-1.2024	[-]
p	2.3355	2.6095	[-]
q	2.8168	2.9861	[-]
e	2	2	[-]
κ_{prop}	0.7384	0.5624	[-]
κ_{rotor}	0.2616	0.4376	[-]
κ_c	1.695	1.9788	[-]
λ_{TWS}	1.2487	1.2714	[-]
λ_{TWA}	-1.1373	-0.8733	[-]
λ_{VS}	-0.0618	-0.0874	[-]
τ_n	1.453	1.7195	[s]
τ_v	314.5259	314.6197	[s]
Uncontrolled system with actuator and wind-assisted propulsor			
g	-0.0135	-0.0159	[-]
v	1.0636	1.0781	[-]

Table 3.1: Parameters and variables of the linearised model at different levels.

According to Table 3.1 and Eq. (3.12), it can also be noticed that a further increase of true wind angle and ship speed around the equilibrium leads to a decrease of the thrust variation generated by the Flettner rotor. This is because λ_{TWA} and λ_{vS} are negative for this two conditions.

3.3. Core propulsion system

3.3.1. Linearised model

Following the first step mentioned in Section 3.1, the verification process of the core propulsion system, including the additional wind-assisted system, is shown in this section. This is achieved by comparing the linearized model's response to disturbance of wind and wake with that of the nonlinear model in the frequency domain.

Regarding the linearized model, the linearisation process of the core propulsion system and the wind-assisted system are already presented in Section 3.2. Based on the ship speed loop (Eq. (3.23)) and the shaft speed loop (Eq. (3.34)), the linearized model for the core propulsion system with the wind-assisted propulsion system can be written in the State-Space model form as:

$$A = \begin{bmatrix} \frac{-2+b}{\tau_n} & \frac{-b}{\tau_n} \\ \frac{\kappa_{prop}\cdot(2-a)}{\tau_v} & \frac{\kappa_{rotor}\cdot\lambda_{vs}+\kappa_{prop}\cdot a-e}{\tau_v} \end{bmatrix} \tag{3.35}$$

$$B = \begin{bmatrix} \frac{1}{\tau_n} & \frac{-q}{\tau_n} \\ 0 & \frac{\kappa_{prop} \cdot p}{\tau_v} \end{bmatrix} \tag{3.36}$$

$$C = \begin{bmatrix} 1 & 0 \\ 0 & 1 \end{bmatrix} \tag{3.37}$$

$$D = \begin{bmatrix} 0 & 0 \\ 0 & 0 \end{bmatrix} \tag{3.38}$$

$$x = y = \begin{bmatrix} \delta n^* \\ \delta V_s^* \end{bmatrix}, u = \begin{bmatrix} \delta M_b^* \\ \delta \theta^* \end{bmatrix} \tag{3.39}$$

$$w = \begin{bmatrix} \delta \alpha^* \\ \delta w^* \\ \delta TWS^* \\ \delta TWA^* \end{bmatrix} \tag{3.40}$$

$$G = \begin{bmatrix} 0 & \frac{b}{\tau_n} & 0 & 0 \\ \frac{-1}{\tau_v} & \frac{-\kappa_{prop} \cdot a}{\tau_v} & \frac{\kappa_{rotor} \cdot \lambda_{TWS}}{\tau_v} & \frac{\kappa_{rotor} \cdot \lambda_{TWA}}{\tau_v} \end{bmatrix} \tag{3.41}$$

Eq. (3.39) shows that the variations of the shaft speed and ship speed are the outputs of the model. On the other hand, the State-Space model's inputs are the variation of true wind speed disturbance and wake disturbance.

To investigate the linearised model's performance, the Bode magnitude plots for the engine speed and ship speed can be obtained by implementing the State-Space model in MATLAB. As the results, the linearized system's sensitivity function for the responses of the engine speed and the ship speed to the variation of true wind speed and wake at Beaufort scale 6 and 7 are shown in Figure 3.3, and their parameters are given in Table 3.1 presented in Section 3.2.5.

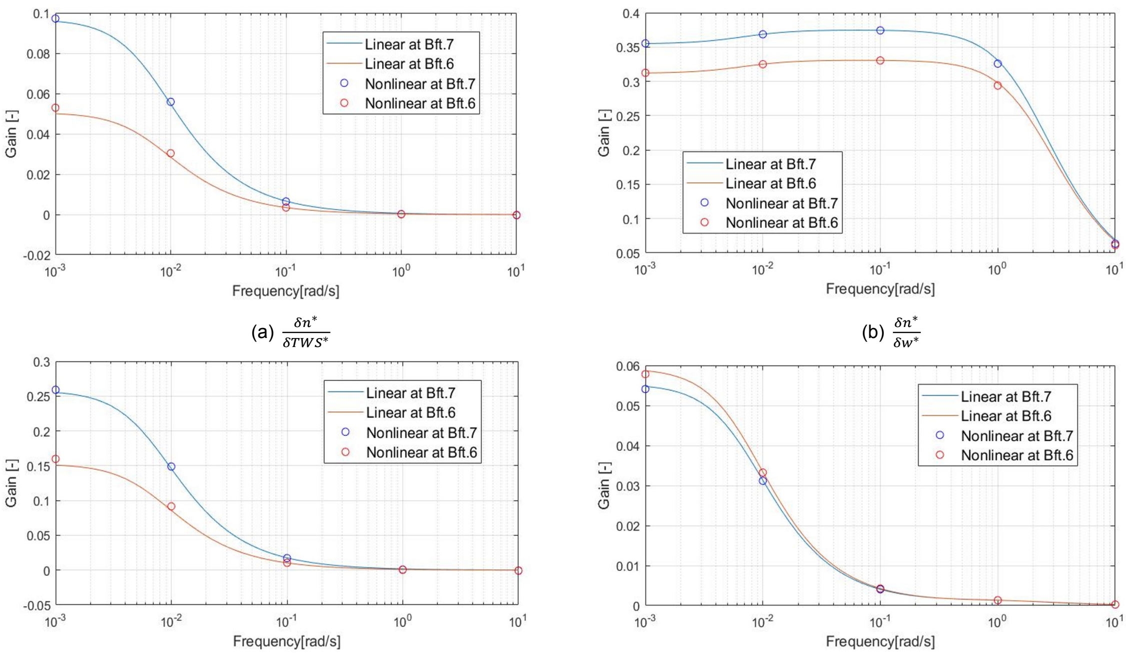

(a) $\frac{\delta n^*}{\delta TWS^*}$ (b) $\frac{\delta n^*}{\delta w^*}$

(c) $\frac{\delta V_S^*}{\delta TWS^*}$ (d) $\frac{\delta V_S^*}{\delta w^*}$

Figure 3.3: Bode magnitude plots of shaft speed and ship speed at Beaufort scale 6 and 7 for the linearised model (solid line) and nonlinear model (dot) of the core propulsion system including wind-assisted propulsion model.

3.3.2. Verification of linearised model

In Figure 3.3, the dots represent the nonlinear model's responses at to variation of true wind speed and wake at each frequency. This is achieved by giving true wind speed and wake fraction in sinusoidal form with a fixed amplitude and frequency from 0.001 to 10 [rad/s] at the equilibrium point. That is, those two regular disturbances can be implemented in the nonlinear model in the way shown in Figure 2.11. As the result, the engine speed and ship speed that are the outputs from the nonlinear model will be in the sinusoidal form in time-domain simulation after the nonlinear model reaches its steady state. Regarding the variation of the values, the magnitude of the sinusoidal output signals can be divided with its equilibrium value so that it can be compared with outputs from the linearised model.

To get a feeling of how to interpret the Bode magnitude plots, an example is given here: For the core propulsion system, the gain of $\frac{\delta n^*}{\delta TWS^*}$ is approximately 0.3 at a frequency of 0.01 [rad/s], which indicates that a sinusoidal true wind speed variation of 10 % at that frequency leads to a sinusoidal variation of engine speed of 3 %. With the interpretation in mind, some observations will be made in Section 3.6.

In conclusions, according to Figure 3.3 (a), 3.3 (b), 3.3 (c) and 3.3 (d), it can be noticed that the derived lineariesed model's responses of engine speed and ship speed to the true wind speed variation and wake variation agree very well with that of the nonlinear model, which indicates that the derived linearised model for core propulsion system with the additional wind-assisted system can be used further.

3.4. Uncontrolled system with actuators

While the derivation so far is correct, the second step is adding actuators that drive the shaft and ship speed loop. According to the research [Vrijdag and Stapersma, 2017], the actuators are the engine and the CPP (controllable pitch propellers) hydraulic system, which provide M_b or δM_b^* as the inputs at the engine side whereas θ or $\delta\theta^*$ at the propeller side.

Because the diesel engine's response is the main focus in this thesis, it is decided to model and linearised the diesel engine only. Compared with the diesel engine model used in the literature [Vrijdag and Stapersma, 2017], another engine model [Shi et al., 2010] was adopted in this thesis, which implies that a new linearised diesel engine model is required to be derived. As shown in Appendix B, Eq. (2.19) can be linearized and normalized as:

$$\delta M_b^* = g \cdot \delta n^* + v \cdot \delta X_{set}^* \tag{3.42}$$

where g and v are given in Appendix B. Regarding the CPP hydraulic system and following the literature [Vrijdag and Stapersma, 2017], if a CPP is used, the differential equation for the propeller pitch is given as:

$$\tau_\theta \cdot \frac{d\theta^*}{dt} = \delta\theta_{set}^* - \delta\theta^* \tag{3.43}$$

By substituting Eq. (3.42) into Eq. (3.28) and adding Eq. (3.43) , the Space-State model of the uncontrolled system with actuators and wind-assisted propulsion system can be derived as:

$$A = \begin{bmatrix} \frac{-2+b+g}{\tau_n} & \frac{-b}{\tau_n} & \frac{-q}{\tau_n} \\ \frac{\kappa_{prop}\cdot(2-a)}{\tau_v} & \frac{\kappa_{rotor}\cdot\lambda_{Vs}+\kappa_{prop}-e}{\tau_v} & \frac{\kappa_{prop}\cdot p}{\tau_v} \\ 0 & 0 & \frac{-1}{\tau_\theta} \end{bmatrix} \tag{3.44}$$

$$B = \begin{bmatrix} \frac{v}{\tau_n} & 0 \\ 0 & 0 \\ 0 & \frac{1}{\tau_\theta} \end{bmatrix} \tag{3.45}$$

$$C = \begin{bmatrix} 1 & 0 & 0 \\ 0 & 1 & 0 \\ 0 & 0 & 1 \end{bmatrix} \tag{3.46}$$

$$D = \begin{bmatrix} 0 & 0 \\ 0 & 0 \\ 0 & 0 \end{bmatrix} \tag{3.47}$$

$$x = y = \begin{bmatrix} \delta n^* \\ \delta V_s^* \\ \delta \theta^* \end{bmatrix}, u = \begin{bmatrix} \delta X_{set}^* \\ \delta \theta_{set}^* \end{bmatrix} \tag{3.48}$$

$$w = \begin{bmatrix} \delta \alpha^* \\ \delta w^* \\ \delta TWS^* \\ \delta TWA^* \end{bmatrix} \tag{3.49}$$

$$G = \begin{bmatrix} 0 & \frac{b}{\tau_n} & 0 & 0 \\ \frac{-1}{\tau_v} & \frac{-\kappa_{prop} \cdot a}{\tau_v} & \frac{\kappa_{rotor} \cdot \lambda_{TWS}}{\tau_v} & \frac{\kappa_{rotor} \cdot \lambda_{TWA}}{\tau_v} \\ 0 & 0 & 0 & 0 \end{bmatrix} \tag{3.50}$$

To verify the derived linearised model with actuators and the wind-asissted propulsion system, the same procedure presented in Section 3.3 for obtaining the system's sensitivity function in for the responses of the engine speed and ship speed to variation of true wind speed and wake was carried out. As the results, the linearized system's sensitivity function in terms of the engine speed and the ship speed at Beaufort scale 6 and 7 are shown in Figure 3.4 and their parameters are given in Table 3.1 presented in Section 3.2.5.

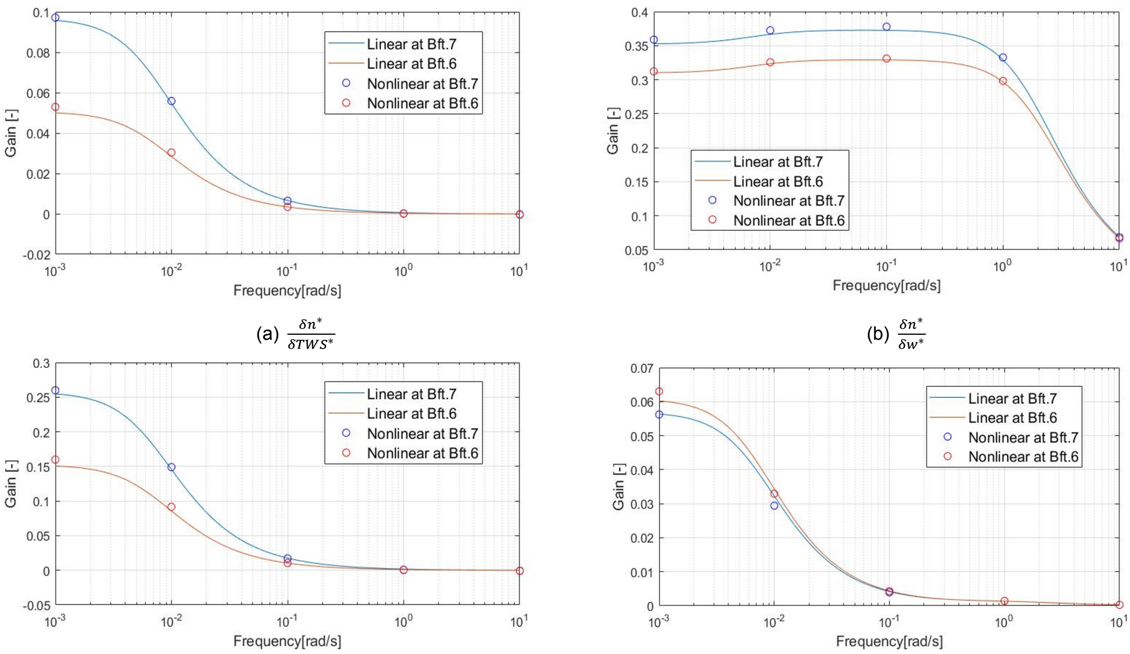

(a) $\frac{\delta n^*}{\delta TWS^*}$ (b) $\frac{\delta n^*}{\delta w^*}$

(c) $\frac{\delta V_S^*}{\delta TWS^*}$ (d) $\frac{\delta V_S^*}{\delta w^*}$

Figure 3.4: Bode magnitude plots of shaft speed and ship speed at Beaufort scale 6 and 7 for the linearised model(solid line) and nonlinear model(dot) of the core propulsion system including wind-assisted propulsion model and actuator.

From Table 3.1 presented in Section 3.2.5, the value of g is negative. Although it does not lie between -1 and -0.5, which is believed to be a typical range for the value of g [Vrijdag and Stapersma, 2017], the slightly negative slope matches the expectation because of increasing piston friction in the engine with increasing engine speed. Regarding the value of v, it lies in the expected between 0.75 to 1.25 [Vrijdag and Stapersma, 2017]. In conclusions, based on Figure 3.4 (a), 3.4 (b), 3.4 (c) and 3.4 (d), it can be seen that the linearised model's responses of engine speed and ship speed to the variation of the true wind speed and wake fit very well with that of the nonlinear model, which indicates that the linearised model for an uncontrolled system with the additional wind-assisted system and actuators can be applied further.

3.5. Controlled system

In this section, the third step, which is the final step for the normalization and linearization of the model, is presented for introducing the controller (engine speed governor). From the previous sections, it can be guaranteed that the derived linearised model, including the wind-assisted model and actuators, is still correct. However, there is still no control system in it, and thus the controller in the normalized and linearised form will be derived.

According to Eq. (2.18), the input of the engine speed governor is the engine speed normalized with the maximum engine speed. This is different from the approach presented in the literature [Vrijdag and Stapersma, 2017] that the engine speed error is normalized with the engine speed at it equilibrium engine speed. Therefore, another new approach is presented here. In this case, the relative error in engine speed is given by:

$$e_n = \frac{n_{set} - n}{n_{max}} \tag{3.51}$$

As derived in Appendix C, the linearised PI controller is derived as:

$$\delta X_{set}^* = \kappa_c \cdot \left(K_i \cdot \delta E_n^* + K_p \cdot (\delta n_{set}^* - \delta n^*)\right) \tag{3.52}$$

where $\kappa_c = \frac{X_{max}}{X_{set,0}} \cdot \frac{n_0}{n_{max}}$ and $\delta E_n^* = \int_0^t \delta e_n^* dt$. To write Eq. (3.52) in State-Space model form, another new differential equation can be derived, which is:

$$\delta E_n^* = \int_0^t \delta e_n^* dt \Rightarrow \frac{\mathrm{d}E_n^*}{\mathrm{d}t} = \delta e_n^* \tag{3.53}$$

In addition, the engine torque M_b is one of the variables that determines the dynamic behavior of the engine and thus it is selected as an new output besides δn^*, δV_s^* and $\delta\theta^*$. The variation of controlled engine torque δM_b^* can be obtained by substituting Eq. (3.52) into Eq. (3.42) and it becomes:

$$\delta M_b^* = (g - v \cdot \kappa_c \cdot K_p) \cdot \delta n^* + v \cdot \kappa_c \cdot K_i \cdot \delta E_n^* + v \cdot \kappa_c \cdot K_p \cdot \delta n_{set}^* \tag{3.54}$$

Eq. (3.54) shows that the variation of the engine torque is, in fact, a linear combination of the system states, δn^* and δE^*, as well as the input δn_{set}^*.

Finally, substituting Eq. (3.52) and Eq. (3.53) into Eq. (3.42) and adding a new state represented by Eq. (3.53) , the Space-State model of the controlled system with actuators and wind-assisted propulsion system can be derived as:

$$A = \begin{bmatrix} \frac{-2+b+g-v\cdot\kappa_c\cdot K_p}{\tau_n} & \frac{-b}{\tau_n} & \frac{-q}{\tau_n} & \frac{v\cdot\kappa_c\cdot K_i}{\tau_n} \\ \frac{\kappa_{prop}\cdot(2-a)}{\tau_v} & \frac{\kappa_{rotor}\cdot\lambda_{Vs}+\kappa_{prop}\cdot a-e}{\tau_v} & \frac{\kappa_{prop}\cdot p}{\tau_v} & 0 \\ 0 & 0 & \frac{-1}{\tau_\theta} & 0 \\ 0 & 0 & 0 & 0 \end{bmatrix} \tag{3.55}$$

$$B = \begin{bmatrix} 0 & \frac{v\cdot\kappa_c\cdot K_p}{\tau_n} \\ 0 & 0 \\ \frac{1}{\tau_\theta} & 0 \\ 0 & 1 \end{bmatrix} \tag{3.56}$$

$$C = \begin{bmatrix} 1 & 0 & 0 & 0 \\ 0 & 1 & 0 & 0 \\ 0 & 0 & 1 & 0 \\ g - v\cdot\kappa_c\cdot K_p & 0 & 0 & v\cdot\kappa_c\cdot K_i \end{bmatrix} \tag{3.57}$$

$$D = \begin{bmatrix} 0 & 0 \\ 0 & 0 \\ 0 & 0 \\ 0 & v \cdot \kappa_c \cdot K_p \end{bmatrix} \tag{3.58}$$

$$x = \begin{bmatrix} \delta n^* \\ \delta V_s^* \\ \delta \theta^* \\ \delta E_n^* \end{bmatrix}, y = \begin{bmatrix} \delta n^* \\ \delta V_s^* \\ \delta \theta^* \\ \delta M_b^* \end{bmatrix}, u = \begin{bmatrix} \delta \theta_{set}^* \\ \delta n_{set}^* \end{bmatrix}, w = \begin{bmatrix} \delta \alpha^* \\ \delta w^* \\ \delta TWS^* \\ \delta TWA^* \end{bmatrix} \tag{3.59}$$

$$G = \begin{bmatrix} 0 & \frac{b}{\tau_n} & 0 & 0 \\ \frac{-1}{\tau_v} & \frac{-\kappa_{prop} \cdot a}{\tau_v} & \frac{\kappa_{rotor} \cdot \lambda_{TWS}}{\tau_v} & \frac{\kappa_{prop} \cdot \lambda_{TWA}}{\tau_v} \\ 0 & 0 & 0 & 0 \\ 0 & 0 & 0 & 0 \end{bmatrix} \tag{3.60}$$

To verify the derived linearised model, the same procedure for obtaining the system's sensitivity function for response of engine speed, engine torque and ship speed to variation of true wind speed and wake at Beaufort scale 6 and 7 will be carried out. The results can be seen in Figure 3.5 and their parameters are given in Table 3.1 presented in Section 3.2.5.

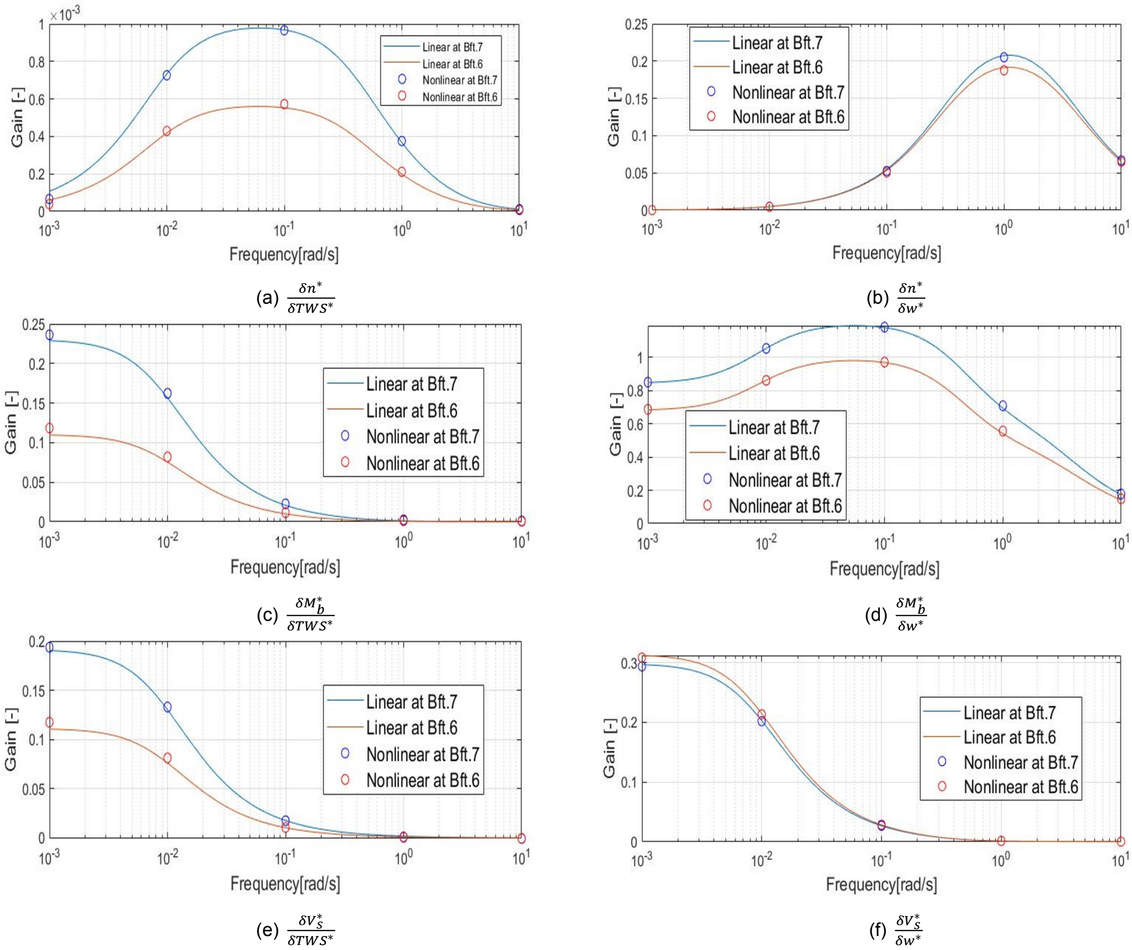

(a) $\frac{\delta n^*}{\delta TWS^*}$ (b) $\frac{\delta n^*}{\delta w^*}$

(c) $\frac{\delta M_b^*}{\delta TWS^*}$ (d) $\frac{\delta M_b^*}{\delta w^*}$

(e) $\frac{\delta V_S^*}{\delta TWS^*}$ (f) $\frac{\delta V_S^*}{\delta w^*}$

Figure 3.5: Bode magnitude plots of shaft speed, engine torque and ship speed at Beaufort scale 6 and 7 for the linearised model (solid line) and nonlinear model (dot) of the core propulsion system including wind-assisted propulsion model, the actuator and a controller.

In conclusion, Figure 3.5 shows that the derived linearized model's responses of engine speed, engine torque, and ship speed to variation of the true wind speed and wake fraction agree very well with that of the nonlinear model. This implies that the derived linearised model for a controlled system with the additional wind-assisted system and actuators can be applied.

3.6. Comparisons

In this section, there are two parts. The difference in frequency-domain behavior of the core State-Space model and the State-Space model with actuators is presented in the first part. In the second part, the controller's impact in the frequency domain can be seen by comparing the behavior of it and that of the system with actuators .

3.6.1. Core propulsion system v.s. Uncontrolled system with actuators

From the previous sections regarding the core propulsion system and uncontrolled system with actuators, their frequency-domain system behavior in terms of engine speed and ship velocity are presented in Figure 3.6.

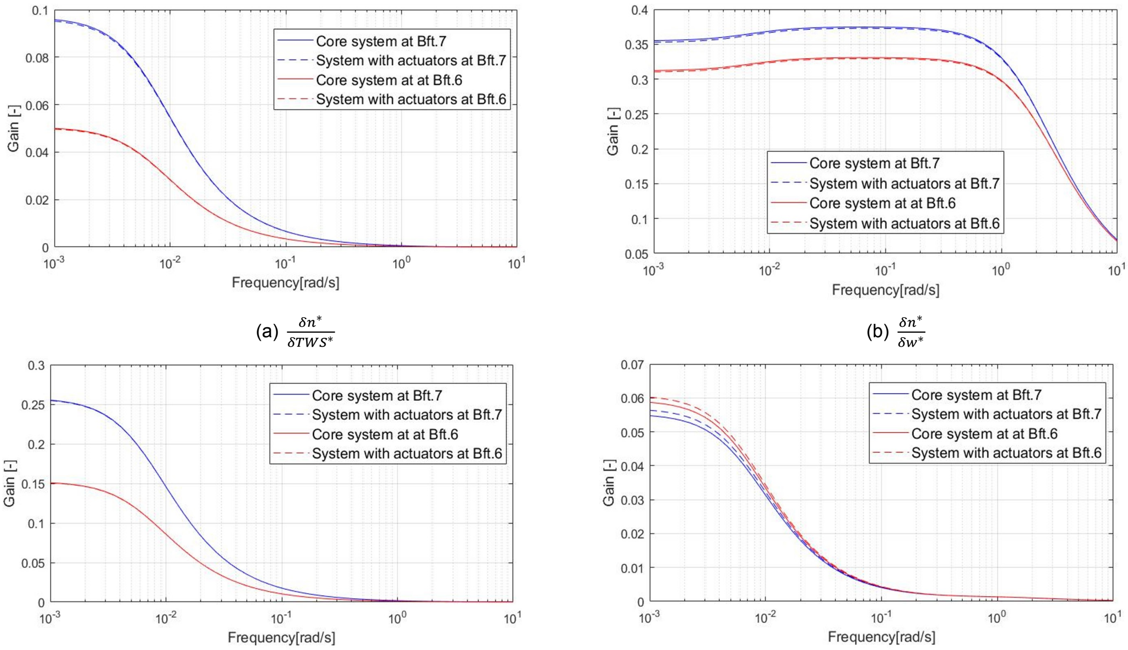

(a) $\frac{\delta n^*}{\delta TWS^*}$ (b) $\frac{\delta n^*}{\delta w^*}$

(c) $\frac{\delta V_S^*}{\delta TWS^*}$ (d) $\frac{\delta V_S^*}{\delta w^*}$

Figure 3.6: Bode magnitude plots of shaft speed and ship speed at Beaufort scale 6 and 7 for the core system (solid line) and uncontrolled system with the actuator (dash line).

Figure 3.6 shows that there is almost the same for these two systems. The slight differences are due to the engine model, which is based on the static fuel map. This phenomenon agrees well with the description in the literature [Vrijdag and Stapersma, 2017].

Besides, two phenomena can be observed. First, in the high-frequency region, the system response in terms of engine speed and ship speed for both core system and uncontrolled one become very low because of the high inertia of the ship and ship mass. Second, as the Beaufort scale increases, the system response in terms of engine speed and ship speed becomes more sensitive to the variation of the true wind speed and wake fraction.

Finally, comparing the impact of the variation of wake fraction on the system, Figure 3.6 (c) shows that the variation of true wind speed influences the variation of ship speed more. This can be explained by the fact that the true wind speed acts directly on the ship speed loop. On the other hand, from Figure

3.6 (b) the engine speed is more sensitive to the wake disturbance because it directly acts on the shaft speed loop. This effect was also mentioned in the study [Stapersma and Vrijdag, 2017].

3.6.2. Uncontrolled system with actuators v.s. Controlled system

To investigate how the controller influences the system response to variation of true wind speed and wake fraction respectively, the controlled system's frequency-domain behavior is compared with that of the uncontrolled system with actuators. The comparison is illustrated in Figure 3.7.

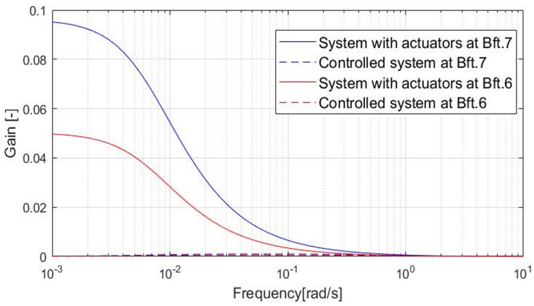

(a) $\frac{\delta n^*}{\delta TWS^*}$

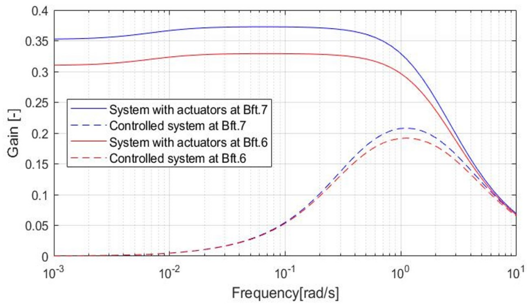

(b) $\frac{\delta n^*}{\delta w^*}$

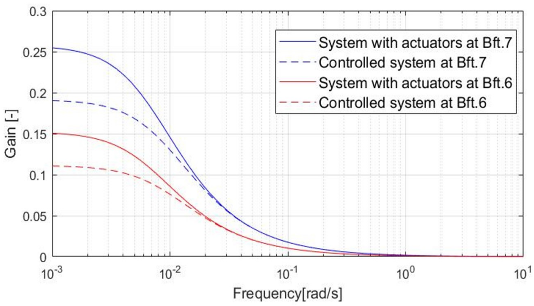

(c) $\frac{\delta V_S^*}{\delta TWS^*}$

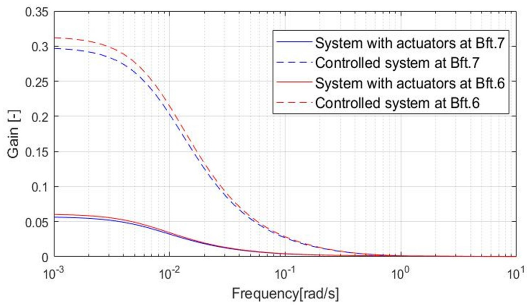

(d) $\frac{\delta V_S^*}{\delta w^*}$

Figure 3.7: Bode magnitude plots of shaft speed and ship speed at Beaufort scale 6 and 7 for the uncontrolled system with the actuator (solid line) and controlled system (dash line).

Regarding the response of engine speed to variation of true wind speed and wake after the controller was introduced, Figure. 3.7 (a) indicates that the response of engine speed to true wind speed variation is reduced significantly, which implies that the impact of wind disturbance around the equilibrium of the engine speed can almost be neglected. On the other hands, as shown in Figure.3.7 (b), the engine speed response becomes less sensitive to wake variation in low-frequency region due to the introduction of the controller governing the engine speed. A similar trend regarding the substantial reduction of engine speed's sensitivity to wake in the low-frequency region can also be noticed in the literature [Vrijdag and Stapersma, 2017].

Concerning the response of ship speed to variations of true wind speed and wake, Figure 3.7 (c) shows that the response of ship speed to true wind speed variation becomes less in low-frequency region. However, the ship speed becomes more sensitive to the wake variation after the controller is introduced. This phenomenon that the ship speed becomes more sensitive to wakefield variation can also be found in the literature [Vrijdag and Stapersma, 2017]. This is results from the propeller torque variation when the engine speed runs in speed control, which subsequently leads to disturbance to the thrust delivered by the propeller. Consequently, the ship speed variation is enlarged by the variation of the propeller thrust instead of engine speed variation in low-frequency region. Moreover, when the engine speed is controlled, torque disturbance due to wakefield induced by waves' amplitude is also mentioned in the literature [Geertsma et al., 2017b].

Besides, from all of the figures in Figure 3.7, two phenomena can be observed. First, it can be seen that the difference between the controlled system and uncontrolled one disappears in the high-frequency region due to the high inertia of the ship total mass and moment of inertia. Second, as the Beaufort scale increases, the system response in terms of engine speed and ship speed becomes more sensitive to the marine environment.

Finally, by comparing dash lines shown in Figure 3.7 (c) and (d) , the variation of true wind speed influences the ship speed more after the controller is introduced . This can be explained by the fact that the true wind speed acts directly on the ship speed loop, whereas the engine speed is more sensitive to the wakefield disturbance because it acts on the shaft speed loop directly. This phenomenon was also mentioned in the study [Stapersma and Vrijdag, 2017].

3.7. Conclusions

Based on the verification results regarding the engine speed, engine torque, and ship speed, more confidence can be guaranteed for the derived linearised model of a wind-assisted ship propulsion system. Besides, the system's response to the regular disturbance of true wind speed and wake at each frequency was analysed in a more systematical way. This provides a foundation for the system's response to the irregular disturbances from the marine environment. Finally, after analyzing the system response to the variation of true wind speed and wake, the derived linearised model can be regarded as a reliable additional tool if the effects of the three types of nonlinear phenomena are identified.

Chapter 4

Disturbances from marine environment

4.1. Introduction

Environmental factors that may impact wind-assisted ship, in general, are wind, waves, and currents. Due to this thesis's scope, only disturbances of true wind speed and wake induced by wave elevation will be focused. To relate the wind-assisted ship propulsion system to the wind and waves it encounters, it is essential first to describe and quantify their physical properties and behaviors.

In nature world, wind and waves vary continuously, and wind and waves that vary perfectly regularly are rarely be seen. Furthermore, the wave's direction is not always in couple with the wind direction. Instead, the wave direction spreads and the wind direction also fluctuates, which are complex and out of the thesis's scope. Hence, to describe them in a simple way, the marine environment can be considered a linear system, which means that the principle of superposition can be applied. With this assumption, the irregular wave amplitude, as an example, can be regarded as the superposition of a certain number of harmonic waves amplitude components with random phase angle. Thus, they can be transferred to the energy density spectrum [Journee and Pinkster, 1997]. This process is illustrated in Figure 4.1 that presents the process from measurement wave elevation in time domain to the energy density spectrum in the frequency domain. On the other hand, when the time signals of wind speed and wave elevation are unavailable from measurements, the spectral approach can be used to generate a time series of wind speed and wave amplitude. This process can also be seen in Figure 4.1 that shows how the the elevation of the sea surface in one direction is generated from the spectrum. Similarly, the time series of true wind speed can be produced in this way [Qian et al., 2016].

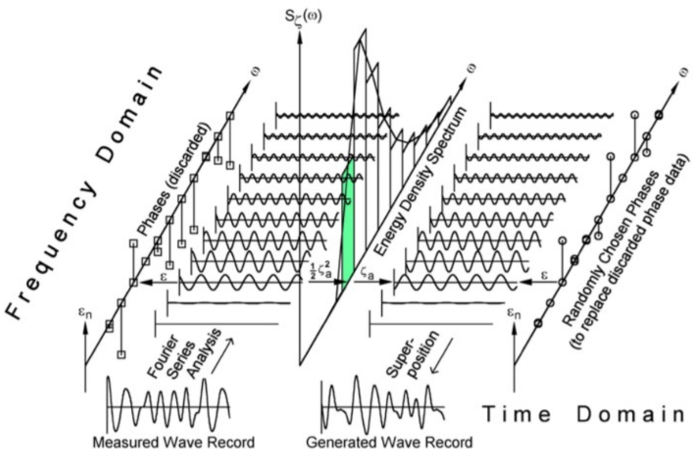

Figure 4.1: Demonstration of time-domain and frequency-domain analysis for waves [Journee and Pinkster, 1997].

To describe wind and waves, the Frøya and Pierson-Moskowitz spectrums are chosen to represent disturbances of true wind speed and wave amplitude respectively in this thesis. The reasons why these two spectrums are selected are given below. First, from Section 3.5, it can be seen that the wind-assisted ship propulsion system is more sensitive to the wind in low-frequency regions. Hence, the usage of Frøya spectrum, which describes the wind speed better in low-frequency region, can be a good start for situations that the responses to the wind disturbance in the low-frequency region is essential. Regarding the Pierson-Moskowitz wave spectrum, it was adopted in the same case from the literature [van der Kolk et al., 2019]. Overall, according to the literature [Veritas, 2010], both of them are recommended for offshore applications and are described in Section 4.2 and 4.3. Furthermore, according to Chapter 3, one of the disturbances to the wind-assisted ship propulsion system is wake fraction instead of wave elevation. Hence, the relation between them will be introduced, and the wake spectrum is derived in Section 4.3.2.

4.2. Wind

The section introduces the Frøya spectrum and how to generate the disturbance of true wind speed.

4.2.1. Wind spectrum

According to the literature [Veritas, 2010], the Frøya spectrum for describing the fluctuations of the horizontal true wind speed is given by:

$$S_{wind} = 320 \cdot \frac{(\frac{TWS_r}{10})^2 \cdot (\frac{z}{10})^{0.45}}{(1+\widetilde{f}^n)^{\frac{5}{3\cdot n}}} \tag{4.1}$$

where

$$\widetilde{f} = 172 \cdot f \cdot (\frac{z}{10})^{\frac{2}{3}} \cdot (\frac{TWS_r}{10})^{-0.75} \tag{4.2}$$

and $n = 0.468$, TWS_r is the reference wind speed [m/s] at 10 [m] height above the sea level and can be obtained by Eq. (2.1) which is based on the Beaufort scale, z is the height above the sea level and it is the height of the wind speed sensor in this case [m] , and f is the frequency [Hz].

This description is regarded to be valid in conditions below [Andersen and Løvseth, 2010]:

- Wind speed, TWS_r, is in the range 10-40 [m/s].
- The height above the sea level,z, is in the range 10-100 [m].
- The frequency, f, is in the range corresponding periods from 1 second to 40 minutes.

It can be noticed that most of the wind spectrum, including the Frøya wind spectrum, the unit of the wind frequency is given as [Hz] instead of [rad/s] for ω used for the linearized model in Chapter 3. Because the value of spectrum based on ω [rad/s] is not equal to that of the spectrum that is given as a function of f [Hz], a spectrum transformation is required. Since the amount of energy in the corresponding frequency intervals, $\Delta\omega$, must be equal to that in the ranges, Δf, the spectrum transformation can be given as [Journee and Pinkster, 1997]:

$$S_{wind}(f) \cdot df = S_{wind}(\omega) \cdot d\omega \rightarrow S_{wind} = \frac{S_{wind}(f)}{\frac{d\omega}{df}} \tag{4.3}$$

The relation between f [Hz] and ω [rad/s] is:

$$\omega = 2 \cdot \pi \cdot f \rightarrow \frac{d\omega}{df} = 2\pi \tag{4.4}$$

Therefore, by applying Eq. (4.3) and (4.4), the wind spectrum based on the frequency, ω, from Beaufort scale 4 to 7 can be calculated and are shown in Figure 4.2.

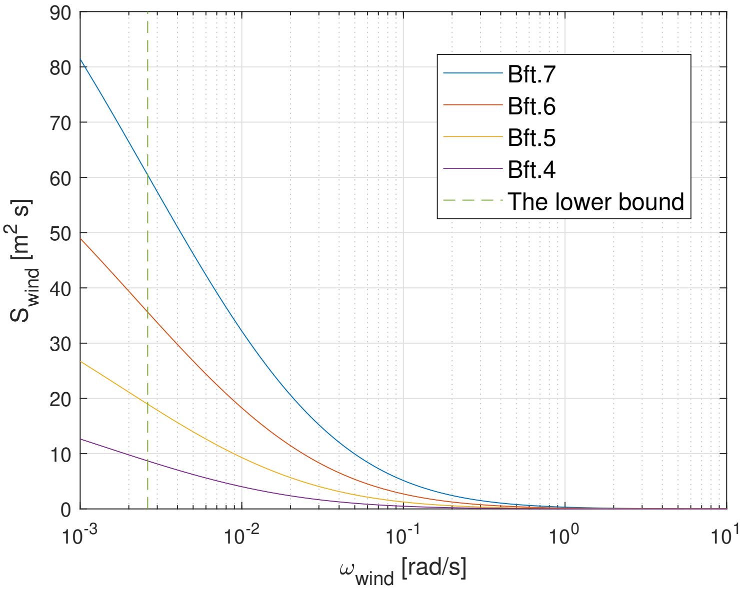

Figure 4.2: Frøya wind spectrum at Beaufort 4 to 7. Note that the green dashed line represents the frequency corresponding to 40 minutes, which is regarded as a lower bound of the frequency according to [Andersen and Løvseth, 2010].

Figure 4.2 shows that a significant increase of spectral energy density, $S_{wind}(\omega)$, with decreasing wind frequency. Furthermore, as the Beaufort scale increases, which means a higher reference of true wind speed, TWS_r, is adopted, the wind spectral energy density, $S(\omega)$, increases markedly.

4.2.2. Link the wind disturbance to the wind-assisted ship propulsion system

In this thesis, the disturbance of the true wind speed can be related to the wind-assisted ship propulsion system in two ways. The first approach links the variation of the true wind speed over a period to the system. In fact, in Chapter 3, several regular disturbance of true wind speed with different frequency were already implemented. In this section, the irregular disturbance of true wind speed was generated, which was used in Chapter 5 for time-domain analysis. The second approach links the wind spectrum to the transfer functions of the wind-assisted system from a frequency-domain view. Because variables were normalized in Chapter 3, the wind spectrum was also normalized.

Link the wind disturbance to the nonlinear model

Chapter 3 shows that the regular disturbance of true wind speed was already evaluated when comparing the dynamic behavior of the linearised model with that of the nonlinear model. However, in reality, a regular disturbance is hardly to seem. Therefore, according to the research [Gavriluta et al., 2012] [Qian et al., 2016] that mentioned how to generate a irregular disturbance of true wind speed from a wind spectrum, the time series of true wind speed can be obtained by :

$$TWS(t) = TWS_0 + \sum_{n=1}^{N} TWS_n \cdot sin(\omega_n + \epsilon_n) \tag{4.5}$$

where N is the number of intervals which can be obtained by separating the band of the wind frequency into several constant unit $(d\omega_{wind})$, ω_n is the vector of wind frequency that corresponds to each frequency in the axis of the wind spectrum, ϵ_n is the vector of phase angles which lies from 0 to 2π [rad] and be randomly generated, and TWS_n is the vector of the true wind speed at each corresponding frequency and it can be calculated by:

$$S_{wind}(\omega_{wind_n}) \cdot d\omega_{wind} = \frac{1}{2} \cdot TWS_n^2 \Rightarrow TWS_n = \sqrt{2 \cdot S_{wind}(\omega_{wind_n}) \cdot d\omega_{wind}} \tag{4.6}$$

By applying Eq. (4.5) and (4.6), time series of true wind speed at Beaufort scale 4 to 7 can be obtained from the Frøya wind spectrum at each corresponding Beaufort scale and they are shown in Figure 4.3.

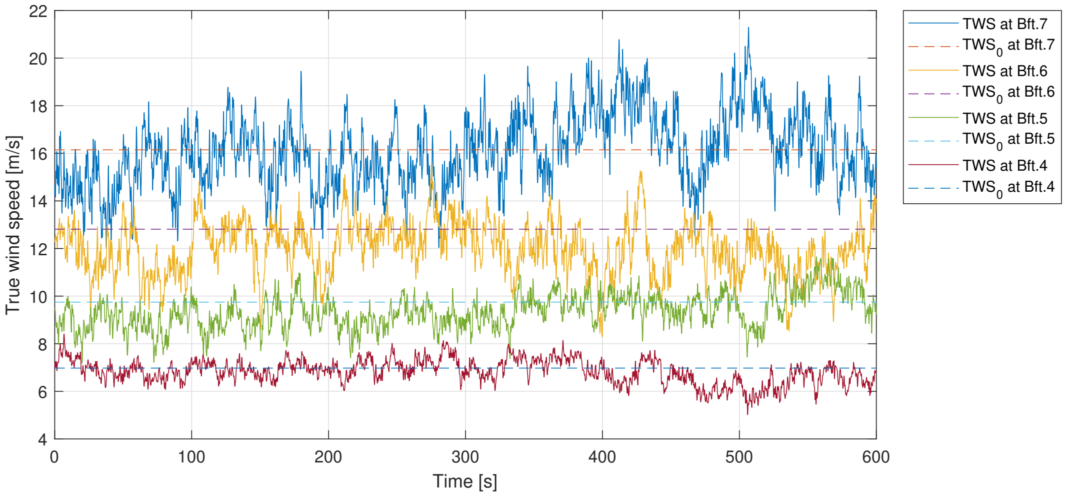

Figure 4.3: Time-varying true wind speed at Beaufort scale 4 to 7.

Link the wind disturbance to the linearised model

From Chapter 3, it can be noticed that the frequency-domain analysis for the linearised model was conducted in normalization form. Considering this and the application of the wind spectrum in Chapter 5, it is decided to also normalize the Frøya wind spectrum at Beaufort scale 4 to 7, and they can be obtained by applying Eq. (4.7). Consequently, the Frøya wind spectrum in normalized form, $S_{\delta wind^*}$, is presented in Figure 4.4.

$$S_{\delta TWS^*}(\omega_{wind}) = \frac{S_{wind}(\omega_{wind})}{TWS_0^2} \tag{4.7}$$

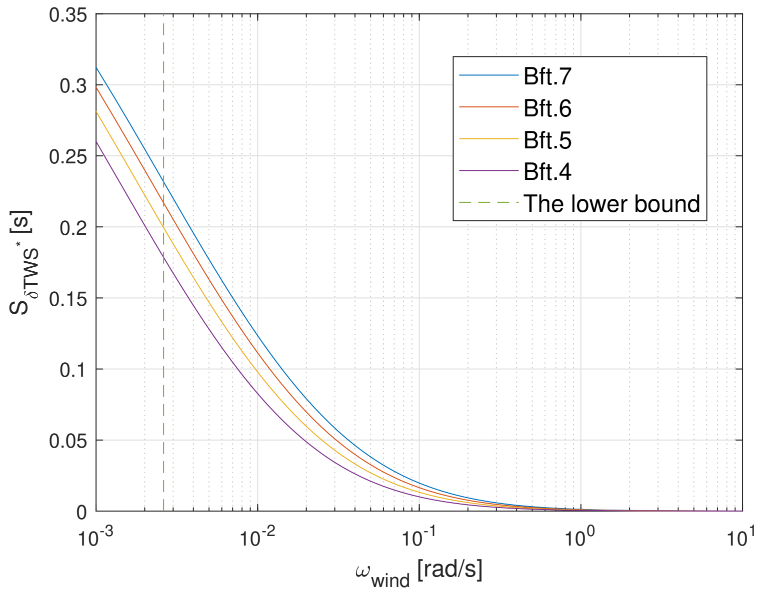

Figure 4.4: Frøya wind spectrum in normalised form. Note that the green dashed line represents the frequency corresponding to 40 minutes, which is regarded as a lower bound of the frequency based on [Andersen and Løvseth, 2010].

4.3. Wave

This section introduces the Pierson-Moskowitz wave spectrum used to model the disturbance of wave amplitude at different Beaufort scale. However, in Chapter 3, it can be noticed that the wave amplitude does not influence the wind-assisted ship propulsion system directly; instead, it affect it via the wakefield sensed by the propeller. Moreover, considering one of the disturbances into the system is wake fraction, it is decided to derive the wake spectrum, which was derived from the wave encounter spectrum. Subsequently, from a frequency-domain perspective, the derived wake spectrum was connected to the wind-assisted propulsion ship system in Chapter 5.

4.3.1. Wave spectrum

An irregular wave elevation can be seen in the real sea surface. The sea elevation gradually becomes statistically stable after the wind has blown for a specified period. Furthermore, if the direction of the waves is the same as that of the dominant wind, which means that multi uni-direction waves are paralleled with each other, the sea in this condition is regarded as a long-crested sea which is fully-developed. To describe the fully-developed long-crested sea in a precise way, one-parameter Pierson-Moskowits (PM) spectrum, which can be scaled based on the Beaufort scale with the significant wave height, can be used [Pérez and Blanke, 2002] and it is:

$$S_{wave}(\omega_{wave}) = \frac{0.78}{\omega_{wave}^5} \cdot e^{\frac{-3.11}{\omega_{wave}^4 \cdot H_{1/3}^2}} \tag{4.8}$$

where ω_{wave} is absolute wave frequency in units of [rad/s], which is observed by the fixed coordinate system, $H_{1/3}$ [m] is the significant wave height that can be observed from the sea which provided in Table 4.1.

Wave Spectrum Parameters Estimates								
Scale of Beaufort	Wind Speed at 19.5 m above sea	Open Ocean Areas (Bretschneider)			North Sea Areas (JONSWAP)			
	(kn)	$H_{1/3}$ (m)	T_1 (s)	T_2 (s)	$H_{1/3}$ (m)	T_1 (s)	T_2 (s)	γ (-)
1	2.0	1.10	5.80	5.35	0.50	3.50	3.25	3.3
2	5.0	1.20	5.90	5.45	0.65	3.80	3.55	3.3
3	8.5	1.40	6.00	5.55	0.80	4.20	3.90	3.3
4	13.5	1.70	6.10	5.60	1.10	4.60	4.30	3.3
5	19.0	2.15	6.50	6.00	1.65	5.10	4.75	3.3
6	24.5	2.90	7.20	6.65	2.50	5.70	5.30	3.3
7	30.5	3.75	7.80	7.20	3.60	6.70	6.25	3.3
8	37.0	4.90	8.40	7.75	4.85	7.90	7.35	3.3
9	44.0	6.10	9.00	8.30	6.10	8.80	8.20	3.3
10	51.5	7.45	9.60	8.80	7.45	9.50	8.85	3.3
11	59.5	8.70	10.10	9.30	8.70	10.00	9.30	3.3
12	>64.0	10.25	10.50	9.65	10.25	10.50	9.80	3.3

Table 4.1: Parameters for wave spectrum based on Beaufort scale [Journee and Pinkster, 1997].

Based on Table 4.1, the significant wave height at each Beaufort scale is provided, so the wave spectrum at each Beaufort scale can be obtained and is shown in Figure 4.5.

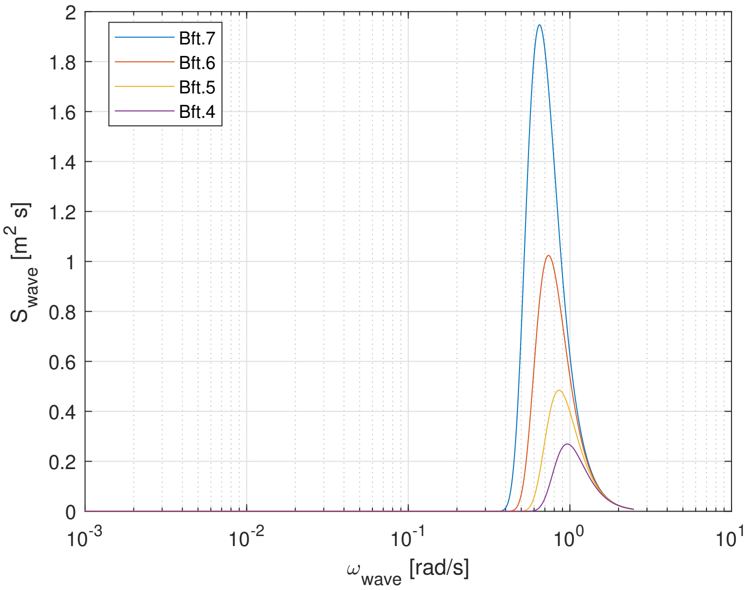

Figure 4.5: Pierson-Moskowits (PM) spectrum at Beaufort scale 4 to 7.

Figure 4.5 shows that as the Beaufort scale decreases, the peak value of the wave spectrum gradually shifts toward a higher frequency region. Furthermore, less energy is contained in the wave spectrum when the Beaufort scale becomes lower.

4.3.2. Wake spectrum

This section shows how the wake spectrum was derived and be normalized with its static value for the frequency-domain analysis. After the wave encounter spectrum is obtained, the wake spectrum based on it can be derived because the sea surface elevation affects the dynamic behavior of the wind-assisted propulsion system via the wake disturbance. Furthermore, to conduct the time-domain analysis for the wind-assisted ship propulsion system, the irregular disturbance of wake was also derived subsequently.

Ship speed and its heading relative to waves

To derive the wake spectrum, the relative motion of the ship to waves must be considered first. When sailing in waves, a ship will encounter waves with a different frequency because of its speed and direction relative to waves. The frequency sensed by the ship is called the wave encounter frequency, $\omega_{wave,\ e}$ [rad/s]. Considering this relative motion between the ship and waves, a spectrum transformation is required because the value of a wave spectrum based on the frequency of encounter, $\omega_{wave,e}$, is different from the wave spectrum based on the absolute wave frequency, ω_{wave}. Following the same principle: there must be an equal amount of energy in the frequency bands $d\omega_{wave,e}$ and $d\omega_{wave}$, the spectrum transformation can be carried out by [Journee and Pinkster, 1997]:

$$S_{wave,e}(\omega_{wave,e}) \cdot d\omega_{wave,e} = S_{wave}(\omega_{wave}) \cdot d\omega_{wave} \rightarrow S_{wave,e}(\omega_{wave,e}) = \frac{S_{wave}(\omega_{wave})}{\frac{d\omega_{wave,e}}{d\omega_{wave}}} \tag{4.9}$$

Regarding the wave encounter frequency, $\omega_{wave,e}$, it can be obtaiend as [Journee and Pinkster, 1997]:

$$\omega_{wave,e} = \omega_{wave} - \frac{\omega_{wave}^2}{g} \cdot V_s \cdot cos(\mu) \tag{4.10}$$

where ω_{wave} is the absolute wave frequency measured in fixed reference [rad/s], V_s is the ship forward speed in surge direction and μ is the ship's heading relative to wave direction where $\mu = 0$ [degree] represents following waves and $\mu = 180$ [degree] corresponds to head waves.

Therefore, based on Eq. (4.9) and (4.10) , the wave encounter spectrum observed by the ship can be calculated as:

$$S_{wave,e}(\omega_{wave,e},\mu) = \frac{S_{wave}(\omega_{wave})}{\left|1 - \frac{2\cdot\omega_{wave}\cdot V_S\cdot cos(\mu)}{g}\right|} \tag{4.11}$$

To get a feeling about the relation between the wave encounter frequency ($\omega_{wave,e}$) and the absolute wave frequency (ω_{wave}), Eq. (4.10) was applied for the ship sailing at 10 [knot] when μ is $0°$, $60°$,$90°$ and $180°$. Consequently, four results based on this four conditions are illustrated in Figure 4.6.

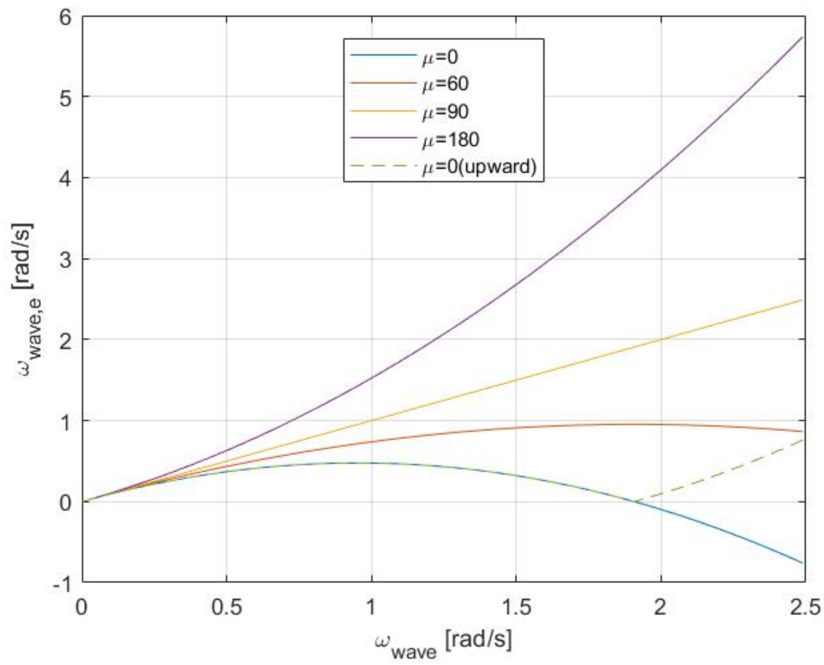

Figure 4.6: The relations between wave encounter frequency ($\omega_{wave,e}$) and absolute wave frequency (ω_{wave}) when the ship sails at 10 [knots] with different heading angle relative to waves (μ).

When looking at Figure 4.6, wave encounter frequency for the following seas, such as $\mu = 180$ [degree], becomes negative, which does not exist in reality. Therefore, according to the research [Nielsen, 2017], the negative encounter frequency was turned upwards so that it becomes positive and shown in Figure 4.6 with a green dashed line. Furthermore, when sailing in head seas, the absolute wave frequency is 1-to-1 mapping with the corresponding encounter wave frequency. Hence, there are no challenges in transforming the wave spectrum to the wave encounter spectrum. Nevertheless, in the following seas, it can be seen that three different absolute wave frequency leads to the same wave encounter frequency, which implies that the wave encounter frequency is not uniquely related to the absolute wave frequency in some conditions. Therefore, those conditions are required to be identified for the following seas.

For the curves in the following seas, such as stern waves (μ=180 [degree]) shown in Figure 4.6, it can be observed that there are three conditions. First, when the wave encounter frequency lies between zero and it's maximum value, three different absolute wave frequency results in the same wave encounter frequency. Second, if the wave encounter frequency reaches its maximum value, two different absolute wave frequency leads to the same wave encounter frequency. Finally, for the wave encounter frequency higher than it's maximum value, there is a unique relation between it and absolute wave frequency. Therefore, the maximum wave encounter frequency can be used to define each condition, and it's corresponding absolute wave frequency can be obtained by:

$$\frac{\mathrm{d}\omega_{wave,e}(\omega_{wave})}{\mathrm{d}\omega_{wave}} = 0 \tag{4.12}$$

Based on Eq. (4.12), the maximum encounter wave frequency is:

$$\omega_{wave,e_{max}} = \frac{g}{4 \cdot V_s \cdot cos(\mu)} \tag{4.13}$$

Finally, the wave spectrum based on wave encounter frequency can be derived after the relation between it and absolute wave frequency is clear. Considering the special circumstances for following seas, [Lewandowski, 2004] provides a way to derive the wave encounter spectrum, which is:

$$S_{wave,e}(\omega_{wave,e}) = \sum_{j=1}^{N} S_{wave}(\omega_{wave,j}) \tag{4.14}$$

where $\omega_{wave,j}$ is the absolute wave frequency corresponding to the wave encounter frequency , N is the number of the absolute wave frequency that results in the same wave encounter frequency, and the value of N depends on the conditions which mentioned previously.

The physical meaning of Eq. (4.14) is that the wave encounter spectrum density at each absolute wave frequency resulting in the same encounter frequency are summed together. According to another research [Nielsen, 2017], this procedure can also be illustrated in Figure 4.7.

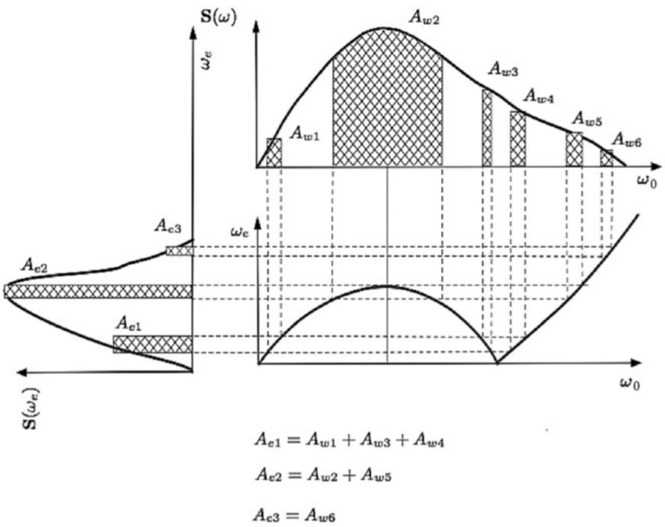

Figure 4.7: The relations between a wave encounter spectrum between a wave spectrum [Nielsen, 2017].

To build a wave encounter spectrum, the absolute wave frequency corresponding to each encounter wave frequency is needed, and the value of those absolute wave frequency at a given wave encounter frequency can be obtained analytically from Eq. (4.10) as:

$$\omega_{wave,1} = \frac{-b' + \sqrt{b'^2 - 4 \cdot a' \cdot c'}}{2 \cdot a'}, \quad \omega_{wave,2} = \frac{-b' - \sqrt{b'^2 - 4 \cdot a' \cdot c'}}{2 \cdot a'} \tag{4.15}$$

where $a' = \frac{-Vs \cdot cos(\mu)}{g}$, $b' = 1$ and $c' = -\omega_{wave,e}$

For the negative wave encounter frequency, which is seen positive by observers, the corresponding positive absolute wave frequency can be obtained as:

$$\omega_{wave,3} = \frac{-b'' + \sqrt{b''^2 - 4 \cdot a'' \cdot c''}}{2 \cdot a''} \tag{4.16}$$

where $a'' = \frac{-Vs \cdot cos(\mu)}{g}$, $b'' = 1$ and $c'' = \omega_{wave,e}$

Subsequently, considering that the different number of absolute wave frequency leads to the same wave encounter frequency, three conditions are made here (Note that to simplify expression shown below, $S_{wave'}$ means S_{wave} is divided by $\left|1 - \frac{2 \cdot \omega_{wave} \cdot V_S \cdot cos(\mu)}{g}\right|$.)

- Condition I: three different absolute wave frequency results in the same wave encounter frequency. This happens when $\omega_{wave,e} < \omega_{wave,e_{max}}$. Under this situation, $N = 3$ and the wave encounter spectrum density at a certain wave encounter frequency is:

$$S_{wave.e}(\omega_{wave,e}) = S_{wave'}(\omega_{wave,1}) + S_{wave'}(\omega_{wave,2}) + S_{wave'}(\omega_{wave,3}) \tag{4.17}$$

- Condition II: two different absolute wave frequency result in the same wave encounter frequency. This occurs when $\omega_{wave,e} = \omega_{wave,e_{max}}$ and $\omega_{wave,e} = 0$. Under the condition, $N = 2$ and the encounter wave spectrum density at this wave encounter frequency is:

$$S_{wave,e}(\omega_{wave,e}) = S_{wave'}(\omega_{wave,1}) + S_{wave'}(\omega_{wave,3}) \tag{4.18}$$

- Condition III: There is an unique relation between the absolute wave frequency and the wave encounter frequency. This can be found when $\omega_{wave,e} > \omega_{wave,e_{max}}$. Under this circumstances, $N = 1$ and the encounter wave spectrum density at this wave encounter frequency is:

$$S_{wave,e}(\omega_{wave,e}) = S_{wave'}(\omega_{wave,3}) \tag{4.19}$$

Finally, under the condition that the ship sails at 10 [knot], the wave encounter spectrum of μ=0,60,90, and 180 [degree] is illustrated in Figure 4.8. At this point, it has to mention that the area under each line should be the same due to energy conservation. By applying the trapezoidal numerical integration method, the area for μ =0,60,120 and 180 [degree] are 0.8794, 0.8812, 0.8813 and 0.8805 respectively. Although there is a small difference due to the numerical method, especially for the stern-wave spectrum that contains a singular point, their area is almost the same. This means that the energy is conveyed well during the transformation of wave spectrum.

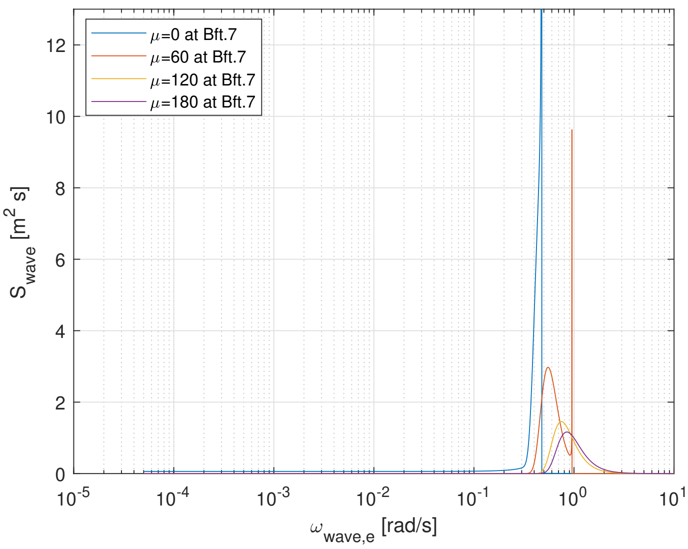

Figure 4.8: Wave encounter spectrum based on the wave encounter frequency for the ship speed of 10 [knot] at different ship headings with respect to the waves,μ [degree].

From Figure 4.8, when sailing in the following seas, the energy distribution shifts to the low-frequency region. Furthermore, when $\mu = 0$ and $\mu = 60$ [degree], two peaks can be seen in the following seas. This is explained by the fact that the wave encounter spectrum becomes singular at a specific absolute wave frequency, which turns the denominator in Eq. (4.11) into zero. Despite the mathematical issue, it is believed that the amplitude of waves will not become infinite due to the extremely small frequency band. Besides, in the following seas, it can be seen that the density of the wave encounter spectrum becomes zero after it's a singular point. This is results from multiple absolute wave frequency leading to the same encounter wave frequency.

Propeller wake

After the wave spectrum sensed by the ship is adequately obtained, the apparent waves can be connected to the wind-assisted ship propulsion system. But how the propulsion system, especially the diesel engine, is influenced by waves? From Chapter 2 and 3, the disturbances from the marine environment are true wind speed and wakefield respectively. Regarding the wake disturbance, how to link wave amplitude and wakefield sensed by the propeller? According to [Vrijdag and Schuttevaer, 2019] and [Geertsma et al., 2017b], the fluctuation of the wake entering the propeller is the main reason for the engine loading disturbance if a engine speed governor is used. One of the reasons for the wake fluctuation is the orbital motion of the water particle flowing into the propeller, which results in a disturbance on the average speed flowing into the propeller. The motion of water particle is related to the wave elevation and gradually decreases in deeper water [Journee and Pinkster, 1997]. Considering the impact of the unsteady wakefield induced by wave amplitude, additional wake fraction, which represents the disturbance is required to be added to the advance velocity, V_a, experienced by a propeller. However, before finding the relation between the wakefield and the wave amplitude, some crucial assumptions used in [Vrijdag and Schuttevaer, 2019] are made below to simplify the wake disturbance:

- Only the axial component of velocity is modeled. In other words, the influence of other contributing factors, such as radiated waves, diffracted waves, are not considered.
- The advance velocity over the whole propeller disk equals the that at the center of the propeller hub. This means that the velocity distribution in the radial direction over the propeller is not considered.
- The ship's speed and it's heading angle relative to waves are considered as constant despite the unsteady wake disturbance.

With those assumptions, an additional axial velocity induced by wave amplitude, u_x [m/s], that represents a velocity disturbance, is added to the propeller advance speed, V_a [m/s], as:

$$V_a = V_s \cdot (1 - w) - u_x \tag{4.20}$$

According to the classic linear wave theory adopted in the literature [Geertsma et al., 2017b], the axial velocity of water particles induced by wave amplitude below the sea surface can be expressed as:

$$u_x = \omega_{wave} \cdot e^{k \cdot z} \cdot \zeta_a \cdot sin(\omega_{wave,e} \cdot t) \tag{4.21}$$

$$k = \frac{\omega^2}{g} \tag{4.22}$$

where ζ is the wave amplitude[m], ω_{wave} is the absolute wave frequency [rad/s], k is the wave number in the unit of [1/m], z is the depth below the sea surface and $\omega_{wave,e}$ is wave encounter frequency [rad/s].

Due to the second assumption: the advance velocity over the whole propeller disk equals the that at the center of the propeller hub, the exponential term in Eq. (4.21) is simplified as:

$$e^{k \cdot z} = e^{k \cdot z_0} \tag{4.23}$$

where z_0 represents the depth of the propeller hub below the sea surface and it is -4.25 [m] in this case.

Furthermore, the study [Vrijdag and Schuttevaer, 2019] shows that the water particle sensed by a propeller has a direction due to the ship heading relative to waves. Therefore, a operator , $cos(\mu)$, is introduced and Eq. (4.21) and yields:

$$u_x = cos(\mu) \cdot \omega_{wave} \cdot e^{k \cdot z_0} \cdot \zeta_a \cdot sin(\omega_{wave,e} \cdot t) \tag{4.24}$$

Substituting Eq. (4.24) into Eq. (4.20) gives:

$$w(t) = w_0 + \frac{cos(\mu) \cdot \omega_{wave} \cdot e^{k \cdot z_0} \cdot \zeta_a \cdot sin(\omega_{wave,e} \cdot t)}{V_s} \tag{4.25}$$

where w_0 is the wake fraction on calm water.

Note that w represent wake fraction [-] and is frequency [rad/s] in the thesis.By defining $w(t) = \delta w$ and $\delta\zeta_a = \zeta_a \cdot sin(\omega_e \cdot t)$, the wake disturbance can be rewritten as:

$$\delta w = \frac{cos(\mu) \cdot \omega_{wave} \cdot e^{k \cdot z}}{V_s} \cdot \delta\zeta_a \tag{4.26}$$

After the wave spectrum based on the wave encounter frequency as well as the relationship between the variation of wake fraction, and sea surface elevation, $\delta\zeta_a$ are obtained respectively, a wake spectrum based on the wave encounter frequency can be derived and was used to analyze the response of the wind-assisted ship propulsion system in Chapter 5. Based on Eq. (4.26), a transfer function for obtaining the wake disturbance from wave elevation can be represented as:

$$H = \frac{cos(\mu) \cdot \omega_{wave} \cdot e^{k \cdot z_0}}{V_s} \tag{4.27}$$

Therefore, by applying the transfer function H, the wake spectrum based on the encounter wave frequency can be approximated as:

$$S_{\delta w}(\omega_{wave,e}) = H(\omega_{wave})^2 \cdot S_{wave,e}(\omega_{wave,e}) \tag{4.28}$$

However, considering that the wave encounter frequency can be generated from different absolute wave frequency in the following seas, a similar approach used to define conditions in the wave encounter spectrum in the following seas is applied here:

- Condition I: three different absolute wave frequency result in the same wave encounter frequency. This phenomenon happens when $\omega_{wave,e} < \omega_{wave,e_{max}}$. Under this situation, the wake spectrum is:

$$S_{\delta w}(\omega_{wave,e}) = \sum_{j=1}^{3} H(\omega_{wave,j})^2 \cdot S_{wave'}(\omega_{wave,j}) \tag{4.29}$$

- Condition II: two different absolute wave frequency lead to the same wave encounter frequency. This occurs when $\omega_{wave,e} = \omega_{wave,e_{max}}$ or $\omega_{wave,e} = 0$ [degree]. Hence, the wake spectra density under this condition is:

$$S_{\delta w}(\omega_{wave,e}) = \sum_{j=1}^{2} H(\omega_{wave,j})^2 \cdot S_{wave'}(\omega_{wave,j+1}) \tag{4.30}$$

- Condition III: There is an unique relationship between the absolute wave frequency and the wave encounter frequency. Therefore, the wake spectra density under this situation is:

$$S_{\delta w}(\omega_{wave,e}) = H(\omega_{wave,3})^2 \cdot S_{wave'}(\omega_{wave,3}) \tag{4.31}$$

To understand the impact of the ship heading relative to waves on the wake spectrum, the ship sailing at 10 [knot] at Beaufort scale 7 was used to evaluate Eq. (4.29), (4.30) and (4.31) from head to stern waves. And the results are shown in Figure 4.9. Note that only the area for μ =180 [degree] and μ =0 [degree] should be the same because all of the energy is conveyed into surge direction under these two conditions. By applying the trapezoidal numerical approach, the area for these two angles are 0.0108 and 0.0109 respectively. Despite a little difference due to numerical error, their area is approximately the same.

Furthermore, under the chosen condition, $V_s = 10$ [knot], the impact of Beaufort scale on wake spectrum for $\mu = 60$ [degree] is also investigated and presented in Figure 4.10, which shows how the transfer function, H, influences the wake spectrum. From Figure 4.9, compared with the wave encounter spectrum shown in Figure 4.8, the wake spectrum was enlarged by the operator, $cos(\mu)$, presented in Eq. (4.27) when μ is gradually close to 0 and 180 [degree]. Moreover, when $\mu = 90$ [degree], it can be observed that the energy of wake spectrum is zero. This can be explained by the fact that the wake disturbance in surge direction is zero for beam waves.

Figure 4.10 shows that the location of the peak value in the wake spectrum gradually shift to high-frequency region while the Beaufort scale decreases. In addition, all the value of the wake spectrum at different Beaufort scales become zero after their singular point, which is 0.95 [rad/s] for $\mu = 60$ [degree] and $V_s = 10$ [knot]. Finally, from Figure 4.10, the energy containing in the wake spectrum and it's corresponding frequency band decrease when the Beaufort scale decreases.

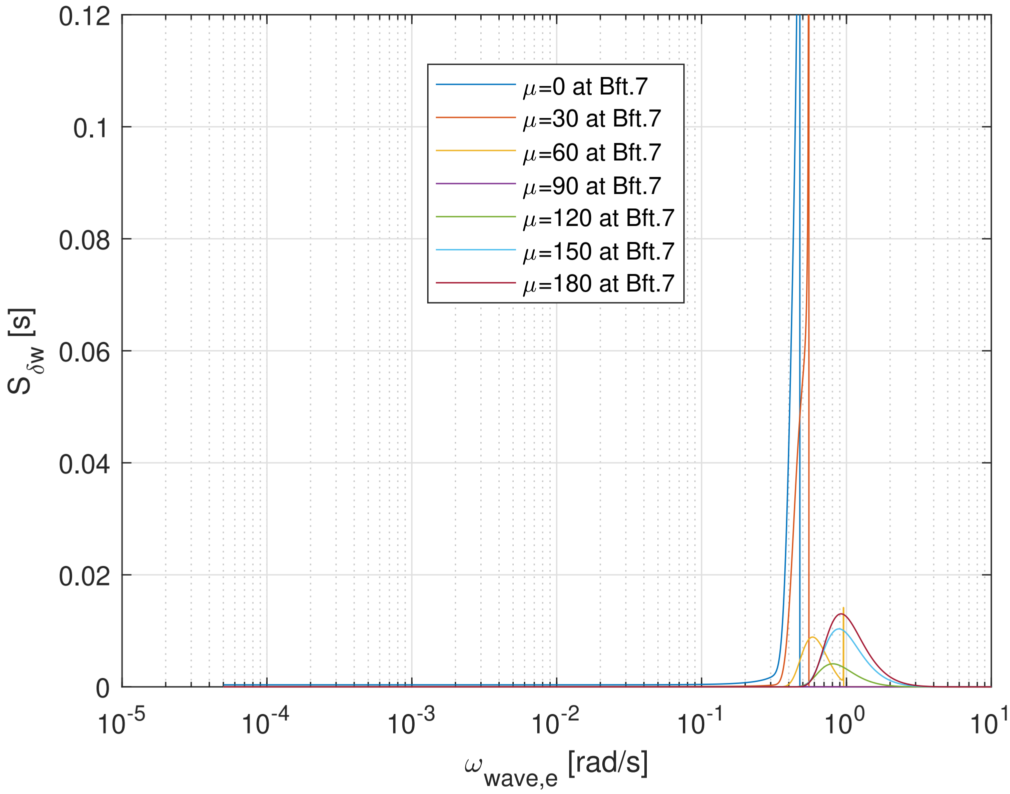

Figure 4.9: Wake spectrum based on wave encounter frequency at Beaufort scale 7 for the ship sailing at 10 [knot] from stern waves (μ=0 [degree]) to head waves (μ=180 [degree]).

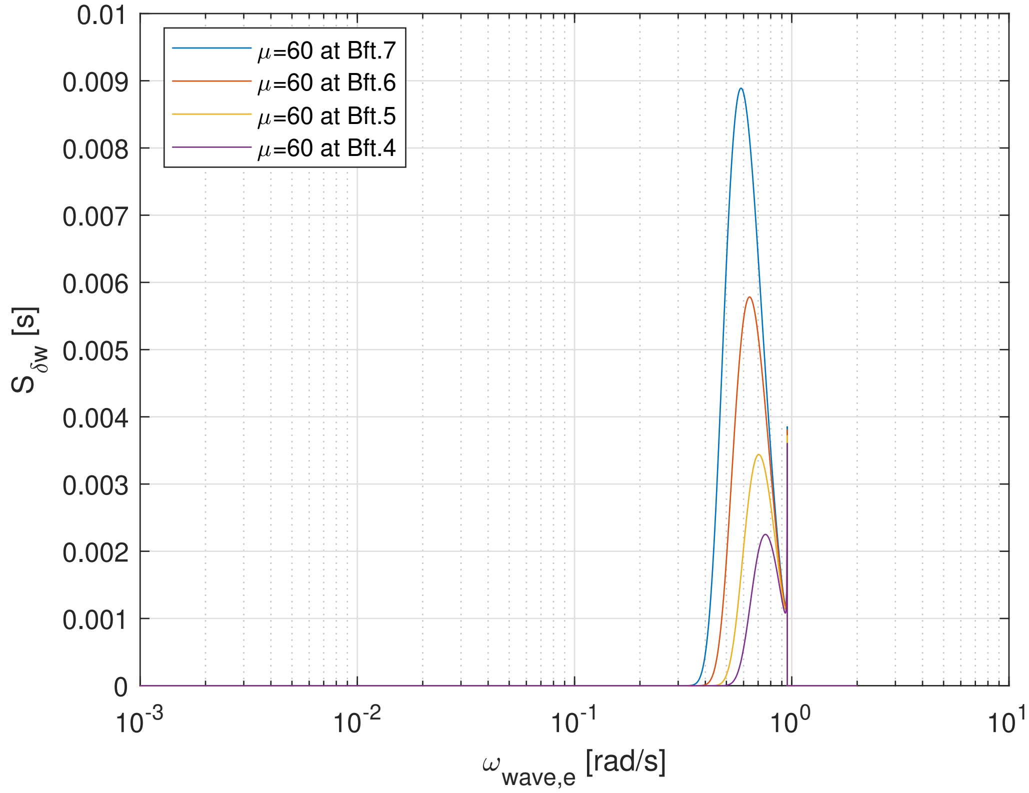

Figure 4.10: Wake spectrum based on encounter wave frequency for the ship sailing at 10 [knot] at $\mu = 60$ [degree] from Beaufort scale 4 to 7

4.3.3. Link the wake disturbance to the wind-assisted ship propulsion system

In this thesis, the wake disturbance can be related to the wind-assisted ship propulsion system in two ways. The first approach is linking the time series of unsteady wake fraction to the system from a time-domain perspective. In Chapter 3, the regular disturbance of wake was already implemented. In this section, the irregular disturbance of wake is generated, which can be used in Chapter 5. Besides, the second approach links the derived wake spectrum to the transfer functions of the wind-assisted system from a frequency-domain view. Because variables were normalized in Chapter 3, the wake spectrum is normalized as well.

Link the wake disturbance to the nonlinear model

In Chapter 3, the regular disturbance of wake with different frequency was already evaluated when comparing the dynamic behavior of the linearised model with that of the nonlinear model. However, in reality, a regular disturbance seldom occurs. Therefore, according to the research [Pérez and Blanke, 2002] that mentioned how to generate irregular wave amplitude from a wave spectrum, the irregular wake can be obtained similarly from the derived wake spectrum as:

$$w(t) = \sum_{n=1}^{N} w_n \cdot sin(\omega_{wave,e_n} + \epsilon_n) \tag{4.32}$$

where N is the number of intervals which can be obtained by separating the band of the wave encounter frequency into several constant unit, ω_{wave,e_n} is the vector of wave encounter frequency that corresponds to each encounter frequency in the horizontal axis of the wake spectrum, ϵ_n is the vector of phase angles which lies from 0 to 2π [rad] and be randomly generated, and w_n is the vector of the magnitude of wake fraction and it can be calculated as:

$$S_{\delta w}(\omega_{wave,e_n}) \cdot d\omega_{wave,e} = \frac{1}{2} \cdot w_n^2 \Rightarrow w_n = \sqrt{2 \cdot S_{\delta w}(\omega_{wave,e_n}) \cdot d\omega_{wave,e}} \tag{4.33}$$

By using Eq. (4.32) and (4.33) for the ship sailing at 10 [knot], three time-domain simulations of wake disturbance at Beaufort scale 7 with different μ are shown in Figure 4.11. Besides, to see the time series of wake disturbance at different Beaufort scales, the irregular disturbance of wake at $\mu = 60[degree]$ are illustrated in Figure 4.12. Note that those irregular disturbance of wake are only examples because different phase angles were generated randomly, which means that different time series of wake disturbance was produced in each simulation for generating the irregular disturbance. However, some phenomena can still be noticed. In Figure 4.11, it can be seen clearly that the wave encounter frequency gradually becomes higher from stern to head waves. This can be mathematically explained by Figure 4.9 that the wake spectrum in stern waves lies in the low-frequency region. As μ increases, the energy stored in the wake spectrum gradually shifts to a relative high-frequency region. Moreover, although the value of the wake spectrum in stern waves is very high in some frequency region, the wake amplitude is not so high compared with that in head waves. The reason is that the length of the frequency band containing energy in stern waves is much shorter than in head waves. Hence, the total energy that can be generated from the wake spectrum is not so large in stern waves. Subsequently, according to Eq. (4.32), the wake disturbance at each time is the superposition of several harmonic wake component. Therefore, in stern waves, the number of harmonic wake component that contributes to the wake disturbance at each time is lower than that in head waves. Finally, Figure 4.12 shows that the maximum wake amplitude increases as the Beaufort scale increases. This is because more energy is contained in the wake spectrum as the Beaufort scale is higher.

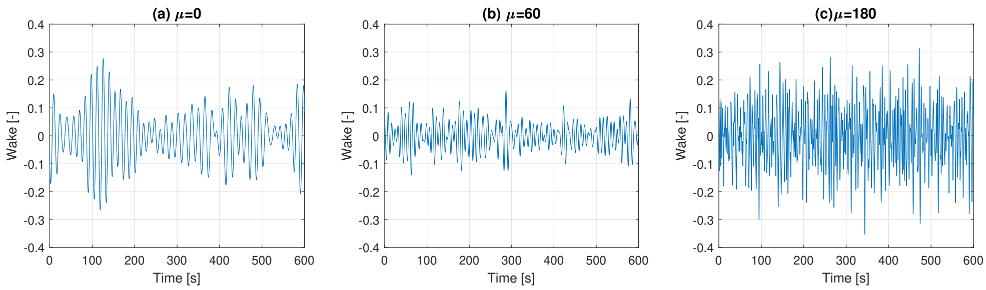

Figure 4.11: Three examples of the irregular disturbance of wake at $\mu = 0, 60$ and 180 [degree] when Beaufort scale is 7.

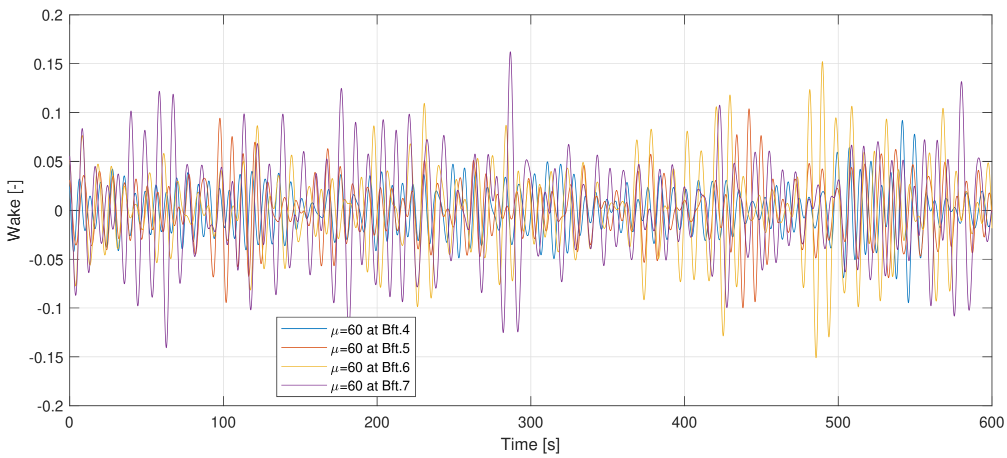

Figure 4.12: Irregular wake disturbance at $\mu = 60$ [degree] from Beaufort scale 4 to 7.

Link the wake disturbance to the linearised model

From Chapter 3, it can be noticed that the frequency-domain analysis for the linearised model of the wind-assisted ship propulsion system was conducted in normalization form. Considering this and following the research [Vrijdag and Schuttevaer, 2019], the wake spectrum in normalization form, which is used in Chapter 5, can be derived as :

$$
\begin{aligned}
\delta w &= \frac{cos(\mu) \cdot \omega_{wave} \cdot e^{k \cdot z_0}}{V_s} \cdot \delta \zeta_a \\
\rightarrow \frac{\delta w}{1-w} &= \frac{cos(\mu) \cdot \omega_{wave} \cdot e^{k \cdot z_0}}{V_s \cdot (1-w)} \cdot \frac{-z_0}{-z_0} \cdot \delta \zeta_a \\
\rightarrow \delta w^* &= \frac{cos(\mu) \cdot \omega_{wave} \cdot e^{k \cdot z_0} \cdot -z_0}{V_a} \cdot \delta \zeta_a^*
\end{aligned}
\tag{4.34}
$$

At this point, it has to mention that the wave amplitude is normalised with the depth of the hub. Subsequently, by defining a transfer function as: $H^* = \frac{cos(\mu) \cdot \omega_{wave} \cdot e^{k \cdot z_0} \cdot -z_0}{V_a}$, the wake spectrum in normalization form can be expressed as:

$$
S_{\delta w^*}(\omega_{wave,e,j}) = \sum_{j=1}^{N} (H^*(\omega_{wave,j}))^2 \cdot S_{wave'^*}(\omega_{wave,j}) \tag{4.35}
$$

where $S_{wave'^*}(\omega_{wave,j}) = \frac{S_{wave'}(\omega_{wave,j})}{z_0^2}$ and the value of N depends on the conditions used in the wake spectrum.

By applying Eq. (4.34) and (4.35), the wake spectrum in Figure 4.9 and 4.12 are transformed into their normalized form respectively and are illustrated in Figure 4.13 and 4.14 respectively.

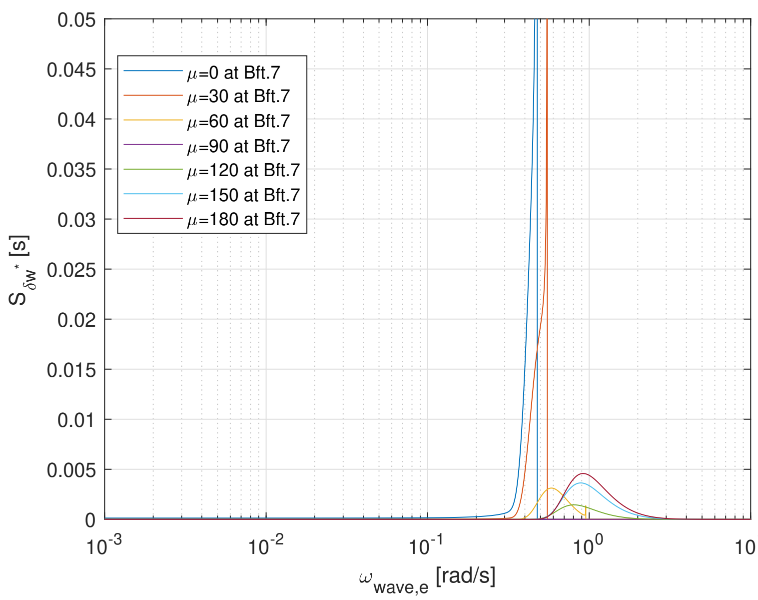

Figure 4.13: Normalised wake spectrum based on wave encounter frequency at Beaufort scale 7 for the ship sailing at 10 [knot] from head to stern waves.

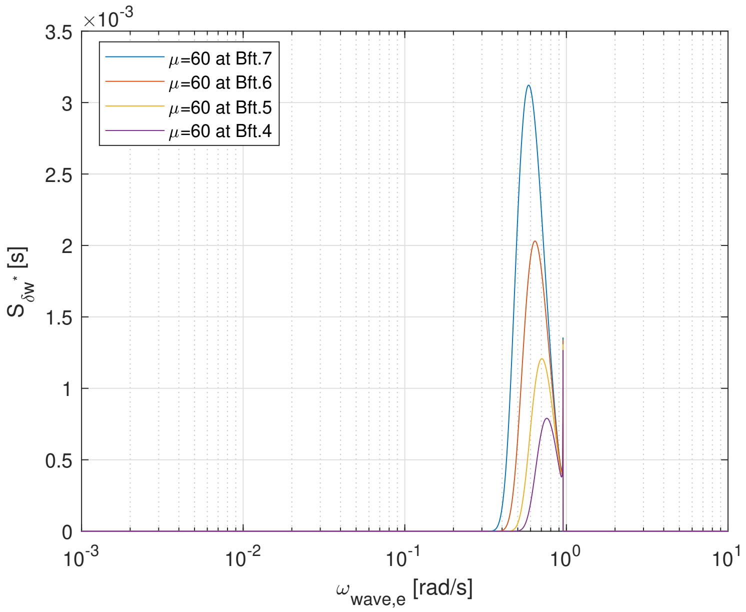

Figure 4.14: Normalised wake spectrum based on wave encounter frequency for the ship sailing at 10 [knot] for $\mu = 60$ [degree] from Beaufort scale 4 to 7.

4.4. Conclusions

With Frøya and Pierson-Moskowitz spectrum, the disturbances of true wind speed and wave amplitude at different Beaufort scales can be described quantitatively if the real data from measurement are unavailable. In addition, the impact of sea surface elevation on the advance velocity experienced by propeller hub in surge direction was also presented. Hence, the wake spectrum was firstly derived.

In this thesis, the Beaufort scale was used to define the status of wind and waves, and it has a strong effect on the amount of energy that can be excited from the marine environment. In general, as the Beaufort scale increases, the energy that can be conveyed from the spectrum to the disturbances of true wind speed and wave amplitude increase. Furthermore, a shift of the peak for the wave spectrum toward the high-frequency region can be found when the Beaufort scale decreases. In addition to the the wind spectrum, the wave spectrum sensed by the ship is influenced by the ship speed and it's heading relative to waves. Consequently, the wave encounter spectrum was derived based on the assumption that the ship speed is unchanged despite of the disturbances. Furthermore, the wake spectrum was also derived to model the wake disturbance sensed by the propeller hub. At this point, it has to mention that the wake spectrum usage has never been found and used in any literature. However, it would provide benefits for frequency-domain analysis, which is presented in Chapter 5.

By using those wind spectrum and the derived wake spectrum, the disturbances closer to real seaway are connected to the wind-assisted ship propulsion system in Chapter 5. Hence, the time-domain and frequency-domain analysis of the dynamic behavior of the wind-assisted ship propulsion system is carried in Chapter 5.

Chapter 5

Propulsion system responses to marine environment

5.1. Impact of irregular disturbances in time-domain analysis

In this section, two disturbances from the marine environment derived in Chapter 4 were connected to the wind-assisted ship propulsion system. In Chapter 3, to sail at the desired ship speed, 10 knots, the Flettner rotor generates 43.76 % and 26.16 % of the total thrust at Beaufort scale 7 and 6 under its favorable true wind angle. In this condition, the impact of true wind speed and wake disturbance, which induced by the sea surface elevation, on the system were investigated isolatedly from a time-domain perspective. Some phenomenons will be explained further by the frequency-domain analysis in Section 5.2.

5.1.1. Irregular wind

In reality, the true wind speed would be neither constant speed as shown in Chapter 2 or be as the sinusoidal form evaluated in Chapter 3. Instead, true wind speed that vary irregularly with time will be seen. To evaluate its impact on the wind-assisted ship propulsion system, the time series of true wind speed generated from the Frøya spectrum, which is regarded as the disturbance of true wind speed, will be added to the system via the way shown in Figure 2.11. Consequently, when the true wind angle is 120 [degree], a 10-minute and 1-hour time-domain simulation of the engine's behavior at Beaufort scale 6 and 7 are presented in Figure 5.1.

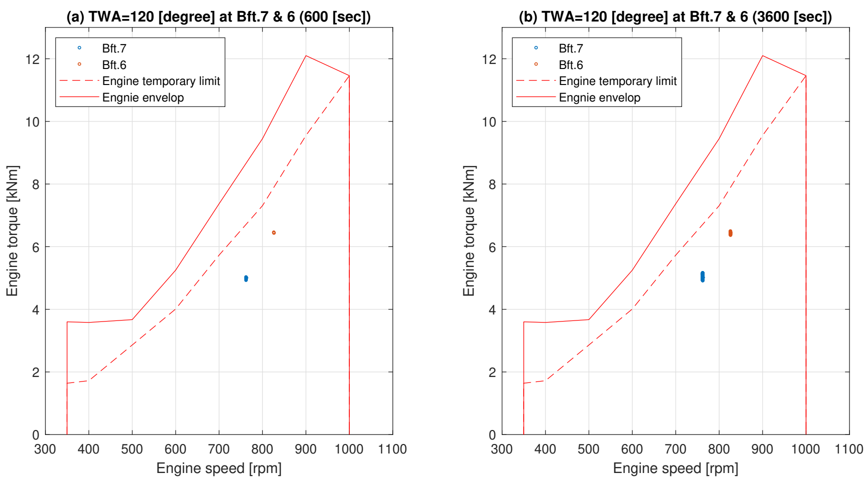

Figure 5.1: 10-minute and 1-hour time-domain simulation of the engine operating cloud at Beaufort scale 6 and 7. The ratio of the thrust generated by the Flettner rotor to the total thrust at Beaufort scale 7 and 6 are approximately 0.44 and 0.26 respectively.

Figure 5.1 show that the impact of true wind speed disturbance on the engine speed is minimal. This is in line with the results shown in Figure 3.5 (a) that the engine speed is not sensitive to the variation of true wind speed when the engine speed governor is introduced. Furthermore, a small variation of engine torque can be noticed in Figure 5.1. According to Figure 3.5 (c), the engine torque is more sensitive to the true wind disturbance compared with the engine speed. Therefore, a engine torque fluctuation can be noticed, and the 10-minute period is approximately equal to 0.01 [rad/s], which is located in the frequency region where the engine torque is not so resistant to the true wind disturbance. Moreover, Chapter 3 states that the engine torque becomes more activated to the regular variation of true wind speed in the low-frequency region. In addition, from Chapter 4, it can be seen that the wind spectrum contains more energy in the low-frequency region, which indicates a longer period. Therefore, a 60-minute time-domain simulation of the behavior of engine at Beaufort scale 6 and 7 are presented in Figure 5.1 (b), which shows a relatively larger variation of engine torque compared with the engine torque variation in Figure 5.1 (a). According to Figure 3.5 (c), this is results from the fact that the engine torque becomes more sensitive to the variation of true wind speed as its frequency decreases, which implies a longer period. Overall, from Figure 5.1 (a) and 5.1 (b), relatively larger variations of engine torque can be noticed when Beaufort scale increases, and the torque variation are not very large.

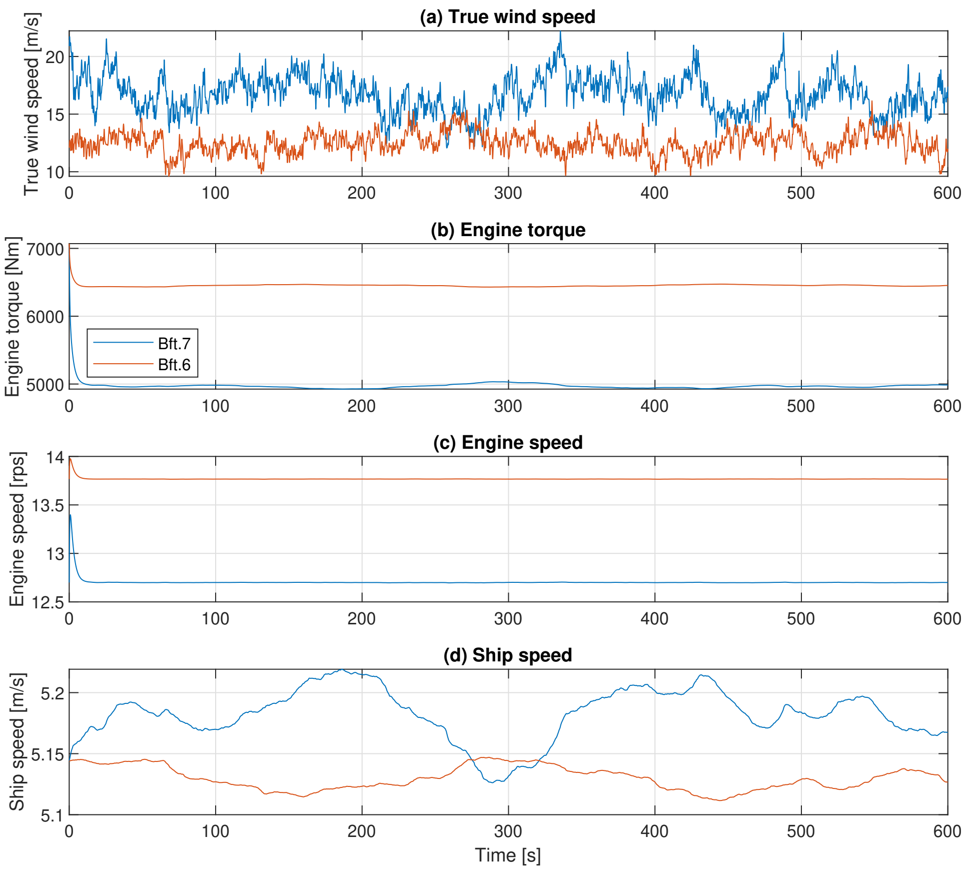

Figure 5.2: The response of the engine torque, engine speed and ship speed for a given true wind speed during a 10-minute time -domain simulation.

Figure 5.2 presents the time series of true wind speed, engine torque, engine speed, and ship speed for the 10-minute simulation. When looking at Figure 5.2 (d), the ship speed is influenced more by the true wind speed disturbance due to more fluctuations. Moreover, with the controller, the engine speed is almost constant. This indicates that the ship speed is influenced mainly by the thrust generated by the Flettner rotor. Because the rotor is implemented in the ship speed loop, the ship velocity will directly react to the true wind speed. Despite the quick variation of true wind speed, some of them would be filtered out by the total ship mass. In other words, due to unsteady acceleration result from the change of the rotor's thrust, it will require a longer period to change significantly the ship speed. Finally, Figure 5.2 (b) shows that there is a small peak of engine torque at Beaufort scale 7 from 200 to 400 [second], where a relatively stable acceleration and deceleration can be noticed in Figure 5.2 (d). The change of the ship speed makes the advance ship velocity, V_a, lower or higher, which in turn influences the angle of the inflow to the section of the propeller if the engine speed is constant. Therefore, under the condition, the propeller torque is changed by the variation of the angle of attack due to the ship speed. Besides, according to the literature [Branlard, 2010], the gust, which is defined as a sudden increases in wind speed [Veritas, 2010], can be generated while the time series of true wind speed is produced from a wind spectrum. As shown in Figure 5.2, a sudden increase of true wind speed at approximately t=20 [second] and t=490 [second] can be observed in 5.2 (a) . However, despite the ship speed being influenced by the gust, the period or the strength of these two gusts is not long or strong enough to result in a larger ship speed variation and thus the torque variation. Therefore, compared with the low frequency-varying true wind speed, the gust's impact on the engine torque, in this case, is not so significant.

5.1.2. Irregular wake

Similarly, the irregular amplitude of waves, which subsequently induces irregular wakefield, can be seen in reality. According to Chapter 4 that presents those occasional wakefield time series, they can be added to the wind-assisted propulsion system as the wake disturbance. This can be done in the way shown in Figure 2.11. Therefore, when μ is 60 [degree], which is the same as the true wind angle, 120 [degree], a 10-minute simulation for the impact of the wake disturbance on the engine at Beaufort scale 6 and 7 are shown in Figure 5.3 (b). Furthermore, the impact of head and stern waves on the propeller of the system at Beaufort scale 6 and 7 are also illustrated in Figure 5.3 (a) and (c).

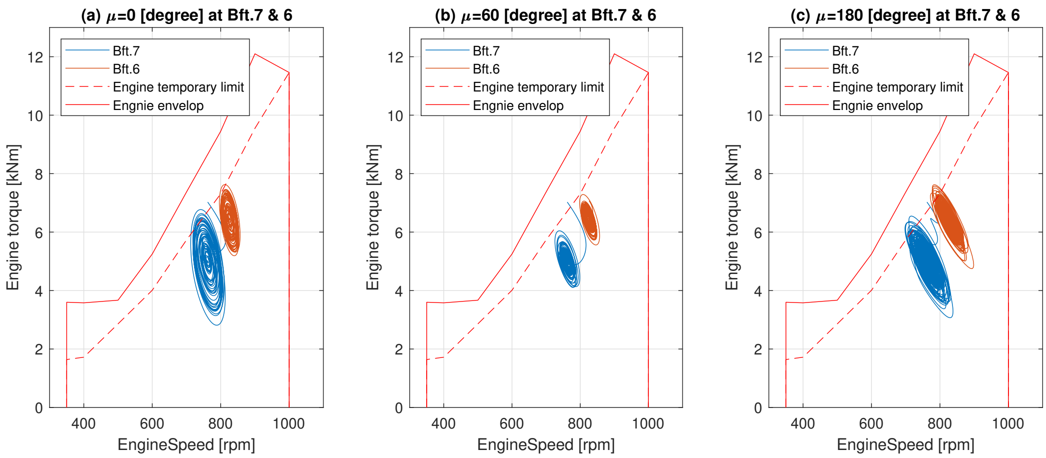

Figure 5.3: For heading relarive to waves is 0, 60 and 180 [degree], the engine operating cloud at Beaufort scale 6 and 7 under a favorable true wind angle.

In Figure 5.3, the variation of engine speed and torque lead to an engine operating cloud. Compared with the operating cloud in head waves, the operating cloud in stern waves becomes more vertical. This phenomenon was also found in the study [Vrijdag and Stapersma, 2017]. In addition, when μ is 60 [degree], it can be noticed that the size of the engine operating cloud becomes smaller because the strength of wake is decreased by the operator $cos(\mu)$ shown in Eq. (4.24). In other words, relatively less wake disturbance in surge direction is sensed by the propeller when the waves come from μ=60 [degree]. Overall, Figure 5.3 shows that the size of the engine operating cloud increases when the Beaufort scale increases.

Figure 5.4 shows the time series of wakefield, engine torque, engine speed, and ship speed for a 10-minute simulation under different conditions. Compared with the wind speed disturbance, the variation of wake strongly affects the engine torque and speed because it connects to the shaft speed loop directly. Compared with the variation of ship speed due to the true wind speed disturbance, a smaller fluctuation of ship speed can be noticed in Figure 5.4 (j), (k) and (i). In addition, it can also be noticed that the frequency of variation of engine torque, engine speed, and ship speed is very close to the frequency of wake disturbance. The frequency of those responses increases as the heading relative to waves, μ, changes from 0 to 180 [degree]. The further insight of those responses will be presented in the next section based on a frequency-domain analysis.

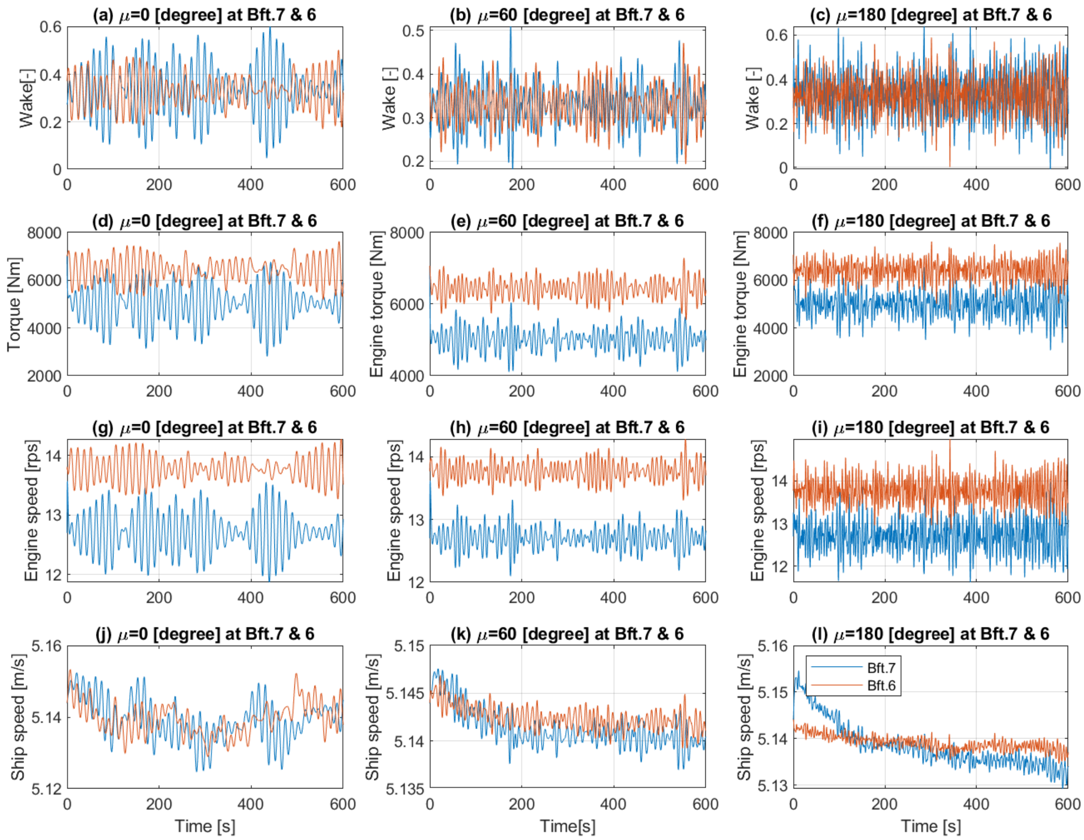

Figure 5.4: For heading relative to waves is 0, 60 and 180 [degree] under a favorable true wind angle, the response of the engine torque, engine speed and ship speed for a given wakefield during a 10-minute time -domain simulation.

In addition to the engine torque, a 10-minute simulation for the location of engine operating point in Specific Fuel Consumption curves (SFC curves) are presented in Figure 5.5. Despite the variation of engine power and speed for each engine point due to the true wind speed disturbance, the specific fuel consumption of each engine operating point for this case study, in general, does not increase significantly, which indicates that the engine efficiency is still acceptable. According to the literature [Woud and Stapersma, 2002], below 25% to 40% torque, the combustion in the engine probably becomes too cold, and the fouling of the cylinder will occur. For the selected case, this engine does not suffer this issue under its favor wind direction at Beaufort scale 6 and 7.

Under this dynamic condition, it also be worth investigating the total fuel consumption compared with that in steady condition. Without considering the extra amount of fuel required to spin the Flettner rotor, the total fuel consumption, $m_{f,total}$, in a given period can be calculated as:

$$m_{f,total}(T) = \int_0^T \dot{m}_f(t)\, dt \tag{5.1}$$

where T is the total simulation period, and $\dot{m}_f$, is the required amount of fuel per second that can be obtained from Eq. (2.24).

To make a fair comparisons, the relative total amount of fuel saving, SA, is defined as:

$$SA = \frac{m_{f,\ total,\ baseline} - m_{f,\ total,\ condition}}{m_{f,\ total,\ baseline}} [-] \tag{5.2}$$

in which $m_{f,\ total,\ baseline}$, is the total amount of fuel for the baseline design that the ship speed 10 [knot] without the assistance of the Flettner rotor. Secondly, $m_{f,\ total,\ condition}$ is the total amount of fuel for each condition which is shown in Table 5.1.

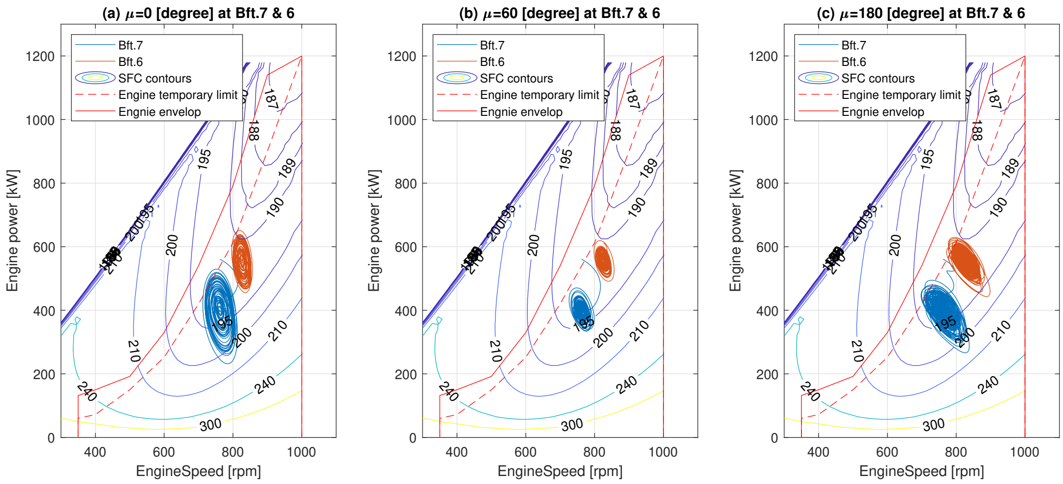

Figure 5.5: For heading relative to waves is 0, 60 and 180 [degree] under a favorable true wind angle, the engine operating cloud at Beaufort scale 6 and 7. Note that the y-axis is engine power instead of engine torque.

Table 5.1 shows the relative total amount of fuel saved under each given condition for a 10-minute simulation. The static condition means the steady engine operating point at Beaufort scale 6 and 7, shown in Table 2.2. According to Table 5.1, the relative total amount of fuel saved for the static and dynamic condition are almost the same at each Beaufort scale. Moreover, in the simulations, it can also be noticed that the relative total amount of fuel saving in the dynamic condition is relatively higher than in a static situation.

Relative total amount of fuel saving [%]				
μ [degree]	0	60	180	Static condition
Bft .7	49.72	49.66	49.83	49.60
Bft .6	31.07	30.96	31.12	30.91

Table 5.1: Relative total amount of fuel saving for the wind-assisted propulsion system during the 10-minute simulation. Note that the wind-assisted ship propulsion is operated at it's favorable true wind angle and true wind speed.

5.1.3. Conclusions from the time-domain simulations

For the selected case with a specific controller, as the Beaufort scale increase, the size of the operating cloud becomes bigger. Compared with true wind speed disturbance, wake disturbance influences the engine speed and torque significantly. However, the wake disturbance has less impact on the dynamic behavior of ship speed, whereas the true wind speed disturbance influences the ship speed directly.

However, it is still insufficient to unveil the dynamic behavior of the system from a time-domain perspective because the phase angles used to generate the irregular disturbances are chosen randomly.

Furthermore, one of the negative results is that the most considerable disturbance, which is significant for an extreme response, might never occur during the time-domain simulation. This probably influences the interpretation of results when extreme values are required [Journee and Pinkster, 1997]. Therefore, the frequency-domain analysis based on the regular inputs from the marine environment is believed to provide more insight into the phenomenon and was conducted in the following sections.

5.2. Impact of disturbances in frequency-domain analysis

To further investigate the primary research objective: to what extent, do the wind and wave disturbances from the marine environment influence the system, the frequency-domain analysis was conducted for obtaining the system response spectrum in terms of engine speed, engine torque, and ship speed. And this energy spectrum can be found by applying a transfer function.

In general, a response spectrum can be used to describe the spectral density of the system response at a series of frequencies. Regarding its application, it has been widely used in obtaining the response spectrum of a vessel's motion in a given sea condition. For example, by applying a transfer function called the Response Amplitude Operators (RAO) which linearly represents a response of a specific ship motion to waves' amplitude at each frequency, the response spectrum this specific ship's motion, under the assumptions of the linearity and superposition, can be derived as [Journee and Pinkster, 1997]:

$$S_r(\omega_e) = \left| \frac{r_a}{\zeta_a}(\omega_e) \right|^2 \cdot S_{\zeta_a}(\omega_e) \tag{5.3}$$

where $S_r(\omega_e)$ is the response spectrum of a specific motion, r_a is the response of a specific motion at each frequency, ζ_a is the wave amplitude and S_{ζ_a} is the wave spectrum. Note that the wave spectrum can be a certain wave spectrum. In this way, the response spectrum of a certain degree of motion at a given wave spectrum can be derived.

Similarly, to answer the main research question, the response spectrum for the wind-assisted ship propulsion can be used. To obtain its response spectrum, the transfer functions and the environment spectrum describing the disturbances of wind and wakefield induced by waves are required. Both of them are already derived in previous chapters, which is the Bode magnitude plots presented in Chapter 3 and the spectrum of wind and wave shown in Chapter 4. Furthermore, because the bode magnitude plot presented in Chapter 3 is the linear relationship between the system responses and the regular disturbances, the response spectrum in terms of engine speed, engine torque, and ship speed can be derived and presented in the following sections. Besides, from the time-domain simulation, it can be seen that the engine operating cloud does not touch the engine envelop, which also implies that the derived linearised system can be used if the hard limit is not presented during the simulation.

5.2.1. Wind

To investigate the impact of the true wind speed's disturbance on the wind-assisted propulsion system in terms of its engine speed, engine torque, and ship speed, their response spectrum can be derived by:

$$S_{\delta n^*}(\omega_{wind}) = \left| H_{\frac{\delta n^*}{\delta TWS^*}}(\omega_{wind}) \right|^2 \cdot S_{\delta TWS^*}(\omega_{wind}) \tag{5.4}$$

$$S_{\delta M_b^*}(\omega_{wind}) = \left| H_{\frac{\delta M_b^*}{\delta TWS^*}}(\omega_{wind}) \right|^2 \cdot S_{\delta TWS^*}(\omega_{wind}) \tag{5.5}$$

$$S_{\delta V_s^*}(\omega_{wind}) = \left| H_{\frac{\delta V_s^*}{\delta TWS^*}}(\omega_{wind}) \right|^2 \cdot S_{\delta TWS^*}(\omega_{wind}) \tag{5.6}$$

where H represents transfer functions which can be illustrated in Bode magnitude plot shown in Chapter 3. Based on Eq. (5.4), (5.5) and (5.6), Figure 5.6 illustrates the process for obtaining the response spectrum from the wind spectrum via those three transfer functions.

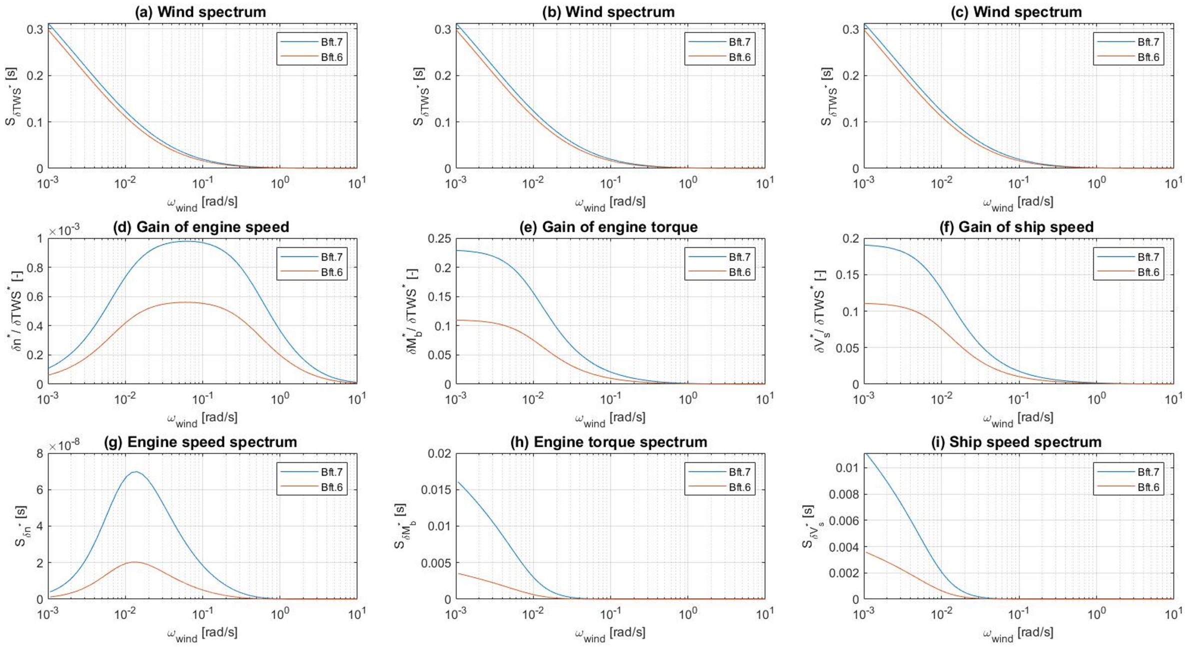

Figure 5.6: Response spectrum based on the wind spectrum via each transfer function at Beaufort scale 6 and 7.

Firstly, Figure 5.6 (a), (b) and (c) represent the wind spectrum in normalization form as a function of wind frequency. Subsequently, for the ship sails at 10 knots when TWA =120 [degree] at Bft.6 and Bft.7, the transfer functions regarding the variation of the engine speed, the engine torque, and the ship speed under those two operation conditions are shown in Figure 5.6 (d), (e) and (f). Finally, by multiplying the value of the wind spectrum density shown in Figure 5.6 (a), (b) and (c) with the square of the values shown in Figure 5.6 (d), (e) and (f) at each corresponding frequency, the system responses spectrum in terms of the variation for the engine speed, the engine torque and the ship speed under those two conditions can be obtained and are shown in Figure 5.6 (g), (h) and (i). For example, the response spectrum for the variation of the engine speed shown in Figure 5.6 (g) can be obtained by multiplying the value of the wind spectrum density shown in Figure 5.6 (a) with the square of the transfer function shown in Figure 5.6 (g) at each frequency. That is, by a multiplication with a certain transfer function, each regular component from the wind spectrum can be linearly transferred to a regular component of the system response spectrum.

Figure 5.6 (g) shows that the peak of the engine speed response can be found when the absolute wind frequency is approximately 0.01 [rad/s]. Although the wind spectral density keeps increasing with increase in wind frequency, the spectra density of the engine speed decreases because the engine speed becomes less and less sensitive to the variation of the true wind speed in low frequency region. Overall, the value of the engine speed response spectrum at each wind frequency is very low, which in line with the time-domain simulation that the engine speed remains almost constant despite the fluctuation of true wind speed.

Regarding the response spectrum of variation of the engine torque and the ship speed shown in Figure 5.6 (g) and (i), a similar distribution of response spectra density can be found. Although the wind spectrum contains some energy from 0.1 to 1 [rad/s], the value for the response spectrum of the engine torque and ship speed within this range is relatively low. This is result from the fact that the transfer function of the engine torque and ship speed have relatively low values in this wind frequency region. However, when the frequency of the wind lies between 0.001 and 0.1 [rad/s] corresponding to approximately 6283 and 628 seconds respectively, a relatively higher of response spectrum of the engine torque and ship speed can be noticed due to relatively higher values of the wind spectrum and transfer functions. Furthermore, in the region where the wind frequency is approximately between 0.001 to 0.004, the slope of engine torque and ship speed response spectrum shown in Figure 5.6 (h) and (i) become lower. This is due to the fact that the values of the engine torque and ship speed transfer function, presented in Figure 5.6 (e) and (f) increase at a lower rate in this wind frequency region.

Overall, for the selected case with a specific controller under the chosen operational condition, when the Beaufort scale is 6, the response spectrum of the variation of the engine speed, the engine torque, and the ship speed to true wind speed is roughly half of those values at Beaufort scale 7. In addition, the response of engine speed to true wind speed is very low, and the engine torque and ship speed are more sensitive to the fluctuation of true wind speed in low-frequency region.

5.2.2. Wave

Because fluctuations of wave amplitude induces the wake disturbances, a wake spectrum was derived from a wave encounter spectrum in Chapter 3, and the response spectrum will be derived based on the derived wake spectrum.

Wake disturbance at different Beaufort scales

The response spectrum of the engine speed, the engine torque, and the ship speed to wake disturbance can be derived by following the same procedure for obtaining their response spectrum to the wind spectrum. Thus, based on the derived wake spectrum, the response spectrum in terms of the engine speed, the engine torque and the ship speed can be derived by:

$$S_{\delta n^*}(\omega_{wake,e}) = \left| H_{\frac{\delta n^*}{\delta w^*}}(\omega_{wake,e}) \right|^2 \cdot S_{\delta w^*}(\omega_{wake,e}) \tag{5.7}$$

$$S_{\delta M_b^*}(\omega_{wake,e}) = \left| H_{\frac{\delta M_b^*}{\delta w^*}}(\omega_{wake,e}) \right|^2 \cdot S_{\delta w^*}(\omega_{wake,e}) \tag{5.8}$$

$$S_{\delta V_s^*}(\omega_{wake,e}) = \left| H_{\frac{\delta V_s^*}{\delta w^*}}(\omega_{wake,e}) \right|^2 \cdot S_{\delta w^*}(\omega_{wake,e}) \tag{5.9}$$

Similarly, by applying Eq. (5.7) , Eq. (5.7) and Eq. (5.7), the response spectrum for the variation of the engine speed, engine torque and ship speed are shown in Figure 5.7 (g), (h) and (i) respectively.

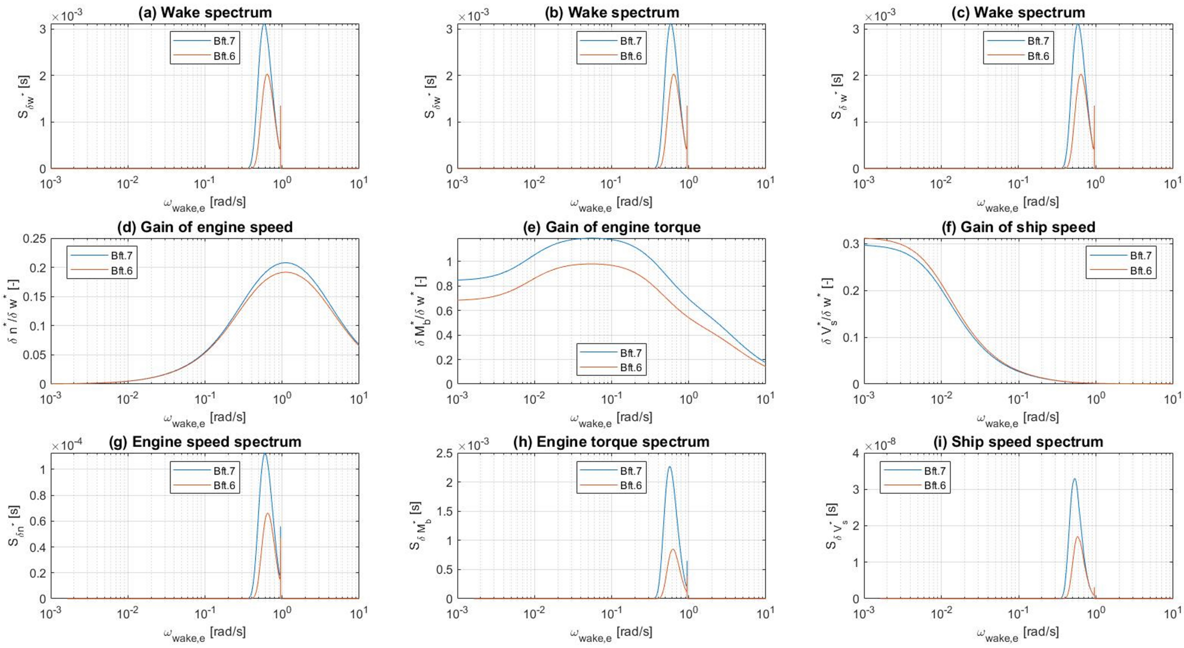

Figure 5.7: Response spectrum based on the wake spectrum via each transfer function at Beaufort scale 6 and 7.

To begin with, compared with response spectrum of the variation of ship speed shown in Figure 5.7 (i), some peaks with a relatively higher value can be found in Figure 5.7 (g) and (h), which represent the response spectrum of the variation of the engine speed and torque. Besides, it can also be noticed that the system is only be activated within a specific frequency region. These are results from the fact that wake spectrum only contain energy within the frequency region that can be conveyed to the system via each transfer function, and its maximum value for each response spectrum is found at the same frequency as the wake spectrum.

Furthermore, Figure 5.7 (a), (b) and (c) show that the location of peak value for wake spectrum at Beaufort 6 shifts to a relatively higher frequency location. Compared with the engine torque transfer function shown in Figure 5.7 (e), the location of this peak value for wake spectrum is closer to the frequency region where the engine speed is more sensitive to wake disturbance and this can be seen in Figure 5.7 (d). Therefore, although more energy exists in the wake spectrum at Beaufort scale 7, the difference between the peak value for engine speed response spectrum at Beaufort scale 6 and 7 becomes relatively smaller compared with that for engine torque response spectrum, and this phenomenon can be noticed in Figure 5.7 (g).

Regarding the response spectrum of the variation of the ship speed shown in Figure 5.7 (i), although two peak values can be noticed at approximately 05 [rad/s] , the values of this ship speed response spectrum are relatively lower. From Figure 5.7 (c) and (f), it is clear that the frequency region where the wake spectrum contains energy does not overlapped with the frequency region, 0.001 to 0.1 [rad/s], where the ship speed would be very sensitive to the wake disturbance. Consequently, under the selected operation condition for the selected case, the variation of wake does not influence the ship speed significantly.

Wake at different ship's heading relative to waves

In Chapter 4, the ship's heading relative to waves has an impact on the energy distribution in the wake spectrum based on the wave encounter frequency. Especially for the wake spectrum in the following seas, more energy can be found in the low-frequency region than in the head seas. Therefore, Figure 5.8 shows the impact of ship's heading relative to waves on the system.

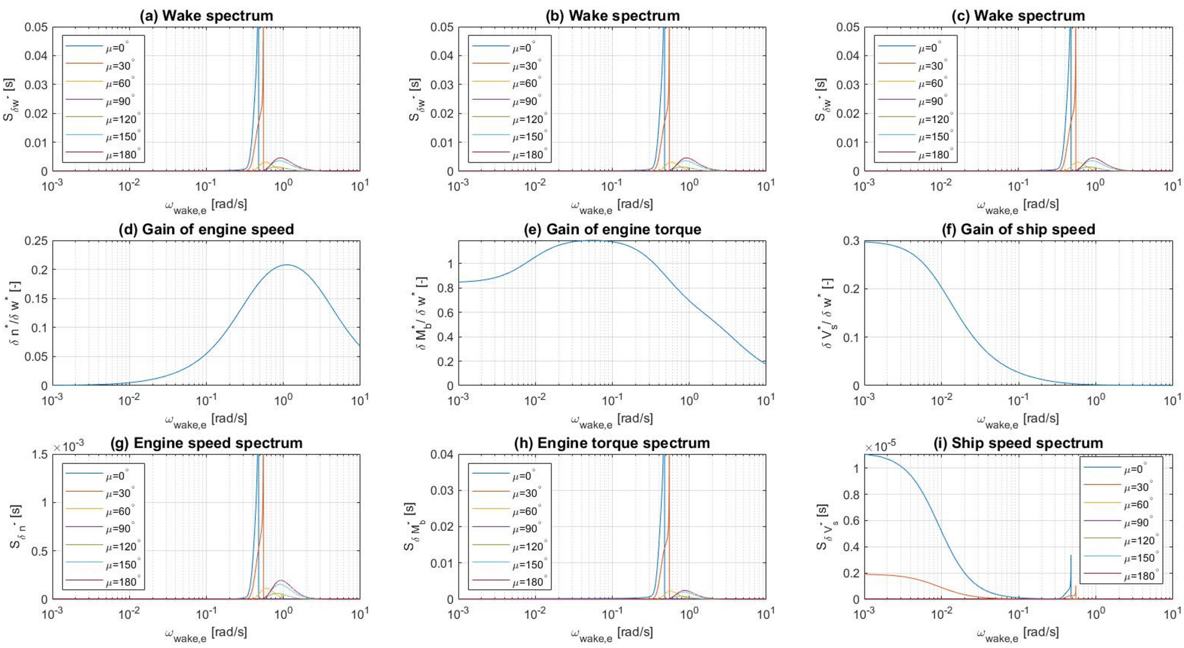

Figure 5.8: Response spectrum based on the wake spectrum via each transfer function at Beaufort scale 7 with different angles of heading relative to waves.

Regarding the impact of wake on engine speed, Figure 5.8 (g) shows that the engine speed response spectrum is gradually enlarged from μ =0 to 180 [degree] compared with the wake spectrum shown in Figure 5.8 (a). This is due to the fact that the wake spectrum from μ =0 to 180 [degree] is located in the frequency region where the engine speed becomes more and more sensitive to wake disturbance. On the other hand, concerning the engine torque, Figure 5.8 (h) implies that the value of engine torque response spectrum is gradually reduced from μ =0 to 180 [degree] compared with the wake spectrum shown in Figure 5.8 (b). This can be explained by the fact that the wake spectrum from μ=0 to 180 [degree] is located in the frequency region where the engine torque is gradually less sensitive to wake disturbance. A clear phenomenon of this result is that the difference between the peak value of the engine torque response spectrum at μ =0 and μ =60 is less. Finally, When it comes to the ship speed response, Figure 5.8 (i) shows that the impact of wake on it is minimal.

In addition to the value of response spectrum, the length of its frequency band, is also important because it determines how much the energy can be conveyed from the wake spectrum to the response spectrum. In Figure 5.8 (g) and (h), the frequency band becomes gradually longer from stern to head waves. This also indicates that the frequency range that the wake disturbance can excite the wind-assisted propulsion system becomes gradually longer. Because the irregular wakes are the superposition of a number of a harmonic wake with random phase angles, the magnitude of irregular wake in head waves, in this case, is composed of a higher number of harmonic wake with different frequencies. Hence, although the value of the wake spectra density for head waves is relatively low compared with that for stern waves, the magnitude of irregular wakes for head waves at a time step might be close to that for the stern waves. Furthermore, under head waves, the impact of the wake on engine speed and torque are enlarged and diminished. Consequently, in Figure 5.3, the operating cloud in head waves is less vertical because of the relatively higher engine speed variation.

Besides, although the response spectral density of engine speed and torque in stern waves are very high, their variation shown in Figure 5.4 is not so high compared with that in head waves. The reason is that the length of the frequency band containing energy in both engine speed and torque response spectrum are much shorter than that in head waves. To see the frequency band in the real scale clearly instead of the logarithmic scale used previously, the x-axis in Figure 5.8 (g) and (h) are transferred from the original logarithmic scale to the real scale and they are shown in Figure 5.9. Furthermore, the magnitude of engine speed and torque in time-domain simulation are regarded as the superposition of several harmonic components with random phase angle in the linear system. Therefore, for the following waves, the number of harmonic components contributing to the magnitude at each time is lower than in head waves.

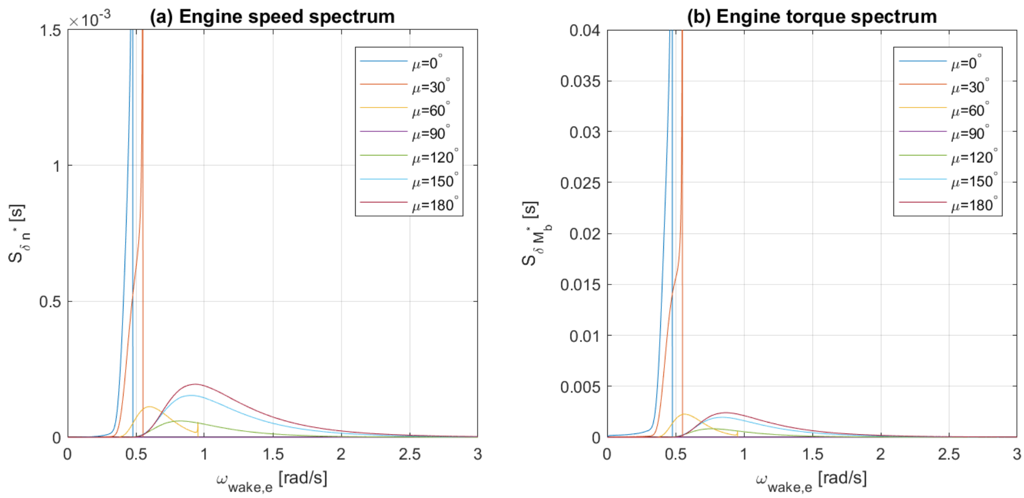

Figure 5.9: Variation of the engine speed and torque response spectrum based on a real scale of x-axis at Beaufort scale 7.

5.2.3. Conclusions from the frequency-domain simulations

Compared with time-domain analysis for the selected case with a specific controller, the frequency-domain analysis shows clearly how the wind and wake disturbance are conveyed from their spectrum to the system response spectrum through each transfer function. Furthermore, the fluctuation of true wind speed and wake generated by wave amplitude disturbance, in fact, influence the diesel engine through the propeller, which is illustrated in Figure 5.10.

After the analysis of the impact of true wind speed disturbance, it can be concluded that the ship speed is more sensitive to low-frequency variation of true wind speed. Furthermore, the introduction of the engine speed controller enables the engine speed to resist the variation of true wind speed very well. Hence, the propeller rotational speed will be unchanged. Consequently, as shown in Figure 5.10 (a) that presents a section of a propeller, the angle of attack, α, will be changed due to the variation of the ship speed in this situation. This results in the variation of the propeller torque and then the variation of engine torque. If the true wind speed disturbance with low-frequency variation is sensed by the ship, which makes it be steadily accelerated and decelerated in a relatively longer period, a relatively higher variation of engine torque would be generated.

Regarding the impact of the variation of wake disturbance induced by the time-varying wave amplitude, it can be concluded that the wake disturbance has less effect on the variation of the ship speed. From the frequency-domain analysis in the given operational condition, this is because the frequency range where the ship speed is more sensitive to the variation of wake disturbance does not overlap with that of the wake spectrum. Therefore, as shown in Figure 5.10 (b), the variation of the angle of attack is mainly due to the variation of wakefield and the engine speed shown in blue color, which subsequently changes the engine torque.

Concerning the response of engine speed and torque to wake disturbance from stern to head waves, the response of engine speed is gradually enlarged, whereas the engine torque is diminished. The reason is that the slope of the engine speed transfer function is positive in the frequency region corresponding to the frequency band of the wake spectrum. On the other hand, the slope of the engine torque transfer function is negative in the frequency region. Consequently, a relatively more substantial variation of engine speed and a relatively less engine torque would make the engine operating cloud less vertical in head waves.

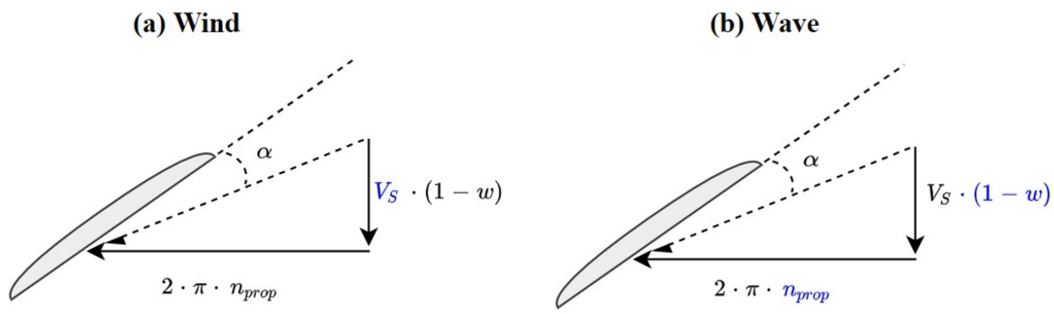

Figure 5.10: A view of the propeller section and it relations with the ship speed, the wake disturbance induced by wave amplitude disturbance and the propeller rotational speed.

5.3. Sensitivity analysis

From the previous sections, the acceleration and deceleration of the ship is influenced directly by the time-varying true wind speed. Considering the variation of ship speed is the result of ship speed loop containing the total ship mass, it would be beneficial to investigate its impact on the wind-assisted ship propulsion system. In addition to the total ship mass, the influences of the moment of inertia in the shaft speed loop will also be investigated. At this point, it has to mentioned that the system dynamic behavior is also determined by the parameters used in the wind-assisted ship. Note that despite the change of those parameters, it is assumed that the system's static behavior is unchanged. For example, although the total ship mass becomes two times higher than the given case, its resistance remains unchanged. Another factor that influences the dynamic behavior of the wind-assisted ship propulsion system is the setting of the PI controller, and its response to the wake disturbance for a conventional propulsion system was already investigated systematically in [Vrijdag and Stapersma, 2017]. Therefore, only the impact of the different total ship mass and the moment of inertia will be investigated in the thesis.

5.3.1. Total ship mass

By replacing the original total ship mass, m_{ship}, with $2 \cdot m_{ship}$ and $0.5 \cdot m_{ship}$ respectively, the Bode magnitude plots of the wind-assisted ship propulsion system with different total ship mass are shown in Figure 5.11. Note that the plots on the left-hand and right-hand side are the impact of true wind speed and wake disturbance on the system.

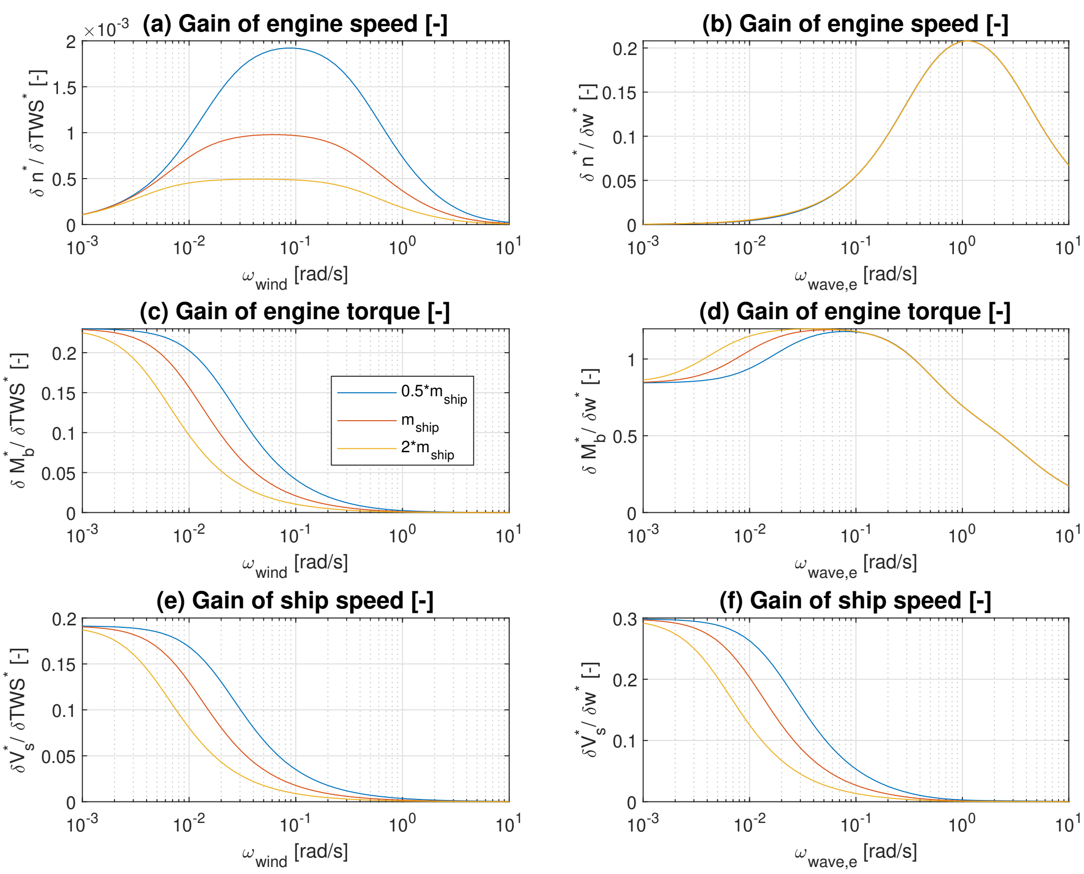

Figure 5.11: Bode magnitude plots of the wind-assisted ship propulsion system with different total ship mass at Beaufort scale 7.

In Figure 5.11, except Figure 5.11 (d), it can be seen that the increase of total ship mass has a strong effect of reducing the sensitivity of the system to variation of true wind speed and wakes. The changed of the ship's total mass influences the dynamic behavior of the ship speed loop firstly. As the total ship mass increases, less acceleration can be generated with a given net force. Consequently, the impact of disturbances on the system decreases. However, Figure 5.11 (d) shows a completely different result in the low-frequency region. One of the reasons for this phenomenon is that a higher propeller force is required for the heavier ship during acceleration and deceleration, resulting in a higher variation of engine torque in the low-frequency region where the controller have a relatively poor performance.

5.3.2. Inertia of moment

Similarly, replacing the original inertia of moment, I_p, with $2 \cdot I_p$ and $0.5 \cdot I_p$, the Bode magnitude plots of the wind-assisted ship propulsion system are shown in Figure 5.12.

The impact of the different inertia of moment on the system can be seen clearly in Figure 5.12 (b) and (d). The variation of engine speed and torque results from the shaft speed loop, including the inertia of the moment. Within the low-frequency region in Figure 5.12 (b), the controller has a good performance of resisting the engine speed to the variation of wake disturbance. On the other hand, in Figure 5.12 (d), a relatively poor performance for the engine torque to resist the wake disturbance can also be noticed in low-frequency region. For the role of the inertia of the moment in high-frequency region, it acts as a filter that filters out the high-frequency wake disturbance that pasted to the system. Consequently, the wake disturbance does not influence the engine speed and torque significantly. However, if a lower inertia of moment, such as $0.5 \cdot I_p$, is adopted, Figure 5.12 (b) and (d) depict that the engine speed and torque response increase significantly in the high-frequency region.

For the region between high-frequency and low-frequency wake disturbance in Figure 5.12 (b), the controller (an engine speed governor) does not perform well, which results in a relatively higher response of engine speed. In the corresponding frequency region in Figure 5.12 (d) , it can be noticed that the response of engine torque becomes higher.

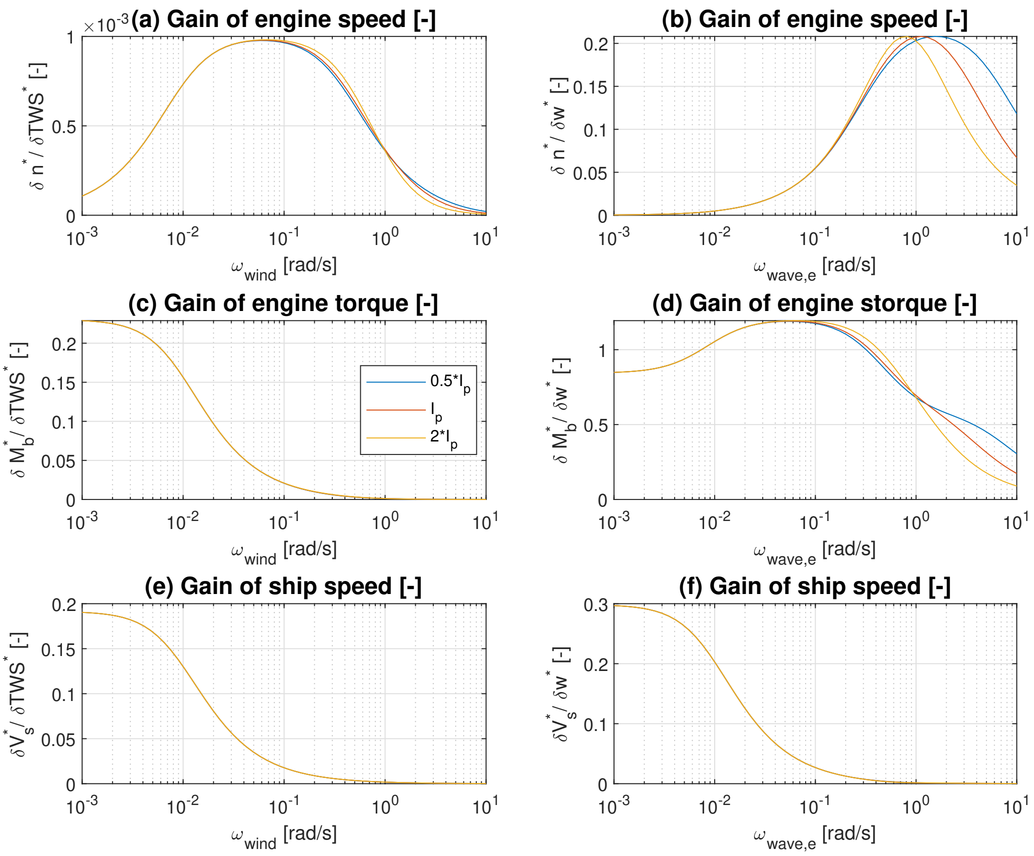

Figure 5.12: Bode magnitude plots of the wind-assisted propulsion ship system with different inertia of moment at Beaufort scale 7.

5.3.3. Conclusions from the sensitivity study

With the derived linearised wind-assisted ship propulsion model, the frequency-domain analysis provides a systematical insight into the impact of parameters on the system, which might benefit the designer in having a quick overview of the dynamic behavior of the system.

Based on the sensitivity study for the case with a specific engine speed governor, the increase in ship total mass, in general, enables the system be less sensitive to the true wind speed and wake disturbance, but this increases the engine torque response to wake disturbance in the low-frequency region. However, the influence for the rise of inertia of the moment on the system might not be so positive, because this enlarges the response of engine speed and torque to the wake disturbance in the frequency region where the controller has a relatively poor performance and a lot of energy is contained in the wake spectrum.

5.4. Conclusions

For the wind-assisted ship propulsion system, especially the selected case with a specific controller(engine speed governor) at it favorable true wind angle, some conclusions are made here when approximately 44 % and 26 % of the thrust is provided by the Flettner rotor at Beaufort scale 7 and 6.

As Beaufort scale increases, the strength of true wind speed disturbance becomes stronger and then it directly influences the ship speed. Due to the controller which enables the engine speed to be resistant to the true wind speed disturbance, the engine speed is not influenced significantly, but the engine torque is influenced slightly when the ship speed is steadily accelerated and decelerated by the true wind speed disturbance. On the other hand, compared with true wind speed disturbance, the engine speed and torque are more sensitive to the wake disturbance and thus the fluctuation of engine speed and torque are generated. Consequently, a clear engine operating cloud whose size increases as Beaufort scale increases can be noticed. However, the ship speed is not influenced by the wake disturbance significantly.

To give a more insight into the system, the frequency-domain analysis was carried by connecting the Bode magnitude plots derived in Chapter 3 with the wind and wake spectrum obtained in Chapter 4. As a result, the system response spectrum, which shows the system response in a more realistic seaway, can be obtained. Based on the linear theory, it was found that only the overlap of the transfer function's frequency region corresponding with that of a particular wind and wake spectrum, the system will be excited by the irregular disturbances. Furthermore, by combining the environmental spectrum and the system transfer functions, it will be clear to track how the energy is conveyed from the marine environment to the system. Finally, the contribution from the harmonic component in the wind and wake spectrum to the system response spectrum at each frequency can also be seen clearly.

Overall, with the linearised model that can be regarded as an additional tool to analyze a system [Stapersma and Vrijdag, 2017] [Vrijdag and Stapersma, 2017] [Vrijdag and Schuttevaer, 2019], how the marine disturbances influence the wind-assisted ship propulsion system can be seen clearly. Besides, the impact of different parameters on the dynamic behavior of the wind-assisted propulsion system can be also be seen clearly and systematically from the frequency-domain analysis.

Chapter 6

Conclusions & Recommendations

6.1. Conclusions

In Chapter 1, the main research question for this thesis is:

To what extent, do wind and wave at different Beaufort scales influence the performance of the wind-assisted ship, especially for the propulsion diesel engine in the selected case?

To address this question, the Beaufort scale, in this thesis, is utilized as an indicator to describe the wind, the sea state, and the operational condition of the wind-assisted ship propulsion system. Moreover, following the research [van der Kolk et al., 2019], which analyzed the static behavior of the vessel, CF5000, it's dynamic behavior can be evaluated by the time-domain and frequency-domain analysis of the same case with a Flettner rotor and a controller.

Regarding the first research objective, the nonlinear parametric model of the wind-assisted ship propulsion system is derived by adding a Flettner rotor into the ship speed loop used in the conventional ship propulsion model derived by [Vrijdag and Stapersma, 2017]. Because the wind sensed by the Flettner rotor is apparent wind instead of true wind, an additional submodel that transfers the true wind to apparent wind at different Beaufort scales is also included. On the other hand, an engine model [Shi et al., 2010] that considers the impact of fuel input and engine speed on engine performance is also adopted. Consequently, Chapter 2 indicates that under the condition of the favorable true wind angle, the desired ship speed can be achieved by using less engine power and less engine speed as the Beaufort scale increases. And waves influence the system via the propeller by the wake disturbance.

Concerning the second research objective, the Frøya wind spectrum and Pierson Moskowitz wave spectrum were employed to quantify the wind and waves at different Beaufort scales. Because one of the disturbances to the wind-assisted ship propulsion system, in this case, is the wake disturbance instead of the wave amplitude used in [Vrijdag and Schuttevaer, 2019], a wake spectrum based on the wave encounter spectrum was derived. Consequently, based on the wind and wake spectrum that describe the wind and wake disturbance from a frequency-domain perspective, the time series of true wind speed and wake fraction at different Beaufort scales can be obtained. According to Chapter 4, the strength of both disturbances increases as the Beaufort scale increases. Furthermore, from stern to head waves, the energy contained in wave and wake spectrum gradually shifts from the low-frequency to high-frequency regions.

For the third research objective, wind and wake disturbance are included into the wind-assisted ship propulsion system with a specific controller. To get more insight into the system, its linearised model was derived by linearizing and normalizing the nonlinear model around its equilibrium. Hence, the frequency-domain analysis can be conducted based on Bode magnitude plots, representing how a system responds (engine torque, engine speed, and ship speed) to a regular disturbance (true wind speed and wake) at each frequency. This provides a foundation to understand how the system reacts to irregular disturbances. As a result, Chapter 3 shows that although the introduction of the controller makes the ship speed more sensitive to wake disturbance, it enables the engine speed to become less sensitive to the variation of true wind speed and wake fraction. Moreover, the controller performs very well for the engine speed to strongly resist the variation of true wind speed and wake in the low-frequency region. In the high-frequency region, both disturbances are gradually filtered out by the ship mass and the moment of inertia.

Finally, by implementing irregular disturbance of true wind speed and wake fraction into the wind-assisted ship propulsion system, it was found that the impact of true wind speed disturbance on the dynamic behavior of the engine torque and engine speed are not significant. Although the rotor generates approximately 44 % of the total thrust at Beaufort scale 7 and some gust can be noticed during the time-domain simulation, the impact of the true wind speed disturbance on the dynamic behavior of the propulsion engine is still relatively low compared with that of wake disturbance on the engine. On the other hand, the ship speed is more sensitive to the true wind speed disturbance, but it is not very sensitive to wake disturbance. Moreover, as the Beaufort scale increases, the fluctuation of engine speed, engine torque and ship speed increase. Regarding the impact of head wave disturbance on the system, the time-domain simulation shows that the engine operating cloud becomes less vertical due to more engine speed fluctuation. The frequency-domain analysis can further explain these phenomena.

In addition to time-domain analysis, the frequency-domain analysis was conducted by evaluating the system response spectrum, which can be derived from the Bode magnitude plots as well as the wind and wake spectrum. Thus, how the energy is conveyed from the marine environment to the system can be tracked and the main research question can be addressed better. Consequently, the wind-assisted ship propulsion system will be activated if the frequency region of the wind and wake spectrum overlaps with that of the system transfer function where it is sensitive to. Therefore, the ship speed is not strongly influenced by the irregular wake disturbance because the wake spectrum and the ship speed's transfer function with higher sensitivity to wake do not overlap. Regarding the impact of the true wind disturbance on the system, the engine torque and ship speed are more sensitive to the true wind speed in low-frequency region. Concerning the wake disturbance generated from stern to head waves, frequency-domain analysis shows that the engine speed response spectrum is gradually enlarged. In contrast, the engine torque response spectrum gradually shrinks from stern to head waves. This explains why the engine operating cloud becomes less vertical in irregular head waves. Finally, for the selected case with a specific controller, the sensitivity study shows that the increase of ship mass and the moment of inertia, in general, reduces the response of the propulsion engine as well as the ship speed to the variation of true wind speed and wake. However, within the frequency region where the controller has a relatively poor performance, the system response to the disturbances within this frequency region will be enlarged.

Overall, under the favorable wind angle at Beaufort scale 7, although the given controller, which induces the fluctuation of fuel injection and subsequently the engine load disturbance under dynamic condition, the size of the engine operating cloud for the selected case is not quite big, and the impact of the true wind speed disturbance on the dynamic behavior of the engine is not significant. Therefore, based on the simulation results for the selected case, the potential of the wind-assisted ship propulsion system is still promising sign. For other cases or with more rotors, the approach used in this thesis can be applied to evaluate the dynamic behavior of the wind-assisted ship propulsion system.

6.2. Recommendations for future research

After more understanding of the dynamic behavior of a wind-assisted ship propulsion system for the specific selected case, the research can be further enriched in the following directions.

Extension to 3D

In this thesis, only the longitudinal motion of the ship is mainly considered. However, if the wind comes from the ship's side, it's motion, such as roll, will be influenced. Subsequently, the thrust generated by the Flettner rotor will be influenced. In addition, the yaw's motion, which influences the leeway angle, can also be included so that the apparent wind angle sensed by the rotor can be more accurate.

Therefore, it is recommended to extend the model with a model describing the manoeuvering behavior.

Analysis of other operating conditions
Besides the favor true wind angle, the dynamic behavior of a wind-assisted ship can also be investigated at other true wind angles, such as headwind. The additional drag was induced instead of the thrust and thus the rotor is recommended to be depowered under this condition. On the other hand, in addition to the desired ship speed, the dynamic behavior of the wind-assisted ship at different ship speed can also be evaluated. According to Chapter 4, the energy distribution of wave encounter spectrum is influenced by the ship speed. Considering the impact of the ship speed on the system transfer function and the apparent wind, the system response at different ship speeds would also be worth investigating.

Addition of more components
The electric motor that used to spin the rotor can also be included and linearized in the future. Besides, instead of using only one specific Flettner rotor, different sizes of it and more rotors can also be included to evaluate the dynamic performance of the wind-assisted performance. The impact of a different number of the rotor on the engine performance would be evaluated by adding a different number of the derived Flettner rotor model into the ship speed loop. Under its favorable wind condition, it is expected that the engine loading would be further decreased, which implies that losses from the gearbox might be significant and a more complex gearbox model [Godjevac et al., 2016] might need to be considered. Another extension can be the resistance disturbances, such as added wave resistance, which is also influenced by the wave amplitude and ship heading relative to waves. Especially for head waves, a relatively higher added resistance would be generated. Considering this, it would be worthwhile to include it in the ship speed loop. In addition to the forces produced by the Flettner rotor, the wind resistance might play an important role for ships with a larger surface area. Hence,the resistance can also be considered and it could be estimated for a wind from any direction as shown in the literature [Journee and Pinkster, 1997].

Controller development
With the derived wind-assisted ship propulsion model, especially its linearised model in State-space form, the engine speed governor gain setting used in the given controller can be further refined systematically to evaluate the dynamic behavior of the system. Besides, it might be beneficial for the engine speed governor gain settings to be dependent on the system operating point instead of the maximum operating point.

Other applications
The derived linearised model for obtaining the apparent wind and encounter wake spectrum might also be used in other applications, such as Dynamic Position, which also encounter apparent wind and heading relative to encounter waves during when it moves. Furthermore, the new approach, system response spectrum for the engine, might provide the benefits for the designer to get more insight into how the energy from the marine environment is conveyed to the system.

Bibliography

Odd Jan Andersen and Jørgen Løvseth. Stability modifications of the frøya wind spectrum. *Journal of wind engineering and industrial aerodynamics*, 98(4-5):236–242, 2010.

Nicolas Bialystocki and Dimitris Konovessis. On the estimation of ship's fuel consumption and speed curve: A statistical approach. *Journal of Ocean Engineering and Science*, 1(2):157–166, 2016.

Jan J Blok. The resistance increase of a ship in waves. 1993.

G Bordogna, S Muggiasca, S Giappino, Marco Belloli, JA Keuning, RHM Huijsmans, and AP van't Veer. Experiments on a flettner rotor at critical and supercritical reynolds numbers. *Journal of Wind Engineering and Industrial Aerodynamics*, 188:19–29, 2019.

Giovanni Bordogna, DJ Markey, RHM Huijsmans, JA Keuning, and FV Fossati. Wind-assisted ship propulsion: A review and development of a performance prediction program for commercial ships. In *Proceedings of the 11th International Conference on Hydrodynamics, ICHD 2014, Singapore. P2014-1*, 2014.

Emmanuel Branlard. Generation of time series from a spectrum: generation of wind time series from the kaimal spectrum, generation of wave time series from jonswap spectrum. *Technical University of Denmark*, 2010.

John Carlton. *Marine propellers and propulsion*. Butterworth-Heinemann, 2018.

KMJ Drenthe, GR Dekker, LJ Kemp, and DAM van Velzen. Propellers performance in oblique flow. 2016.

R Eggers and AS Kisjes. Seakeeping and manoeuvring for wind assisted ships. 2019.

Rogier Eggers. Operational performance of wind assisted ships. In *Proc. 10th Symposium on High-Performance Marine Vehicles (HIPER), Cortona, Italy*, 2016.

Fabio Fossati. *Aero-hydrodynamics and the performance of sailing yachts: the science behind sailing yachts and their design*. A&C Black, 2009.

Toshifumi Fujiwara, Grant E Hearn, Fumitoshi Kitamura, Michio Ueno, and Yoshimasa Minami. Steady sailing performance of a hybrid-sail assisted bulk carrier. *Journal of marine science and technology*, 10(3):131–146, 2005.

Catalin Gavriluta, Sergiu Spataru, Ioan Mosincat, Constantino Citro, Ignacio Candela, and Pedro Rodriguez. Complete methodology on generating realistic wind speed profiles based on measurements. In *International conference on renewable energies and power quality*, volume 1, 2012.

RD Geertsma, RR Negenborn, K Visser, and JJ Hopman. Design and control of hybrid power and propulsion systems for smart ships: A review of developments. *Applied Energy*, 194:30–54, 2017a.

RD Geertsma, RR Negenborn, K Visser, MA Loonstijn, and JJ Hopman. Pitch control for ships with diesel mechanical and hybrid propulsion: Modelling, validation and performance quantification. *Applied Energy*, 206:1609–1631, 2017b.

RD Geertsma, K Visser, and RR Negenborn. Adaptive pitch control for ships with diesel mechanical and hybrid propulsion. *Applied Energy*, 228:2490–2509, 2018.

Milinko Godjevac, Joost Drijver, Leo de Vries, and Douwe Stapersma. Evaluation of losses in maritime gearboxes. *Proceedings of the Institution of Mechanical Engineers, part M: Journal of Engineering for the Maritime Environment*, 230(4):623–638, 2016.

Siegfried Heier. *Grid integration of wind energy: onshore and offshore conversion systems*. John Wiley & Sons, 2014.

Johan MJ Journee and JA Pinkster. Offshore hydromechanics. *TUDelft, Faculty of Marine Technology, Ship Hydromechanics Laboratory, Report No. 1112-K, Lecture Notes*, 1997.

Martin Kaltschmitt, Wolfgang Streicher, and Andreas Wiese. *Renewable energy: technology, economics and environment*. Springer Science & Business Media, 2007.

Jukka Kuuskoski. Norsepower rotor sail solution. 2017.

Edward M Lewandowski. *The dynamics of marine craft: maneuvering and seakeeping*, volume 22. World scientific, 2004.

P Naaijen, V Koster, and RP Dallinga. On the power savings by an auxiliary kite propulsion system. *International shipbuilding progress*, 53(4):255–279, 2006.

Ulrik D Nielsen. Transformation of a wave energy spectrum from encounter to absolute domain when observing from an advancing ship. *Applied Ocean Research*, 69:160–172, 2017.

Tristan Pérez and Mogens Blanke. Simulation of ship motion in seaway. *The University of Newcastle, Technical Report, no. EE02037*, 2002.

Xiaobin Qian, Yong Yin, Xiufeng Zhang, Xiaofeng Sun, and Helong Shen. Modelling and application of ocean wind disturbance for ship dynamic positioning simulator. In *2016 35th Chinese Control Conference (CCC)*, pages 2126–2131. IEEE, 2016.

Lloyds Register. Wind-powered shipping: A review of the commercial, regulatory and technical factors affecting uptake of wind-assisted propulsion, 2015.

Stewart Schlesinger. Terminology for model credibility. *Simulation*, 32(3):103–104, 1979.

JJA Schot and R Eggers. The effect of leeway angle on the propeller performance. 2019.

W Shi, HT Grimmelius, and D Stapersma. Analysis of ship propulsion system behaviour and the impact on fuel consumption. *International shipbuilding progress*, 57(1-2):35–64, 2010.

TWP Smith, P Newton, G Winn, and A Grech La Rosa. Analysis techniques for evaluating the fuel savings associated with wind assistance. 2013.

D Stapersma. Interaction between propulsor and engine. *Proceedings of the 34th WEGEMT School" Developments in the Design of Propulsors and Propulsion Systems", AULA, TUDelft, June 2000, Edited by: PW de Heer, Paper: P2000-7 Proceedings.*, 2000.

Douwe Stapersma and Arthur Vrijdag. Linearisation of a ship propulsion system model. *Ocean Engineering*, 142:441–457, 2017.

Fabian Tillig and Jonas W Ringsberg. A 4 dof simulation model developed for fuel consumption prediction of ships at sea. *Ships and Offshore Structures*, 14(sup1):112–120, 2019.

Michael Traut, Paul Gilbert, Conor Walsh, Alice Bows, Antonio Filippone, Peter Stansby, and Ruth Wood. Propulsive power contribution of a kite and a flettner rotor on selected shipping routes. *Applied Energy*, 113:362–372, 2014.

Masaru Tsujimoto and Hideo Orihara. Performance prediction of full-scale ship and analysis by means of on-board monitoring (part 1 ship performance prediction in actual seas). *Journal of Marine Science and Technology*, 24(1):16–33, 2019.

Jarkko Väinämö. Operational experiences and results from the first reference installation from nov-2014, roro-ship estraden (9700 dwt). In *24th International HISWA Symposium on Yacht Design and Yacht Construction. Amsterdam, The Netherlands*, 2016.

NJ van der Kolk, G Bordogna, JC Mason, P Desprairies, and A Vrijdag. Case study: Wind-assisted ship propulsion performance prediction, routing, and economic modelling. In *International Conference Power & Propulsion Alternatives for Ships*. The Royal Institution of Naval Architects-RINA, 2019.

PJ Van Spronsen and RL Tousain. An optimal control approach to preventing marine diesel engine overloading aboard karel doorman class frigates. *IFAC Proceedings Volumes*, 34(7):493–498, 2001.

Det Norske Veritas. Dnv-rp-c205 environmental conditions and environmental loads. *Det Norske Veritas: Oslo, Norway*, 2010.

A Vrijdag and D Schuttevaer. Exploration of a systems and control approach to reduce propeller cavitation in a seaway. *Ocean Engineering*, 182:174–187, 2019.

A Vrijdag and D Stapersma. Extension and application of a linearised ship propulsion system model. *Ocean Engineering*, 143:50–65, 2017.

Arthur Vrijdag, D Stapersma, and T Van Terwisga. Control of propeller cavitation in operational conditions. *Journal of Marine Engineering & Technology*, 9(1):15–26, 2010.

H Klein Woud and D Stapersma. Design of propulsion and electric power generation systems, london: Institute of marine engineering. *Science and Technology*, 2002.

Appendix A

Linearisation of subsystems

A.1. The ship speed loop

The dynamics speed of the ship speed can be described by:

$$m_{ship} \cdot \frac{\mathrm{d}V_s}{\mathrm{d}t} = F_{prop} + F_{rotor,x} - F_{ship} \tag{A.1}$$

In the nominal situation:

$$F_{prop} = F_{prop,0} + \delta F_{prop} \tag{A.2}$$

$$F_{rotor,x} = F_{rotor,x,0} + \delta F_{rotor,x} \tag{A.3}$$

$$F_{ship} = F_{ship,0} + \delta F_{ship} \tag{A.4}$$

assuming equilibrium:

$$F_{prop,0} + F_{rotor,x,0} = F_{ship,0} \tag{A.5}$$

hence:

$$m_{ship} \cdot \frac{\mathrm{d}V_s}{\mathrm{d}t} = \delta F_{prop} + \delta F_{rotor,x} - \delta F_{ship} \tag{A.6}$$

Divided by the nominal forces and introducing the integrator constant of the ship:

$$\begin{aligned} \frac{m_{ship} \cdot V_{s,0}}{F_{ship,0}} \cdot \frac{1}{V_{s,0}} \cdot \frac{\mathrm{d}V_s}{\mathrm{d}t} = \frac{F_{prop,0} + F_{rotor,x,0}}{F_{ship,0}} \cdot \frac{F_{prop,0}}{F_{prop,0} + F_{rotor,x,0}} \cdot \frac{\delta F_{prop}}{F_{prop,0}} \\ + \frac{F_{prop,0} + F_{rotor,x,0}}{F_{ship,0}} \cdot \frac{F_{rotor,0}}{F_{prop,0} + F_{rotor,x,0}} \cdot \frac{\delta F_{rotor}}{F_{rotor,x,0}} \\ + \frac{\delta F_{ship}}{F_{ship,0}} \end{aligned}$$

gives

$$\tau_v \cdot \frac{\mathrm{d}V_{ship}^*}{\mathrm{d}t} = \frac{F_{prop,0}}{F_{ship,0}} \cdot \delta F_{prop}^* + \frac{F_{rotor,x,0}}{F_{ship,0}} \cdot \delta F_{rotor,x}^* - \delta F_{ship}^* \tag{A.7}$$

Define the two constants as:

$$\kappa_{rotor} = \frac{F_{rotor,x,0}}{F_{ship}}, \kappa_{prop} = \frac{F_{prop,0}}{F_{ship}} \tag{A.8}$$

gives

$$\tau_v \cdot \frac{\mathrm{d}V_{ship}^{*}}{\mathrm{d}t} = \kappa_{prop} \cdot \delta F_{prop}^{*} + \kappa_{rotor} \cdot \delta F_{rotor,x}^{*} - \delta F_{ship}^{*} \tag{A.9}$$

A.2. The rotor thrust

In case that the Flettner rotor shaft speed is set as a constant, the expected form of $\delta F_{rotor,x}^{*}$ is expected as:

$$\delta F_{rotor,x}^{*} = \lambda_{TWS} \cdot \delta TWS^{*} + \lambda_{TWA} \cdot \delta TWA^{*} + \lambda_{VS} \cdot \delta V_{S}^{*} \tag{A.10}$$

The thrust generated by the Flettner rotor is described by:

$$F_{rotor,x} = F_L \cdot sin(AWA) - F_D \cdot cos(AWA) \tag{A.11}$$

in which all forces vary around equilibrium:

$$F_{rotor,x} = F_{rotor,x,0} + \delta F_{rotor,x} \tag{A.12}$$

$$F_L = F_{L,0} + \delta F_L \tag{A.13}$$

$$F_D = F_{D,0} + \delta F_D \tag{A.14}$$

In a steady nominal condition, the ship force equals the sum of propeller and the Flettner thrust. In that case:

$$F_{rotor,x,0} = F_{L,0} \cdot sin(AWA_0) - F_{D,0} \cdot cos(AWA_0) \tag{A.15}$$

Note that given a function f(x) defined near a, the linearization of f(x) at is given by

$$L(x) = f(a) + f'(a) \cdot (x - a) \tag{A.16}$$

Hence, Eq. (A.15) can be linearized initially as:

$$\begin{aligned} F_{rotor,x} = F_L \cdot [sin(AWA_0) + (AWA - AWA_0) \cdot cos(AWA_0)] \\ -F_D \cdot [cos(AWA_0) - (AWA - AWA_0) \cdot sin(AWA_0)] \end{aligned} \tag{A.17}$$

normalization and neglecting second and higher order terms leaves:

$$\begin{aligned} \frac{\delta F_{rotor,x,0}}{F_{rotor,x}} = sin(AWA_0) \cdot \frac{F_{L,0}}{F_{rotor,x,0}} \cdot \frac{\delta F_L}{F_{L,0}} \\ -cos(AWA_0) \cdot \frac{F_{D,0}}{F_{rotor,x,0}} \cdot \frac{\delta F_D}{F_{D,0}} \\ + \left[F_{L,0} \cdot cos(AWA_0) + F_{D,0} \cdot sin(AWA_0)\right] \cdot \frac{AWA_0}{F_{rotor,x,0}} \cdot \frac{\delta AWA}{AWA_0} \end{aligned} \tag{A.18}$$

gives

$$\begin{aligned} \delta F_{rotor,x}^{*} = sin(AWA_0) \cdot \frac{F_{L,0}}{F_{rotor,x,0}} \cdot \delta F_L^{*} \\ -cos(AWA_0) \cdot \frac{F_{D,0}}{F_{rotor,x,0}} \cdot \delta F_D^{*} \\ + \left[F_{L,0} \cdot cos(AWA_0) + F_{D,0} \cdot sin(AWA_0)\right] \cdot \frac{AWA_0}{F_{rotor,x,0}} \cdot \delta AWA^{*} \end{aligned} \tag{A.19}$$

A.3. The lift and drag force

The Flettner rotor's thrust is obtained by:

$$F_L = C_l \cdot \frac{1}{2} \cdot \rho \cdot AWS^2 * S_w \tag{A.20}$$

It can be derived as:

$$\delta F_L^* = \delta C_l^* + 2 \cdot \delta AWS^* \tag{A.21}$$

where

$$C_l = C_{l,0} + (k - k_0) \cdot (\frac{\mathrm{d}C_l}{\mathrm{d}k})_{k_0} \tag{A.22}$$

assuming equilibrium:

$$C_l = C_{l,0} + \delta C_l \tag{A.23}$$

$$k = k_0 + \delta k \tag{A.24}$$

$$\frac{\delta C_l}{C_{l,0}} = (\frac{\mathrm{d}C_l}{\mathrm{d}k})_{k_0} \cdot \frac{k_0}{C_{l,0}} \cdot \frac{\delta k}{k_0} \tag{A.25}$$

normalisation:

$$\delta C_l^* = (\frac{\mathrm{d}C_l}{\mathrm{d}k})_{k_0} \cdot \frac{k_0}{C_{l,0}} \cdot \delta k^* \tag{A.26}$$

where

$$k = \frac{U_{tan}}{AWS} = \frac{\pi \cdot D_{rotor} \cdot n_{rotor}}{AWS} \rightarrow k^* = -1 \cdot \delta AWS^* \tag{A.27}$$

so that:

$$\delta F_L^* = (2 - (\frac{\mathrm{d}C_l}{\mathrm{d}k})_{k_0} \cdot \frac{k_0}{C_{l,0}}) \cdot \delta AWS^* \tag{A.28}$$

Similarly,

$$\delta F_D^* = (2 - (\frac{\mathrm{d}C_d}{\mathrm{d}k})_{k_0} \cdot \frac{k_0}{C_{d,0}}) \cdot \delta AWS^* \tag{A.29}$$

A.4. The true wind speed and apparent wind speed

Apparent wind speed can be described as:

$$AWS = \sqrt{u^2 + v^2} \tag{A.30}$$

which can be written as:

$$AWS^2 = u^2 + v^2 \tag{A.31}$$

assuming equilibrium:

$$AWS^2 = (AWS_0 + \delta AWS)^2 = AWS_0^2 + 2 \cdot AWS_0 \cdot \delta AWS + \delta AWS^2 \tag{A.32}$$

$$u^2 = (u_0 + \delta u)^2 = u_0^2 + 2 \cdot u_0 \cdot \delta u + \delta u^2 \tag{A.33}$$

$$v^2 = (v_0 + \delta v)^2 = v_0^2 + 2 \cdot v_0 \cdot \delta v + \delta v^2 \tag{A.34}$$

$$AWS_0 \cdot \delta AWS = u_0 \cdot \delta u + v_0 \cdot \delta v \quad \text{(A.35)}$$

Neglecting second terms gives:

$$\delta AWS = \frac{u_0}{AWS_0} \cdot \delta u + \frac{v_0}{AWS_0} \cdot \delta v \quad \text{(A.36)}$$

Normalisation results in:

$$\frac{\delta AWS}{AWS_0} = \frac{u_0}{AWS_0} \cdot \frac{u_0}{AWS_0} \cdot \frac{\delta u}{u_0} + \frac{v_0}{AWS_0} \cdot \frac{v_0}{AWS_0} \cdot \frac{\delta v}{v_0} \quad \text{(A.37)}$$

Therefore

$$\delta AWS^* = (\frac{u_0^2}{AWS_0^2}) \cdot \delta u^* + (\frac{v_0^2}{AWS_0^2}) \cdot \delta v^* \quad \text{(A.38)}$$

where u is:

$$u = TWS \cdot cos(TWA) + V_s \quad \text{(A.39)}$$

near equilibrium and linearization:

$$TWS = TWS_0 + \delta TWS \quad \text{(A.40)}$$

$$TWA = TWA_0 + \delta TWA \quad \text{(A.41)}$$

$$V_s = V_{s,0} + \delta V_s \quad \text{(A.42)}$$

$$u_0 = TWS \cdot [cos(TWA_0) - (TWA - TWA_0) \cdot sin(TWA_0)] + V_s \quad \text{(A.43)}$$

assuming equilibrium:

$$u_0 = TWS_0 \cdot cos(TWA_0) + V_{S,0} \quad \text{(A.44)}$$

$$\frac{\delta u}{u_0} = cos(TWA_0) \cdot \frac{TWS_0}{u_0} \cdot \frac{\delta TWS}{TWS_0} + \frac{v_0}{u_0} \cdot \frac{\delta V_s}{v_0} - sin(TWA_0) \cdot TWS_0 \cdot \frac{TWA_0}{u_0} \cdot \frac{\delta TWA}{TWA_0} \quad \text{(A.45)}$$

normalisation gives:

$$\delta u^* = cos(TWA_0) \cdot \frac{TWS_0}{u_0} \cdot \delta TWS^* + \frac{v_0}{u_0} \cdot \delta V_s^* - sin(TWA_0) \cdot TWS_0 \cdot \frac{TWA_0}{u_0} \cdot \delta TWA^* \quad \text{(A.46)}$$

On the other hand, v is:

$$v = TWS \cdot sin(TWA) \quad \text{(A.47)}$$

near equilibrium and linearization:

$$v = v_0 + \delta v \quad \text{(A.48)}$$

$$TWS = TWS_0 + \delta TWS \quad \text{(A.49)}$$

$$TWA = TWA_0 + \delta TWA \quad \text{(A.50)}$$

assuming equilibrium and linearization:

$$v_0 = TWS_0 \cdot sin(TWA_0) \tag{A.51}$$

$$v = TWS \cdot [sin(TWA_0) + (TWA - TWA_0) \cdot cos(TWA_0)] \tag{A.52}$$

normalisation and neglecting second and higher order terms leaves:

$$\frac{\delta v}{v_0} = sin(TWA_0) \cdot \frac{TWS_0}{v_0} \cdot \frac{\delta TWS}{TWS_0} + cos(TWA_0) \cdot TWS_0 \cdot \frac{TWA_0}{v_0} \cdot \frac{\delta TWA}{TWA_0} \tag{A.53}$$

this can be written as:

$$\delta v^* = sin(TWA_0) \cdot \frac{TWS_0}{v_0} \cdot \delta TWS^* + cos(TWA_0) \cdot TWS_0 \cdot \frac{TWA_0}{v_0} \cdot \delta TWA^* \tag{A.54}$$

A.5. The true wind angle and apparent wind angle

The apparent wind angle is:

$$AWA = \begin{cases} \tan^{-1}(\frac{v}{u}) & [rad], \quad (u \geq 0, v \geq 0) \\ \frac{\pi}{2} & [rad], \quad (u = 0, v > 0) \\ \pi + tan^{-1}(\frac{v}{u}) & [rad], \quad (u < 0, v > 0) \end{cases} \tag{A.55}$$

The arc tangent can be described by Taylor series expansion as:

$$\tan^{-1}(x) = \begin{cases} x - \frac{x^3}{3} + \frac{x^5}{5} - ...(-1 < x < 1) \\ \frac{\pi}{2} - \frac{1}{x} + \frac{1}{3 \cdot x^3} - ...(x \geq 1) \\ \frac{-\pi}{2} - \frac{1}{x} + \frac{1}{3 \cdot x^3} - ...(x \leq -1) \end{cases} \tag{A.56}$$

When $|\frac{v}{u}| < 1$, it can be linearized as:

$$AWA \approx \begin{cases} \frac{v}{u}, & u > 0, v > 0 \\ \pi + \frac{v}{u}, & u < 0, v > 0 \end{cases} \tag{A.57}$$

Normalisation results in:

$$\delta AWA^* = \begin{cases} \delta v^* - \delta u^*, & u > 0, v > 0 \\ \frac{1}{AWA_0} \cdot \frac{v_0}{u_0} \cdot (\delta v^* - \delta u^*), & u < 0, v > 0 \end{cases} \tag{A.58}$$

When $|\frac{v}{u}| > 1$, it can be linearized as:

$$\delta AWA^* = \frac{1}{AWA_0} \cdot \frac{u_0}{v_0} \cdot (\delta v^* - \delta u^*) \tag{A.59}$$

The following procedure is used for obtain Eq. (A.59):

$$AWA = \pi + \tan^{-1}(\frac{v}{u}) \approx \pi + (\frac{-\pi}{2} - \frac{1}{\frac{v}{u}}) = \frac{\pi}{2} - \frac{u}{v} \tag{A.60}$$

Normalisation gives:

$$\frac{AWA}{AWA_0} = \frac{\pi}{2 \cdot AWA_0} - \frac{1}{AWA_0} \cdot \frac{u_0}{v_0} \cdot \frac{\frac{u}{u_0}}{\frac{v}{v_0}} \tag{A.61}$$

Differentiation of Eq. (A.61) by using chain rules gives:

$$\frac{dAWA}{AWA_0} = \frac{-1}{AWA_0} \cdot \frac{u_0}{v_0} \cdot \left(\frac{v}{v_0} \cdot \frac{du}{u_0} - 1 \cdot \frac{u}{u_0} \cdot (\frac{v}{v_0})^{-2} \cdot \frac{dv}{v_0} \right) \tag{A.62}$$

Near equilibrium $\mathrm{d}AWA$, $\mathrm{d}u$ and $\mathrm{d}v$ become small increments δ AWA, δu and δ v. Division of $AWA = AWA_0 + \delta AWA$ by AWA_0 gives $\frac{AWA}{AWA_0} = 1 + \frac{\delta AWA}{AWA_0}$ and likewise $\frac{u}{u_0} = 1 + \frac{\delta u}{u_0}$ and $\frac{v}{v_0} = 1 + \frac{\delta v}{v_0}$. Substitution those in Eq. (A.62) delivers and neglecting second and higher order terms leaves:

$$\delta AWA^* = \frac{1}{AWA_0} \cdot \frac{u_0}{v_0} \cdot (\delta v^* - \delta u^*) \tag{A.63}$$

Appendix B

Linearisation of a actuator

According to the study [Shi et al., 2010], the engine torque can be described as:

$$M_B^+ = 1 - C_0 \cdot (1 - n_e^+) + C_1 \cdot (1 - n_e^+)^2 - C_2 \cdot (1 - m_f^+) + C_3 \cdot (1 - m_f^+)^2 + C_4 \cdot (1 - n_e^+) \cdot (1 - m_f^+) \quad \text{(B.1)}$$

where

$$M_B^+ = \frac{M_B}{M_{B,nomi}} \quad \text{(B.2)}$$

$$n_e^+ = \frac{n_e}{n_{e,nomi}} \quad \text{(B.3)}$$

$$m_f^+ = \frac{m_f}{m_{f,nomi}} \quad \text{(B.4)}$$

Near equilibrium, the engine torque, speed and fuel per cycle can be given as:

$$M_B = M_{B,nomi} + \delta M_B \rightarrow M_B^+ = 1 + \frac{\delta M_B}{M_{B,nomi}} \quad \text{(B.5)}$$

$$n_e = n_{e,nomi} + \delta n_e \rightarrow n_e^+ = 1 + \frac{\delta n_e}{n_{e,nomi}} \quad \text{(B.6)}$$

$$m_f = m_{f,nomi} + \delta m_f \rightarrow m_f^+ = 1 + \frac{\delta m_f}{m_{f,nomi}} \quad \text{(B.7)}$$

Substitution those in Eq. (B.1) delivers:

$$\frac{\delta M_B}{M_{B,nomi}} = C_0 \cdot \frac{\delta n_e}{n_{e,nomi}} - C_1 \cdot (\frac{\delta n_e}{n_{e,nomi}})^2 + C_2 \cdot \frac{\delta m_f}{m_{f,nomi}} - C_3 \cdot (\frac{\delta m_f}{m_{f,nomi}})^2 + 2 \cdot C_4 \cdot (\frac{\delta n_e}{n_{e,nomi}}) \cdot (\frac{\delta m_f}{m_{f,nomi}}) \quad \text{(B.8)}$$

Neglecting second order leaves:

$$\frac{\delta M_B}{M_{B,nomi}} = C_0 \cdot \frac{\delta n_e}{n_{e,nomi}} + C_2 \cdot \frac{\delta m_f}{m_{f,nomi}} \quad \text{(B.9)}$$

Normalisation of Eq. (B.9) results in:

$$\frac{M_{B,nomi}}{M_{B,0}} \cdot \frac{\delta M_B}{M_{B,nomi}} = C_0 \cdot \frac{M_{B,nomi}}{M_{B,0}} \cdot \frac{n_{e,0}}{n_{e,nomi}} \cdot \frac{\delta n_e}{n_{e,0}} + C_2 \cdot \frac{M_{B,nomi}}{M_{B,0}} \cdot \frac{m_{f,0}}{m_{f,nomi}} \cdot \frac{\delta m_f}{m_{f,0}} \quad \text{(B.10)}$$

this can be written as:

$$\delta M_B^* = C_0 \cdot \frac{M_{B,nomi}}{M_{B,0}} \cdot \frac{n_{e,0}}{n_{e,nomi}} \cdot \delta n_e^* + C_2 \cdot \frac{M_{B,nomi}}{M_{B,0}} \cdot \frac{m_{f,0}}{m_{f,nomi}} \cdot \delta m_f^* = g' \cdot \delta n_e^* + v' \cdot \delta m_f^* \quad \text{(B.11)}$$

where

$$g = \frac{M_{B,nomi}}{M_{B,0}} \cdot \frac{n_{e,0}}{n_{e,nomi}} \tag{B.12}$$

$$v = \frac{M_{B,nomi}}{M_{B,0}} \cdot \frac{m_{f,0}}{m_{f,nomi}} \tag{B.13}$$

Because the relationship: $m_{f,set} = X_{set} \cdot m_{f,nomi}$, the variation of the fuel injected per cycle equals to the variation of the fuel rack position. Hence, it can be rewritten as:

$$\delta M_B^* = g \cdot \delta n_e^* + v \cdot \delta X_{set}^* \tag{B.14}$$

where

$$\delta m_f^* = \delta X^* = \delta X_{set}^* \tag{B.15}$$

Appendix C

Linearisation of a controller

According to non-normalised control law, the conventional engine speed controller is given by:

$$X_{set} = \left(K_i \cdot \int_0^t \frac{n_{set} - n}{n_{max}} dt + K_p \cdot \frac{n_{set} - n}{n_{max}}\right) \cdot X_{max} \tag{C.1}$$

Normalisation the engine speed with it's maximum engine speed and assuming $n_0 = n_{set,0}$ yields:

$$\frac{X_{set}}{X_{set,0}} = \left(K_i \cdot \int_0^t \frac{n_{set} - n}{n_0} dt + K_p \cdot \frac{n_{set} - n}{n_0}\right) \cdot \frac{X_{max}}{X_{set,0}} \cdot \frac{n_0}{n_{max}} \tag{C.2}$$

Near equilibrium, dX_{set}, dn_{set} and dn become small increments δX_{set},δn_{set} and δn. By applying chain rule results in:

$$\frac{\delta X_{set}}{X_{set,0}} = \left(K_i \cdot \int_0^t \frac{\delta n_{set} - \delta n}{n_0} dt + K_p \cdot \frac{\delta n_{set} - \delta n}{n_0}\right) \cdot \frac{X_{max}}{X_{set,0}} \cdot \frac{n_0}{n_{max}} \tag{C.3}$$

If, by definition

$$\delta E_n^* \equiv \int_0^t \frac{n_{set} - n}{n_0} dt \tag{C.4}$$

Eq. (C.3) can be rewritten as:

$$\delta X_{set}^* = \frac{X_{max}}{X_{set,0}} \cdot \frac{n_0}{n_{max}} \cdot \left(K_i \cdot \delta E_n^* + K_p \cdot (\delta n_{set}^* - \delta n^*)\right) \tag{C.5}$$